Development of a fluorine-free chemical solution deposition route for rare-earth cuprate superconducting tapes and its application to reel-to-reel processing

Tang, Xiao; Grivel, Jean-Claude

Publication date:
2013

Document Version
Publisher's PDF, also known as Version of record

Citation (APA):
Tang, X., & Grivel, J-C. (2013). Development of a fluorine-free chemical solution deposition route for rare-earth cuprate superconducting tapes and its application to reel-to-reel processing. Kgs. Lyngby: Department of Energy Conversion and Storage, Technical University of Denmark.

Development of a fluorine-free chemical solution deposition route for rare-earth cuprate superconducting tapes and its application to reel-to-reel processing

Xiao Tang
Technical University of Denmark

(Confidential until Public Defence)

Abstrakt

Grundet nul modstand og ingen elektrisk energitab under el transmission, vil applikationen af superledere kunne levere en betydelig fordel, særligt taget den hurtige udvikling i betragtning på bekostning af høje energipriser. For operation ved flydende kvælstof temperatur, har REBCO visse fordele i at kunne bibeholde en høj strømningsdensitet under et stærkt magnetisk felt, således har REBCO højtemperatur superledere højt potentiale inden for højfelts tekniske applikationer.

Sammenlignet med Pulsed Laser Deposition (PLD) og kemisk gas deposition (CVD), er trifluoroacetat metal-organisk deposition (TFA-MOD) mere tilnærmelig i produktionen af REBCO tyndfilm, grundet høj J_c, høj reproduktivitet og lave omkostninger, hvilket ikke involverer nogen form for udstyr til kraftig vakuum. TFA-MOD medfølger derimod to ulemper, den ene er frigivelsen af den giftige HF gas som sideprodukt og det andet er den resulterende tidskrævende dekompositionsproces, som normalt koster over 10 timer. Med hensyn til forbedring af den miljømæssige sikkerhed, ydeevne og produktivitet af metoden, er fokus ved dette studie på produktionen af REBCO tyndfilm ud fra fluor-fri MOD (FF-MOD).

I kapitel 3 er der lavet en gennemgang af eksisterende CSD metoder. Ifølge de forskellige Barium intermediet faser efter dekomponering af organisk precursor, er hoved CSD processerne klassificeret i fire kategorier, for hvilke er barium-fluor processer, bariumhydroxid processer, bariumnitrat processer og bariumcarbonat processer. Med formål at udpege den mest egnede proces for produktion af REBCO tyndfilm i vores forskning, var der også udført forsøg til sammenligning af kvaliteten for micro-struktur for tyndfilm og reaktionsmekanismerne for disse processer.

I kapitel 4 og 5 bruges en fluor-fri vandbaseret sol-gel proces til fremstilling af YBCO tyndfilm. Fokus i kapitel 4 var på optimering af pH værdi med formål at forbedre micro-strukturen og den superledende ydeevne for YBCO tyndfilm. Fokus i kapitel 5 var på udvælgelsen af chelaterende midler på basis af precursor opløsningens stabilitet.

I kapitel 6 var højtermisk-stabilitet polymeriseret akrylsyre brugt til at undertrykke kornvækst i de intermediære faser, dannet under og efter pyrolysen, formålet med det var at fremstille GdBCO tyndfilm af høj kvalitet.

I kapitel 7 var en metanol-baseret fluor-fri MOD metode brugt til deponering af YBCO-Ag superledende tyndfilm. De sporbare mængder af sølv blev brugt til at sænke smeltepunktet for YBCO, hvilket kunne forstærke sammenkoblingen mellem YBCO korn og som konsekvens forøge J_c for tyndfilmen.

I kapitel 8, baseret på effekten af $BaZrO_3$-doping i forbedring af in-field ydeevne af YBCO tyndfilm og den positive indflydelse af Ag-doping til accelerationen af YBCO kornvækst, hvilket var blevet gjort i kapitel 7, er effekten af $BaZrO_3$/Ag hybrid doping på micro-strukturen og ydeevnen af FF-MOD udviklet YBCO tyndfilm undersøgt.

ACKNOWLEDGEMENTS

This dissertation would not have been possible without the guidance and the help of several individuals who in one way or another contributed and extended their valuable assistance in the preparation and completion of this study in the last three years.

Foremost, I am thankful to my PhD thesis supervisor, Dr. Jean-Claude. Grivel, not only for the opportunities he gave me to conduct my academic research in RISØ, DTU, but also for his insight, thought provoking questions and guidance for my thesis.

In addition, I would like to acknowledge my PhD thesis co-supervisor Professor Niels Hessel Andersen for abundant guidance during the completion of this thesis and the invaluable support the most of the magnetic measurements.

Also a special acknowledgement should be shown to Dr. Yue Zhao, during the past three years who helped me a lot both in scientific research and in life.

I would also like to thank Dr. Dong He, Dr. Xiaofen Li, Dr. Anders Christian Wulff, Mr. Asanka Pramod Pallewatta, Dr. Dimitris Pavlopoulos, Dr. Wei Wu and Dr. Tim Holgate. During the time I benefited both in my experiment and discussions with them.

I also extend my thanks to Miss. Yan Xu and Miss. Yunran Xue, for their assistance in my experiments. I wish these two fresh PhD students who are studying in China that everything goes well in the coming several years.

I would like to acknowledge my parents and family members for the personal sacrifices they made to push me forward to allow me to reach new levels of excellence.

Finally, I am indebted to my beloved wife Yan Yang, for her silent but irreplaceable support.

As an old Chinese poem says, even a blade of grass wants to repay the spring warmth and brightness. I dedicate this thesis to every individual that cared about me. Imperfect as it is, it is my sincerest present.

Abstract

Due to the zero resistance and no electric energy loss during electricity transmission, the application of superconductivity would provide a considerable benefit, especially when considering the fast development at the expense of high energy cost nowadays. For operation at liquid nitrogen temperature, REBCO (RE= rare earth) has some evident advantages compared to other high-temperature superconductors in retaining high current densities under strong magnetic fields, thus REBCO high temperature superconductors have significant potential for high field engineering applications.

Compared to Pulsed Laser Deposition (PLD) and Chemical Vapor Deposition (CVD), the trifluoroacetate metal-organic deposition (TFA-MOD) route is more promising for producing REBCO superconducting films, owing to the high-J_c, high reproducibility, and low cost of this technique, which doesn't require any high vacuum equipment. The TFA-MOD has however two intrinsic disadvantages, one being the released hazardous HF gas as a byproduct, while the other is the resulting time-consuming decomposition process, which normally costs more than 10h. In the aim of improving environmental safety, performance and the productivity of the method, the focus of this study is on the production of REBCO films by using fluorine-free MOD (FF-MOD) routes.

In Chapter 3, a review was made on the existing CSD methods. According to the different barium intermediate phases after the decomposition of the organic precursors, the main CSD processes are classified into four categories, which are the barium fluoride process, barium hydroxide process, barium nitrate process, and barium carbonate process. In the aim of selecting the most suitable process for producing REBCO films in our research, trial experiments were also done to compare microstructure quality of the film products and the reaction mechanisms of these processes.

In Chapter 4 and Chapter 5, a fluorine-free water-based sol-gel process was used to produce YBCO films. The focus of chapter 5 was on the optimization of the pH value in the aim of improving the microstructure and superconducting performance of the YBCO films, and the focus of chapter 4 was on the selection of chelating agents on the basis of the precursor solution stability.

In Chapter 6, high-thermal-stability polymerized acrylic acid was used to suppress the grain growth of intermediate phases forming during and after pyrolysis in the aim of producing high quality GdBCO thin films.

In Chapter 7, a methanol-based non-fluorine MOD method was used to deposit YBCO-Ag superconducting thin films. A trace amount of silver addition was used to decrease the melting point of YBCO, which could enhance the interconnection between YBCO grains and in consequence increase the J_c of the films.

In Chapter 8, based on the effect of $BaZrO_3$-doping in improving the in-field performance of YBCO films, and on the positive influence of Ag-doping in accelerating YBCO grain growth, which has been confirmed in Chapter 6, the effect of $BaZrO_3$/Ag hybrid doping on the microstructure and performance of FF-MOD derived YBCO films was investigated.

Chapter 9 is the summary of the thesis.

Table of Contents

Chapter 1

Introduction to the development of superconductors

1.1 Introduction to superconductors

1.1.1 Discovery of superconductors

Research on the fundamental properties that are displayed by materials at extremely low temperatures have always been one of the most appealing topics attracting the interest of scientists. At end of the 18th century, the development of the technologies used for gas liquefaction allowed to achieve ever lower temperature conditions. In 1908, by condensing Helium, H. Kammerlingh. Onnes successfully obtained the temperature of 4.25K, which is quite close to the absolute zero [1]. Three years later, Onnes accidentally observed the disappearance of resistance in mercury when its temperature decreased to 4K [2]. This unprecedented electrical performance was then formally named as “Superconductivity”, which won Onnes the Nobel Prize in 1913 for this great discovery. However, that was not the end of the story, but the unsealing of a new research field.

In the following decades, many other superconductors, such as lead with a transition to the superconducting state at 7.2K, niobium at 8K, niobium nitrides at 15K and niobium germanium at 23K were discovered [3]. As time passed, increasingly higher critical temperatures (T_c) were gradually found in more than 2000 kinds of materials, which include metals, alloys, inorganic compounds and even organic compounds [4]. Especially in 1987, Maokun Wu and Jingwu Zhu successfully synthesized the yttrium barium copper oxide $YBa_2Cu_3O_{7-\delta}$ (YBCO), which displays a high T_c of 92K, above the boiling point of nitrogen (77K), making one more marked step towards the commercialization of superconductors [5].

1.1.2 Characteristics of superconductors

When a superconductor is subjected to conditions where the temperature is lower than T_c, and the magnetic field is lower than the critical magnetic field (H_c), two phenomenons appear in the superconductor:

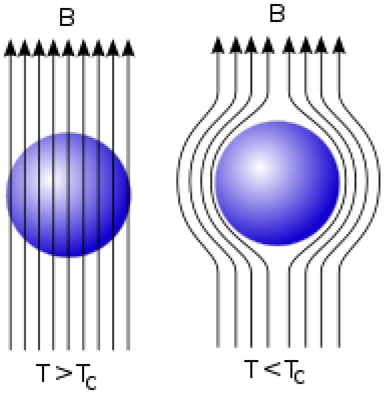

Fig 1.1 The Meissner effect in a superconductor [6].

1. Zero resistance: The electrical resistance of the superconductor is zero.

2. Superdiamagnetism (Meissner Effect): inside the superconductor the magnetic flux is zero, i.e. the lines of magnetic force can't enter the material, as shown in **Fig 1.1** [6]. This on the other hand, means that a superconductor is not a perfect conductor.

In 1935, two years after the discovery of the Meissner effect (1933), the brothers Fritz and Heinz London proposed that the magnetic field is actually not completely expelled by the conductor, but penetrates the superconductor surface to some extent [7]. However, the magnetic field strength declines exponentially within the penetration depth. In superconductors, the London penetration depth (usually denoted as λ or λL) characterizes the distance to which a magnetic field penetrates into a superconductor and becomes equal to 1/e times that of the magnetic field at the surface of the superconductor [7].

On the other hand, the critical magnetic field (H_c) mentioned above is closely related to the temperature [8], as shown in equation (1-1):

$$H_c(T) \sim H_c(0)[1-(T-T_c)^2] \quad (1\text{-}1)$$

where $H_c(0)$ is the critical magnetic field of the superconductor when the temperature is at 0K. As expressed in equation (1-1), the critical magnetic field H_c (T) is propotional to the difference between the applied field and the applied field multiplied by the square of ($T-T_c$). When a current "I" is passing through a superconductor of a radius "R", the strength of the induced magnetic field at the surface of the superconductor is:

$$Hs=\frac{I}{2\pi R} \quad (1\text{-}2)$$

According to the Silsbee theory, when the strength of the induced surface magnetic field (H_s) equals that of the critical magnetic field (H_c), the superconductivity is destroyed.

By substituting $H_s=H_c(T)$ into the equation, the critical current I_c (T) is obtained:

$$I_c(T)=2\pi RH_c(T) \quad (1\text{-}3)$$

Hereby, it can be seen that the critical quantities temperature (T_c), magnetic field (H_c) and current density (J_c) are closely coupled in determining the state of the superconductor. This is shown in **Fig 1.2**, where beneath the curved surface the material is superconducting while everywhere above the curved surface it is in the normal state.

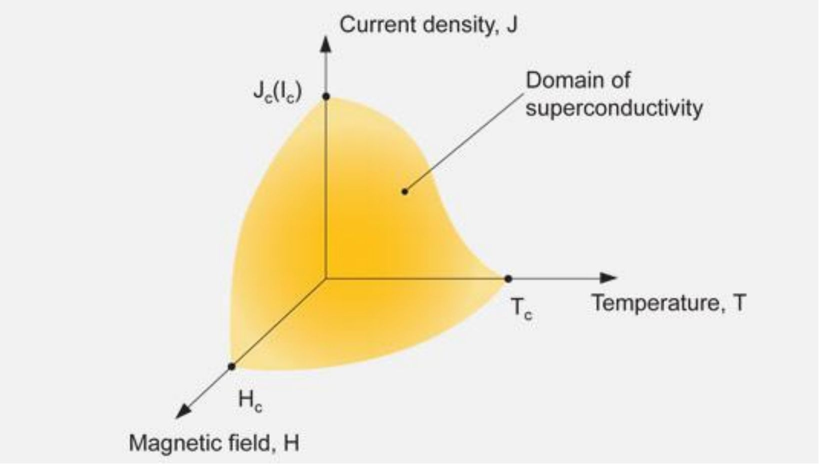

Fig 1.2 *Superconducting state diagram [9].*

1.1.3 Classification of superconductors

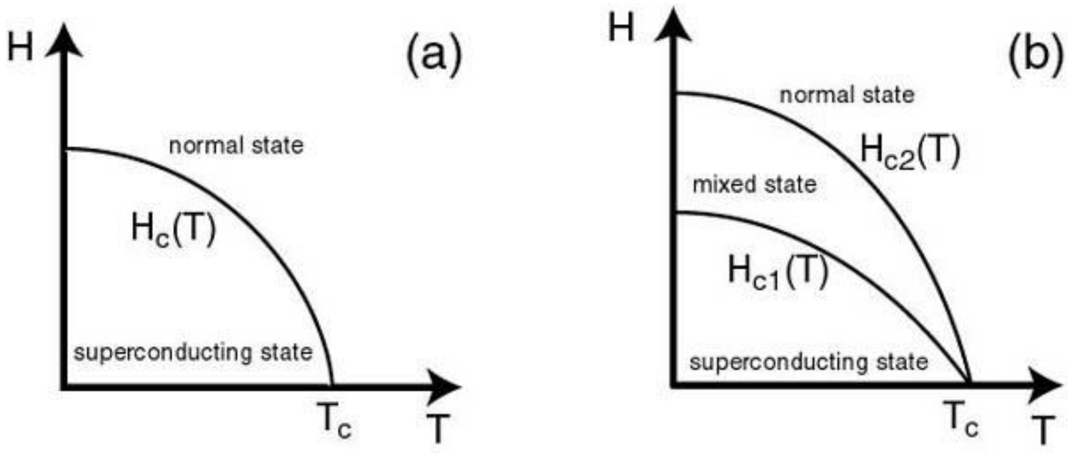

Fig 1.3 *Externally applied magnetic field strength versus temperature for (a) Type I superconductors (b) Type II superconductors [10].*

Type I superconductors

Type I superconductors exhibit two characteristic states, as shown in **Fig.1.3 (a)**. There is only one critical field (H_c), above which the Meissner effect disappears and the magnetic flux can't be expelled from the specimen. This type of superconductivity is normally exhibited by pure metals, e.g. aluminium, lead, and mercury.

Type II superconductors

For type II superconductors, there are two distinct critical fields, Hc_1 and Hc_2. Magnetic vortices form when there is an applied magnetic field. This occurs above a certain critical field strength Hc_1. The vortex density increases with increasing field strength. At a higher critical field Hc_2, superconductivity is completely destroyed. Superconductors such as metal alloy superconductors and cuprate-perovskite ceramic materials, for example YBCO, the one that is being investigated in this thesis, exhibit the type-II behavior, as can be seen from the **Fig 1.3 (b)**.

As shown in **Fig 1.4 (a)**, the type II superconductors that exhibit reversible hysteresis loops are considered as ideal type II superconductors. However, in general, they do not obey this behavior and are called "real type II superconductors", (**Fig 1.4 (b)**).

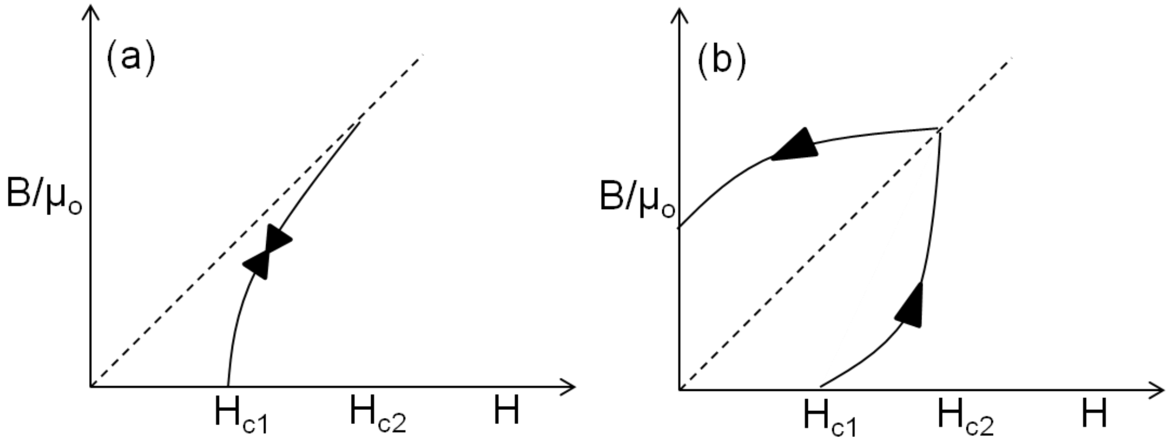

Fig 1.4 *Typical magnetization curve of ideal (a) and real (b) type II superconductors in magnetic measurements.*

As can be seen from the magnetization curve of a real type II superconductor, during the increase of H, the magnetization is slower than that of the ideal one. Similarly, during the decrease of H, the expelling of the internal magnetic fluxes is also relatively sluggish compared to ideal type II superconductors. Even when the applied field declines to zero, residual flux still exists, meaning that some of the flux lines are trapped inside the superconductor. It has been confirmed that the hysteresis as seen in the real type II superconductor resulted from defects such as dislocations, twin planes, stacking faults or small precipitation phases of a size similar to the coherence length (ξ). Because the energy difference for the transformation from superconducting state to normal state is lower in a defect phase compared to that in a non-defect phase, the magnetic flux is pinned from further creeping when it meets a defect during motion inside the superconductor. The defects described here are the so-called flux pining centers, which are quite crucial to the application of type II superconductors. A Lorentz force is generated when a current is applied to a type II superconductor and results in flux motion if there is no barrier for that. The flux motion at a velocity ν and in an electric field E, in consequence induces a voltage, which causes energy dissipation and therefore the zero-resistance no longer exists. It is the pinning force provided by the flux pinning centers that balances the flux motion induced by the Lorenz force and allows supercurrents to persist in the specimen.

1.1.4 Bean Model

To establish a theory of the mixed state of the type II superconductors, many scientists have done a lot of detailed investigations and theoretical calculations. In 1964, Bean proposed a theory to describe the penetration of the magnetic field into a superconductor [11]. With the applied magnetic field gradually increasing from zero to H_{c1}, the magnetic flux is completely expelled from the superconductor due to the Meissner effect which has been described in § 1.1.3. When the applied field is higher than Hc1, the magnetic field enters the superconductor in the form of magnetic flux quanta. As mentioned above, the motion is stopped when a flux quantum meets a flux pinning center. As the applied field continues increasing and eventually the induced Lorentz force exceeds the pinning force, the pinned flux will leave the pinning center and further move inside the material, until it encounters the next pinning center.

In the Bean model, it is assumed that in a state of equilibrium distribution of magnetic fluxes, the flux pinning force is equal to that of the induced Lorenz force, while the magnetic flux density in the neighboring penetrated layer is equal to that of an ideal type II superconductor. Another assumption is that the induced supercurrent density is equal to the critical current density (J_c), as shown in the Maxwell formula:

$$\bigtriangledown \times H = J_{ext} = J_c$$

Where J_{ext} is the magnetic field induced current density. Considering a one-dimensional space and infinite length of a superconductor, the formula is simplified as:

$$dH/dx=J_c$$

By using this formula, the critical current density can be calculated from the variation of the remaining magnetic field in a superconductor. For a cylindrical shaped specimen, by accounting the moment difference between magnetization and demagnetization, J_c(H) can be calculated by using the formula:

$$J_c(H)=30\Delta M/d$$

where ΔM is the width of the hysteresis loop (in A cm^{-2}), d is the radius of the sample volume (in cm).

Based on the Bean Model, E. M. Gyrogy deduced a formula which is applied on rectangle specimens [12]:

$$Jc = \frac{20\Delta M}{V\mathrm{a}(1 - a/3b)}$$

where ΔM is the width of the hysteresis loop (in A cm^{-2}), V is the sample volume (in cm^3), a and b are the cross-sectional dimensions of the sample perpendicular to the applied field with a≥b (in cm). This formula is also used in our experiments.

1.2 Critical temperature

The evolution of the superconducting transition temperature in various material classes is depicted in **Fig 1.5**. Nowadays, 30K is regarded as the border temperature to classify low-temperature (LTS) and high-temperature superconductors (HTS). This is basically related to the T_c of Nb_3Ge, which is 23.2K and remained the highest T_c superconductor for more than one decade since 1973 until 1986, when $La_{2-x}Ba_xCuO_{4-\delta}$ was found to be superconductive at 35K [13].

Many other cuprate HTSs gradually appeared in the years following the discovery of LaBCO and YBCO. In 1988, Bi-Sr-Ca-Cu-O (BSCCO) and Tl-Ca/Ba-Cu-O compounds were subsequently found to be superconductive at up to 105K and 120K, respectively [15, 16]. In 1993, the first Hg-based cuprate superconductor, $HgBa_2CuO_{4+x}$ was found to have a T_c of 94K [17]. One year later, $HgBa_2Ca_2Cu_3O_{8-x}$ (Hg-1223) was found to have a T_c up to 134K [18], interestingly, when applying a high pressure of 31GPa on the material, the T_c of Hg-1223 can shift upward to as high as 164K, which still remains the world record till now [19].

Another interesting HTS material is MgB_2, which in 2001 was found to have a T_c of 39K [20]. Though not of a high T_c among the HTS materials, MgB_2 caused a remarkable interest in the industrialization of superconductors due to the low cost of magnesium and boron reactants and its simple structure, which makes that MgB_2 wires can be produced easily by using the already-commercialized powder-in tube (PIT) process.

The latest discovered HTS materials were iron-based $LaFeAsO_{1-x}Fx$ and $SmFeAsO_{1-x}F_x$, which were found to be superconductive at the temperatures of 26K and 55K, respectively [21, 22]. Nowadays, the research interest in the iron-based HTS materials is still going on [23].

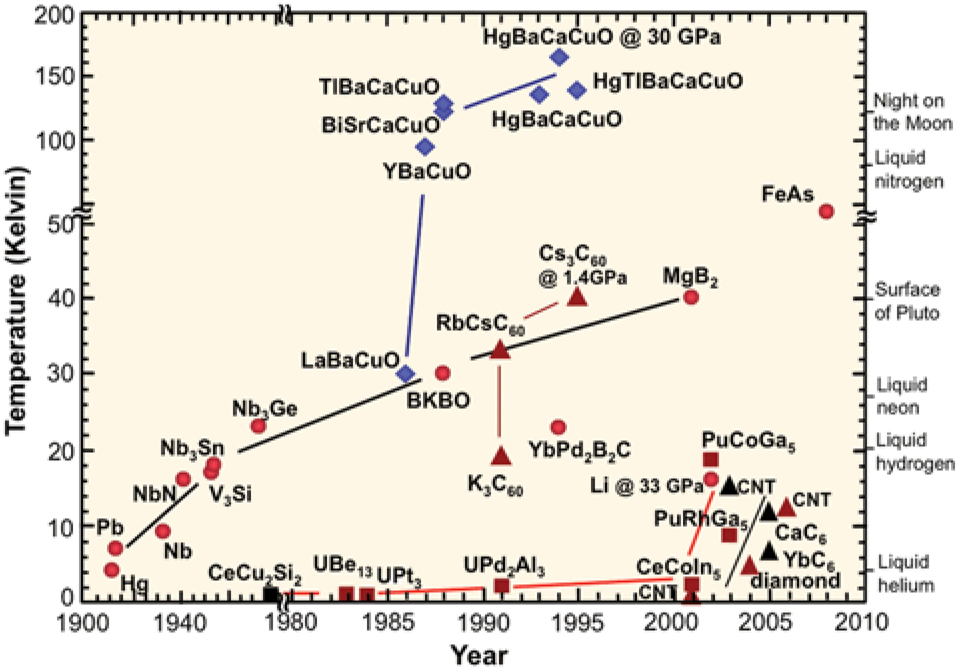

Fig 1.5 *Evolution of the superconducting transition temperature [14].*

Among all the HTS materials, especially the materials with T_c higher than the boiling point of nitrogen, Tl-based and Hg-based cuprates undoubtedly have a dramatic advantage when considering their high T_c. However, the high toxicity of Hg and Tl makes them not quite suitable for large scale production and application. For this reason, YBCO and BSCCO are still the most promising HTS materials for large scale commercialization.

1.3 Application of high temperature superconductors

1.3.1 Magnet technology

One of the most important advantages of superconducting magnets is that no heating takes place when the magnet transports high current densities. Compared to traditionally used copper or aluminum windings, the design of a superconducting magnet can be more compact and yields much more efficient performance. Nowadays, the commonly used superconductors in this field are Nb3Sn and NbTi, which are not considered as HTS, however, it is conceivable that some HTS materials are going to be applied in this field in the very near future.

Some other applications of HTS in magnet technology are the Nuclear Magnetic Resonance (NMR) and Medical Resonance Imaging (MRI) used in medical industry [24]. Also, for applications in the energy storage field, Superconducting Magnetic Energy Storage (SMES) technology is also being developed [25]. The most outstanding use of HTS materials is the Magnetic Levitation (MAGLEV), which can be used to levitate trains in order to eliminate the resistance between the wheels of the train and the trail. In 2005, by utilizing high temperature superconductor (HTS) electromagnetic coils powered by American Superconductor's HTS wire, the maglev train in Japan attained speeds as high as 500km/h [26].

Fig 1.6 *MAGLEV train in Japan [27].*

1.3.2 Electronics

The so-called Josephson junction, which is composed of a sandwich structure “superconducting layer-insulating layer-superconducting layer” has been introduced in some electronic applications, such as Superconducting Quantum Interference Device (SQUID) [28]. This kind of device can detect very tiny changes in magnetic fields, thus can be used to find out the disease in human being’s brain, heart or liver.

1.3.3 Motor Technology

By using superconducting coils, the size of motors can be dramatically decreased to a certain level, while generating the same power as traditionally used copper-coiled motors [29]. The size-reduced motors can be well used as ship propulsion systems and especially wind turbines, which are relating to the research described in this thesis. On the other hand, concerning the potential development of off-shore wind farms, the use of superconducting wires can also remarkably decrease the current loss during the current transmission across long distance in sea.

1.4 Introduction to YBCO

1.4.1 Microstructure of YBCO

Normally, high temperature superconductor (HTS) materials have multi-layered, oxygen-deficient perovskite structures, in which fourfold planar coordinated Cu-O layers effectively form conducting sheets parallel to the *a-b* plane, which are responsible for the superconductivity [30]. In the case of YBCO, a single unit cell is based on a tri-layered perovskite structure. It centers on a Y layer, around which are stacked the CuO_2 planes and a double charge-reservoir layer of O-Ba-O and O-Cu, which provides charge carriers to the CuO_2 planes. The microstructure of YBCO is illustrated in **Fig 1.7**.

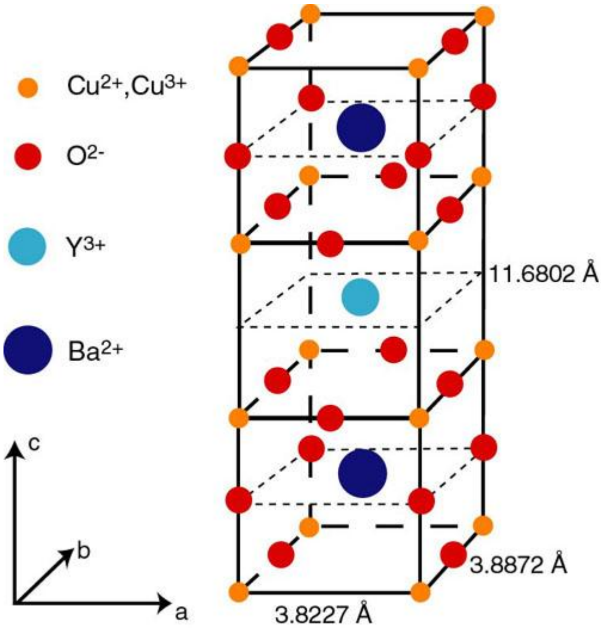

Fig 1.7 *Structure of a single unit cell of YBCO [31].*

1.4.2 Oxygen Stoichiometry

While transfering O to O^{2-}, the electrons need to transit through the CuO_2 plane in order to keep the electrical neutrality. Due to the absence of electrons, the so-called electron hole is naturally formed, which is believed to be the charge carriers that can give rise to extremely high superconducting currents [32]. The charge carrier density in the CuO_2 planes has dramatic influence in determining the superconducting properties. However, it is highly dependent on the oxygen deficiency of the YBCO structure, which can be intuitively reflected from the value of "x" in the $YBa_2Cu_3O_{7-x}$ formula. As can be seen in **Fig 1.8**, it has been confirmed that when "$x \leqslant 0.6$", YBCO is in orthorhombic superconducting symmetry, and exhibits ordering of oxygen atoms in one-dimensional CuO chains along the b-axis, called metallic chains. In this case, T_c appears to be optimized for $x \approx 0$. In contrast, when "$x \geqslant 0.6$", YBCO is in a tetragonal phase, where the oxygen sites in the CuO chains are occupied randomly, thus the material is insulating [32].

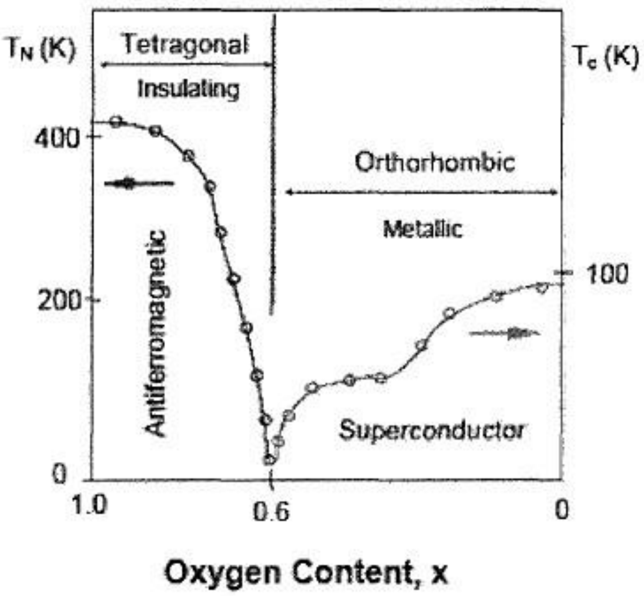

Fig 1.8 *Oxygen content of* $YBa_2Cu_3O_{7-x}$ *[32].*

1.4.3 Anisotropy Factor

Because the superconducting current is carried in the CuO_2 plane, perovskite cuprates superconducting materials are all highly anisotropic. This consequently makes the superconducting parameters ξ (coherence length) and λ (penetration depth) different for parallel to lattice c direction and in the a-b plane, as shown in **Tab. 1.1**. This in consequence leads to difficulties in the production of long wires, as the superconducting grains need to be grown with a preferential orientation, on textured substrates in case of YBCO. Moreover, for the anisotropy of YBCO, grain boundaries (GB) are of considerable importance to the performance, as the current density that can flow through the material is severely limited by the presence of GBs, particularly for those boundaries with misorientation [001] of tilt-angles greater than 10 ° [33]. Transport studies of individual GB in YBCO bi-crystals [34] and coated conductors [35] showed that large-angle grain boundaries act as weak links in the superconductor. Though there are numbers of publications that report the production of randomly oriented YBCO particles through solid reaction, the products are not of high superconducting performance [33, 37].

***Tab 1.1** Coherence length (ξ) and penetration depth (λ) for YBCO at T=0K.*

YBCO	c-axis direction	a-b plane direction
ξ(nm)	890	136
λ(nm)	0.24	1.6

1.5 Development of coated conductor

For the first generation (1G) HTS materials, the $(Bi,Pb)_2Sr_2Ca_2Cu_3O_{10}$ (BSCCO) wires are mainly produced by using the powder-in tube (PIT) process, giving a polycrystalline product. An advantage of BSCCO over YBCO is the smaller sensitivity of its superconducting properties to high-angle grain boundaries and oxygen loss [37, 38]. However, though kilometer-level long length wire products can be routinely manufactured, several disadvantages such as low critical current density under high magnetic fields and high cost of the silver tube, hinders it from vast application in power applications [39].

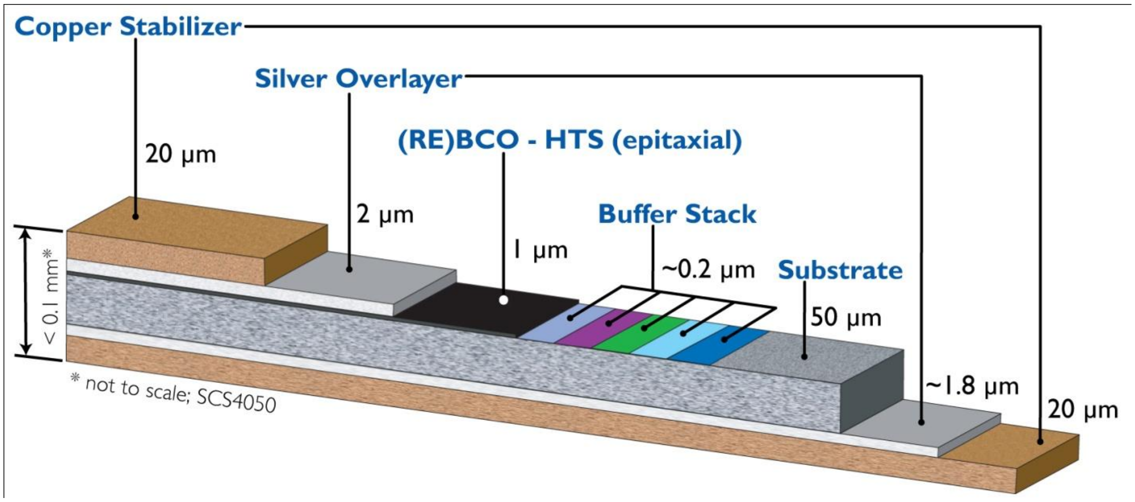

***Fig 1.9** General multilayer architecture of coated conductor [40].*

The concept of "second generation" (2G) HTSC wires was foreseen as an alternative to the powder-in-tube method in order to exploit the capacity of carrying high current density in the environments of high-field and low-temperature with the YBCO superconductor. The basic idea of this 2G wire is that a YBCO superconducting layer can inherit the texture of an underlying substrate having a strong preferential orientation. The requirement for this oriented grain growth is due to the anisotropic properties of YBCO, which have been mentioned above.

This was expected to result in improvements of the wire performance in comparison to the 1G-HTSC-technique, which in the case of YBCO produced a randomly oriented polycrystalline core. The disappointingly low critical current density of these wires did not even result in any significant improvement compared to conventional copper wires [41]. Advantages such as high current density, low energy losses, and possible applications in high magnetic fields are the key factors pushing forward the development of the coated conductors. However, the manufacturing process of these coated conductors is never as easy as that of 1G HTS wires.

The basic idea of depositing a HTSC film on a flexible and inexpensive substrate with a proper texture in long length makes the selection of the substrate always a very important point when considering producing a coated conductor. When depositing a YBCO superconducting layer, the YBCO grains must be grown with preferred orientation both out-of-plane in order to prevent the vertical growth of Cu-O planes, which act as barriers to the current flow, and in-plane to reduce the effect of weak links induced by the grain boundaries [42, 43]. This means that the potential substrates should have “a” and “b” lattice constants similar to those of YBCO, hence of low “misfit” to YBCO. Besides lattice match, other factors should be taken into account for the substrate selection like dielectric and magnetic properties, mechanical performance, chemical compatibility, and suitable thermal expansion coefficients [44]. As can be seen from **Tab 1.2**, sapphire (Al_2O_3), strontium titanate ($SrTiO_3$), magnesium oxide (MgO), yttrium stabilized zirconate (YSZ), and lanthanum aluminate (LAO) could well meet the requirements for the substrate. Due to its balanced property, LAO is used in our experiments for all films grown on single crystals.

However, for making long and flexible YBCO tapes, the use of metallic substrates is necessary. Silver is in principle one of the most promising materials, due to its advantages such as being non-magnetic and nonpoisonous to YBCO. However, its softness and low melting point make it not actually applicable for use [45]. Instead, the most popular materials used nowadays for YBCO deposition are Ni and NiW alloys due to their good stability and low cost compared to a silver tape, in spite of their magnetism [46]. This kind of substrates is named as RABiTs (Rolling assisted biaxially textured substrate) substrates. However, the trade off is a chemical reaction between Ni and YBCO during the formation of the superconducting layer in an oxygen-containing atmosphere. For this reason, the use of a buffer layer becomes necessary to prevent the potential diffusion of metal atoms up into the superconductor as well as the oxidation of the metal [47]. Hence, the classical “alloy substrate-buffer layer-superconducting layer” tri-layer structure has been established and intensively developed during the past two decades in the aim of the industrialization of 2G HTSC materials.

Tab 1.2 *Room temperature properties of the commonly used materials for substrates and buffer layers [39].*

Materials	**Crystal structure**	**Lattice constant (nm)**	**Plane space d (nm)**	**Misfit to YBCO (%)**	**Dielectric constant**	**a (10^{-6}/℃)**	**Melting point (℃)**
CeO_2	Cubic (CaF_2)	0.5411	0.3826	-0.62	15	9.9-13.2	2600
$SrTiO_3$	c.p.	0.3905	0.3905	+1.43	300	10.4	2080
$LaAlO_3$	r.p.	0.3792	0.3792	-1.51	25.4	9.2	2100
$LaMnO_3$	c.p.	0.3880	0.3880	+0.78			
$La_2Zr_2O_7$	c.p.	1.0786	0.3813	-0.96			
Y_2O_3	Cubic (Mn_2O_3)	1.055	0.3723	-3.3	13	8.5	2400
Al_2O_3 (sapphire)	hexagonal	a=0.4758 c=1.299			11.5-9.4	8.31-9.03	2040

Keys: values at room temperature unless otherwise stated;

r.p.: rhombohedral perovskite c.p.: cubic perovskite

Besides the RABiTs technique, another different coated conductor manufacturing technique, which is called “IBAD” has been developed. IBAD stands for ion beam assisted deposition [48, 49]. In this process, the stacked tri-layer structure is also applied, but the texture of the metal substrate is not required. This is because the preferred orientation of YBCO is inherited from the buffer layer, which is deposited with the help of a simultaneous ion (O or Ar) beam bombardment to ensure a strong <100> biaxial texture. However, due to the disadvantages as high equipment cost and very slow deposition rate, this technique will not be used in our research, though it is promising for obtaining higher quality YBCO superconducting thin films compared to RABiTs [50, 51].

1.6 Introducion to deposition techniques

Combined with the use of RABiTs metal substrates, high-performance YBCO films can be grown via two categories of deposition techniques. One is in-situ technique, where the YBCO phase is formed as the material is being deposited, while another is ex-situ technique, where YBCO is formed from precursor materials already deposited on the substrate. Among all the in-situ technologies, Pulsed Laser Deposition (PLD), Liquid Phase Epitaxy (LPE), and Metal-Organic Chemical Vapour Deposition (MOCVD) methologies have been successfully developed [52-56]. The remarkable high J_c values of the products and precise control of the film growth at the atomic level which allows accurate introduction of flux pinning centers and partial substitution of rare-earth elements, make the in-situ techniques superior to the ex-situ techniques. However, the other side of this coin is the required expensive vacuum systems and high-power UV lasers which are disadvantages for commercial use since these aspects contribute to the costs of the wires. As a substitute to the in-situ technologies, the ex-situ ones, particularly the Chemical Solution Deposition (CSD) emerged and attracted much interest worldwide due to its low cost and ease of scaling up. For this reason, the CSD method was applied to the synthesis of YBCO superconducting layers in our investigations. A detailed introduction to the CSD method will be given in Chapter 3.

References

[1] H. K. Onnes, The liquefaction of Helium 1908, *KNAW proceedings*, 11.

[2] H. K. Onnes, Further Experiments with Liquid Helium C. On the Change of Electric Resistance of Pure Metals at Very Low Temperatures VI. The Resistance of Pure Mercury at Helium Temperatures 1911, *Chem. Phys. Lett*. 120 (b).

[3] D. C. Larbalestier, A. Gurevich, D. M. Feldmann, A. Polyanskii, *Nature*, **414** (2001) 368-377.

[4] D. Dew-Hughes, *Low Temperature Physics*, **27** (2001) 967-979.

[5] M. K. Wu, Z. R. Ashburn, C. J. Torng, P. H. Hor, R. L. Meng, L. Gao, Z. J. Huang, Y. Q. Wang, C. W. Chu, *Physics Review Letters*, **58** (1987) 908-910.

[6] W. Meissner, R. Ochsenfeld, *Naturwissenschaften*, **21** (1933) 787.

[7] F. London, H. London , *Proc. Roy. Soc. (London)*, **A149** (1935) 71.

[8] http://www.superox.ru/en/superconductivity.htm

[9] A. C. Rose-Innes, E. H. Rhoderick, *Introduction to Superconductivity*, 1978, Pergamon.

[10] M. Cyrot, D. Pavuna, *Introduction to Superconductivity and High-T_c Materials, World Scientific*, (1992).

[11] C. P. Bean, *Review of Modern Physics*, 36 (1964) 31.

[12] E. M. Gyorgy, R. B. Van Dover, K. A. Jackon, L. F. Schneemeyer, and J. V. Waszczack, *Applied Physics Letters*, **55** (1989) 283-285.

[13] J. G. Bednorz, K. A. Muller, Z. Phys. *B-Condensed Matter*, **64** (1986) 189.

[14] http://www.ccas-web.org/superconductivity/#image

[15] H. Maeda, Y. Tanaka, M. Fukutomi, T. Asano, *Japanese Journal of Physics*, **27** (1988) L209-L210.

[16] Z. Z. Sheng, A. M. Hermann, *Nature*, **332** (1988) 138-139.

[17] S. N. Putilin,E. V. Antipov, O. Chmaissem, M. Marezio, Superconductivity at 94K in HgBa2CuO4+δ, **363** (1993) 56-58.

[18] A. Schilling, M. Cantoni, J. D. Guo, H. R. Ott, *Nature*, **363** (1993) 56-58.

[19] C. W. Chu, L, Gao, F. Chen, Z. J. Huang, R. L. Meng, Y. Y. Xue, *Nature,* **365** (1993) 323-325.

[20] J. Nagamatsu, N. Nagawa, T. Muranaka, Y. Zenitani, J. Akimitsu, *Nature*, **410** (2001) 63-64.

[21] Y. Kamihara, T. Watanabe, M. Hirano, H. Hosono, *Journal of American Chemistry Society*, **130** (2008) 3296-3297.

[22] Z. A. Ren, W. Lu, J. Yang, W. Yi, X. L. Shen, Z. C. Li, G. C. Che, X. L. Dong, L. L. sun, F. Zhou, Z. X. Zhao, *Chinese Physics Letters*, **25** (2008) 2215-2216.

[23] M. Putti, L. Pallecchi, E. Bellingeri, M. R. Cimberle, M. Tropeano, C. Ferdeghini, C. Palenzona, A. Yamamoto, J. Jiang, J. Jaroszynski, F. Kametani, D. Abraimov, A. Polyanskii, J. D. Weiss, E. E. Hellstrom, A. Guresich, D. C. Larbalestier, R. Jin, B. C. Sales, A. S. Sefat, M. A. McGurie, D. Mandrus, P. Cheng, Y. Jia, H. H. Wen, S. Lee, C. B. Eom, *Superconductor Science and Technology*, **23** (2010) 034003.

[24] J. Williams, *IEEE T. Nucl. Sci*. **31** (1984) 994-1005.

[25] H. S. Chen, T. N. Cong, W. Yang, C. Q. Tan, Y. L. Li, Y .L. Ding, *Prog. Nat. Sci*. **19** (2009) 291-312.

[26] http://www.ornl.gov/sci/oetd/news/american_superconductor.htm

[27] http://blogs.discovery.com/news_tech_nfpc/engineering/

[28] H. Hilgenkamp, J. Mannhart, *Rev. Mod. Phys*. **74** (2002) 485-549.

[29] C. Lewis, J. Mueller, *IEEE Power Engineering Society General Meeting*, (2007) 3638-3645.

[30] J. D. Jorgensen, B. W. Veal, A. P. Paulikas, L. J. Nowicki, G. W. Crabtree, H. Claus, and W. K. Kwok, *Physics Review B*, **41** (1990) 1863-1877.

[31] http://tfy.tkk.fi/aes/AES/projects/prlaser/supercond.htm

[32] L. T. Wille, A. Berera, and D. de Fontaine, *Phy. Rev. Lett*, **60** (1988) 1065-1068.

[33] H. C. Freyhardt, J. Hoffmann, J. Wiesmann, J. Dzick, K. Heinemann, A. Isaev, F. arcia-Moreno, S. Sievers, A. Usoskin, *IEEE Trans. Appl. Supercond*, **7** (1997) 1426-1431.

[34] D. Dimos, P. Chaudhari, J. Mannhart, *Phys. Rev. B*, **41** (1990) 4038-4049.

[35] D. T. Verebelyi, D. K. Christen, R. Feenstra, C. Cantoni, A. Goyal, D. F. Lee, M. Paranthaman, P. N. Arendt, R. F. DePaula, J. R. Groves, C. Prouteau, *Appl. Phys. Lett*, **76** (2000) 1755-1757.

[36] S. Narike, N. Sakai, M. Murakami, I. Hirabyashi, *Superconductor Science and Technology*, **17** (2004) S30-S35.

[37] A. Yıldız, K. Kocaba, G. Akyüz, *Journal of Superconductivity and Novel Magnetism*, **25** (2012) 1459-1467.

[38] Q. Li, G. N. Riley, R. D. Parrella, S. Fleshier, M. W. Rupich, W. L. Carter, J. O. Willis, J. Y. Coulter, J. F. Bingert, V. K. Sikka, J. A. Parrell, D. C. Larbalestier, *IEEE Trans. Appl. Supercond*. **7** (1997) 2026-2029.

[39] E. E. Hellstrom, Y. Yuan, J. Jiang, X. Y. Cai, D. C. Larbalestier, Y. Huang, *Supercond. Sci. Technol*. **18** (2005) S325-S331.

[40] http://www.superpower-inc.com/content/2g-hts-wire

[41] M. Guillaume, P. Allenspach, E. D. Specht, *Appl. Super*, **4** (1996) 403.

[42] T. J. Zhang, K. G. Wang, S. Q. Wang, F. S. Liu, *Supercond. Sci. Technol.* **3** (1990) 445.

[43] K. Cha, M. S. Colclough, S. M. Garrison, N. Newman, G. Zaharchuk, *Applied Physics Letters*, **59** (1991) 733.

[44] J. M.Phillips, *Journal of Applied Physics*, **79** (1996) 1829-1848.

[45] Y. Xu, D. Shi, A review of coated conductor development, *Tsinghua Sci. and Technol*, 8 (2003).

[46] N. Cheggour, J. W. Ekin, C. C. Clickner, Transverse compressive stress effect in Y-Ba-Cu-O coatings on biaxially textured Ni and Ni-5at.%W substrates, *Applied Superconductivity Conference* (2002).

[47] D. C. Larbalestier, A. Gurevich, D. M. Feldann, A. Polyanskii, *Nature*, **414** (2001) 368-377.

[48] Y. Lijima, N. Tanabe, O. Kohno, Y. Ikeno, *Applied Physics Letters*, **60** (1992) 769-771.

[49] R. P. Reade, P. Berdahl, R. E. Russo, S. M, *Applied Physics Letters*, **61** (1992) 2231-2233.

[50] M. Majoros, R. I. Tomov, B. A. Glowacki, A. M. Campbell, *IEEE Trans Appl. Supercond*, **13** (2003) 3626.

[51] A. Gupta, E. I. Cooper, R. Jagannathan, E. A. Giess, *ACS Symposium Series*, 377 (1988) 265.

[52] T. Manabe, I. Yamaguchi, S. Nakamura, W. Kondo, T. Kumagai, S. Mizuta, *Journal of Materials Research*, **10** (1995) 1635-1643.

[53] K. Yamagiwa, T. Araki, Y. Takahashi, H. Hier, S. B. Kim, K. Matsumoto, J. Shibata, T. Hirayama, H. Ikuta, U. Mizutani, I. Hirabayashi, *Journal of Crystal Growth*, **229** (2001) 353-357.

[54] J. A. Smith, M. J. Cima, N. Sonnenberg, *IEEE Trans. Appl. Supercond*. **9** (1999) 1531-1534.

[55] O. Castano, A. Cavallaro, A. Palau, J. C. Gonzalez, M Rossell, T. Puig, F. Sandiumenge, N. Mestres, S. Pinol, A. Pomar, X. Obradors, *Superconductor Science and Technology*, **16** (2003) 45-53.

[56] T. Araki, I. Hirabayashi, *Superconductor Science and Technology*, **16** (2003) R71-R94.

Chapter 2

Experimental

2.1 Preparation of Single Crystal Substrates

Throughout the thesis, water-based precursor solutions and methanol-based precursor solutions were applied in synthesizing YBCO superconducting films. Owing to its negligible interfacial reaction and lattice mismatch with YBCO, LAO single crystals have been demonstrated as being amongst the most promising substrates for producing YBCO prototypes at laboratory scale. However, in our work, the wetting property of LAO was found to be strongly dependent on the surface quality when using water-based precursors for coating. This is mainly due to the bad wetting behavior of the water-based solution, as the polarity and cohesive hydrogen bonding between water molecules lead to a very high surface tension, which needs elimination during coating of various materials. To improve the wettability, a pretreatment of the LAO single crystals was routinely applied, as it can not only eliminate the dislocations and surface defects, but most importantly can create an advantageous terrace morphology on the LAO surface [1, 2], which was found extremely beneficial to the coating behavior. During the pretreatment, firstly the LAO substrates were cleaned in trichloroethylene, acetone, and methanol in an ultrasonic bath for 5 minutes. Thereafter, a heat treatment was performed on the substrates at 700℃ for 10 hours in flowing oxygen. **Fig 2.1** shows the influence of LAO pretreatment to the wettability between the water-based precursor solution and the LAO substrates when using the dip-coating technique. It is obvious that without the pretreatment, the solution could not totally cover the substrate surface even at a low withdrawing speed of 5cm/min. After the pretreatment, the surface coverage was dramatically improved, however, with the withdrawing speed increasing from 5cm/min to 15cm/min, excess solution was agglomerated at the bottom part of the substrates, which is marked by white lines in **Fig 2.1**. Spin-coating was also tried for the deposition of water-based precursors. However, rotating speeds ranging from 2000rpm to 8000rpm all showed bad coating quality of the films, indicating an inadaptability of spin-coating to our water-based precursor solutions.

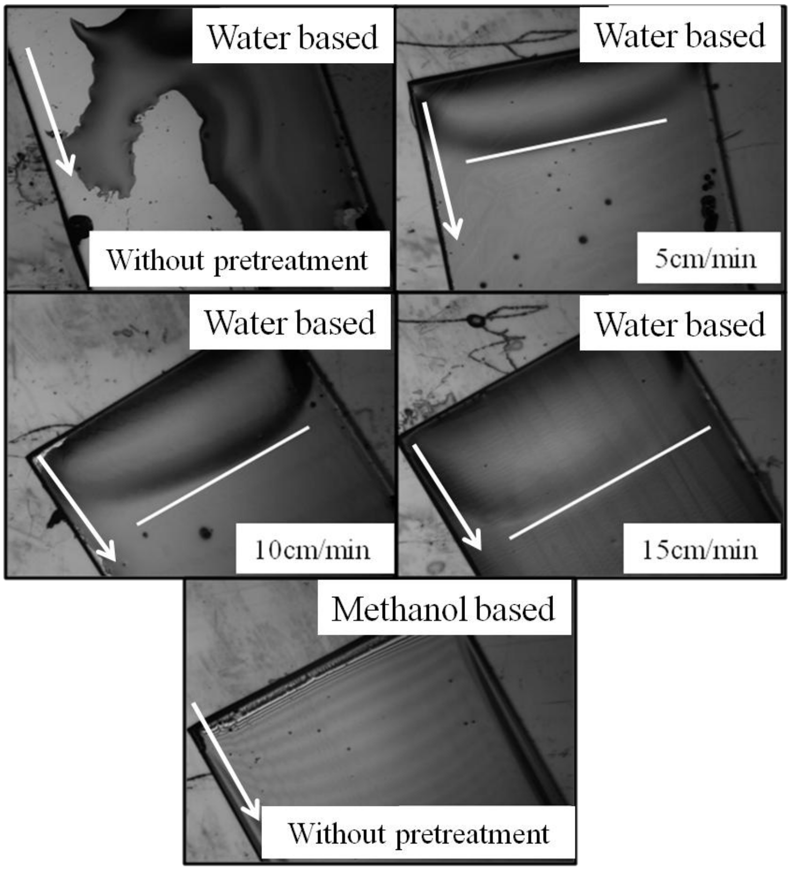

Fig 2.1 *Influence of LAO single crystal pretreatment on the solution wetting property by using water-based solvent and methanol –based solvent. The water-based solvent and the methanol based solvent were coated onto the LAO single crystals without pretreatment at withdrawing speeds of 5cm/min and 40cm/min, respectively. The arrows indicate the withdrawing directions.*

In contrast, thanks to the low surface tension of methanol, the wettability of methanol-based precursor solutions was excellent for both dip-coating and spin-coating, and the substrate surface was totally covered by the solution. However, as shown in **Fig 2.1**, by using dip-coating even at a high withdrawing speed of 40cm/min, which resulted in a short vertical coating period, the high volatility of methanol resulted in a clear striped morphology, which implies a gradual thickness increase from the bottom to the upper side. Thus to ensure the thickness homogeneity, spin-coating was applied for the coating of methanol-based precursor solutions.

2.2 XRD Measurement

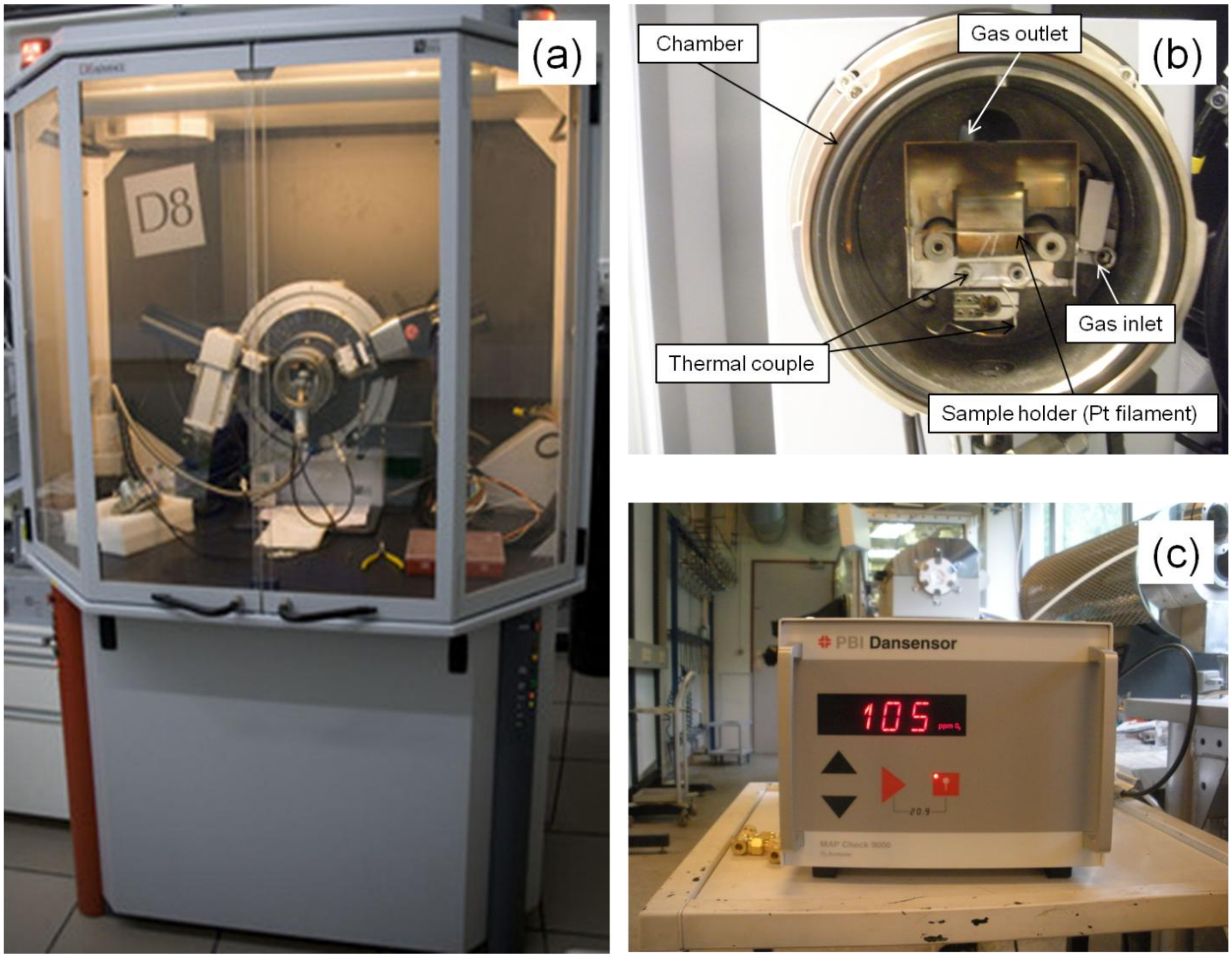

Fig 2.2 *(a) BrukerD8 Advance x-ray diffractometer; (b) Structure of the high-temperature chamber; (c) Oxygen sensor monitoring the oxygen content at the gas outlet.*

In this work, the X-ray diffraction technique was used to characterize the phase content and evaluate the texture of the samples. All the experiments were performed in a BruckerD8 Advanced x-ray diffractometer with a voltage of 20kV and a current of 20mA, respectively. The X-rays were generated by a Cu anode producing Cu-$K_{\alpha}1$ and Cu-$K_{\alpha}2$ radiations with wave lengths of 1.5406Å and 1.5444Å, respectively, with a relative intensity ratio Kα2/Kα1 of 0.5. Additionally, some reflections resulting from the W Lα series radiation is also present in the 2θ spectrums. For the theta-2theta measurements at room temperature, the coupled step-scan mode was used and the data were collected at a step size of 0.05 °and a scanning speed of 1deg/min.

For the in-situ theta-2theta measurements at high temperatures, a scanning mode similar to that used at room temperature was applied. Each scan was started five minutes after having reached the target temperature. During high-temperature measurements, platinum filaments with 1cm-width were used as the sample holder, beneath which a thermal meter was wield to monitor the temperature. Ar/O_2 mixed gases with different oxygen partial pressures were used to evaluate the effect of the annealing atmosphere. The oxygen sensor (MAP Check 9000 O_2 analyser, PBI Dansensor) was connected to the outlet of the chamber. The setup of the in-situ equipment is shown in **Fig 2.2**.

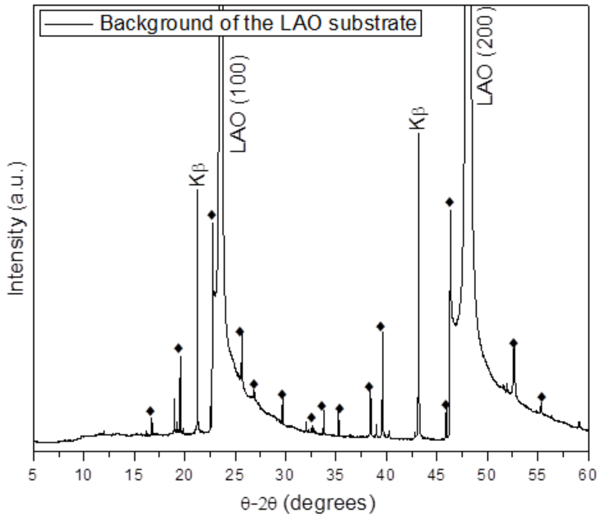

Fig 2.3 *XRD pattern of a LAO substrate.*

The texture scans of the films were performed on a four-circle cradle stage with a scintillation detector and energy resolution. A schematic view of the four-circle stage is shown in **Fig 2.4**. During in-plane and out-of-plane scannings, the angle 2θ, corresponding to the angle between the incident beam and the detector, was kept constant. In particular, for the in-plane texture measurements on the YBCO films, the (103) peak of YBCO was selected, thus 2θ was kept at approximately at 32.8° (depending on the situation of the alignment), and χ was kept at approximately at 45.1 °, which is corresponding to the angle between the YBCO(103) planes and the horizontal plane. By rotating φ from 0° to 359°, four peaks appear in the spectrum, due to the symmetry of the perovskite structure of YBCO. The in-plane texture was qualified by averaging the FWHM (full-width at half maximum) values of the four peaks. For the out-of-plane texture evaluation, measurements were performed with the (005) peak of YBCO, thus 2θ and χ were kept at approximately 38.5° and 0°, respectively. By rotating ω by 5° around the maximum position, we obtained a rocking curve of the (005) reflection, the FWHM value of which was then used to quantify the out-of-plane texture quality.

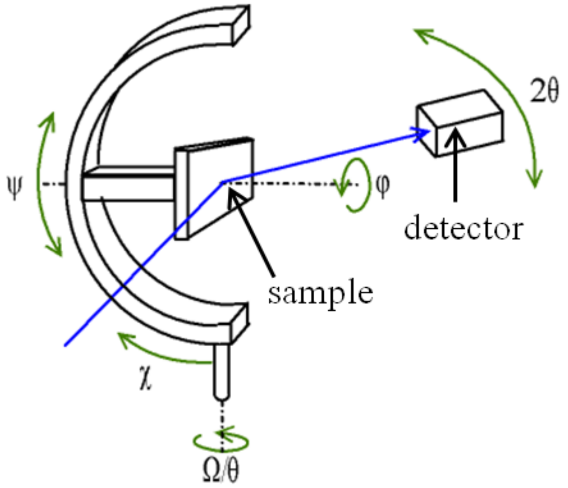

Fig 2.4 *Schematic view of the four-circle sample stage displaying the three rotation angles (χ, φ, ω) and the sample reference system.*

2.3 Thermal decomposition analysis

Thermogravimetry (TG) and differential thermal analysis (DTA) measurements were performed on powder samples to investigate the thermal behavior of precursors and the reaction processes during YBCO formation by using a model STA 449C from Netzsch TG/DTA instrument. During the measurements, different atmospheres were used by introducing pure oxygen or argon gas all at a flow rate of 40ml/min. Before analysis, all the results were corrected with the baseline, which was collected on empty the aluminum oxide crucibles that were going to contain the powder samples thereafter. The powder samples were prepared by heating over night on a heating plate at suitable temperatures, and then being ground into fine powders in order to decrease the effect of the particle size.

2.4 SEM and AFM

The Surface morphology of the films was studied by using a scanning electron microscope (SEM) and an atomic force microscope (AFM) from Zeiss and DME, respectively. The SEM device was equipped with an energy-dispersive X-ray (EDX) detector from Thermo-electron corporation. During the investigation, the mode of secondary electrons emission was used for observing the crystallized thin films, while the mode of In-lens field emission was used for observing the pyrolyzed amorphous thin films, due to their poor conductivity.

2.5 DC magnetization

The magnetization hysteresis loops of the YBCO films were measured by a vibrating sample magnetometer (VSM) in a cryogen-free measurement system (CFMS) from cryogenic Ltd. A sketch of the VSM system is shown in **Fig 2.5**. During the measurement, the film sample is placed inside the cryostat and then mechanically vibrated in a constant magnetic field. The signal induced in the pickup coils is measured. In the studies, the applied field was ranging from -5T to 5T and perpendicular to the a-b plane of the YBCO films.

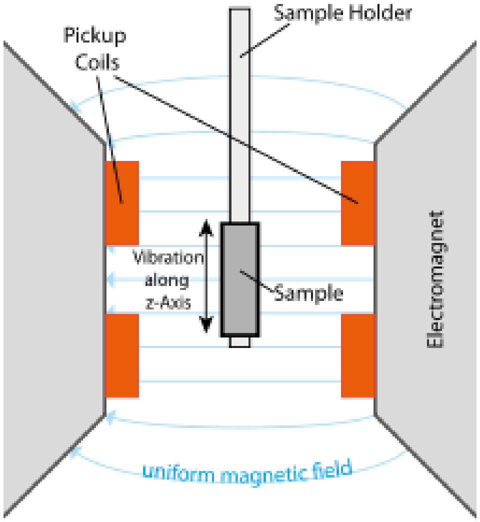

Fig 2.5 *Schematic presentation of the VSM setup.*

As mentioned in the first chapter, from the hysteresis loops, the J_c value of the films can be calculated by using the Bean model for square films,

$$Jc = \frac{20\Delta M}{V\mathrm{a}(1-a/3b)}$$

Where, ΔM is corresponding to the opening of the magnetization hysteresis loop, a and b are the width and the length of the film sample (a<b), respectively, V is the volume of the film.

References

[1] J. Yao, P. B. Merrill, S. S. Perry, D. Marton, J. W. Rabalais, Journal of Chemistry Physics, 108 (1998) 1645.

[2] H. R. Yi, Z. G. Ivanov, D. Winkler, Y. M. Zhang, Applied Physics Letters, 65 (1994) 1177.

Chapter 3

Review and trial of CSD processes

In this chapter, depending on the barium products present after the decomposition of the organic precursors, the main CSD processes are classified into four categories, which are the barium fluoride process (TFA-MOD), barium hydroxide process (TMAP-MOD), barium nitrate process (PAD), and barium carbonate process (FF-MOD). This is motivated by the significant role that the barium intermediate phases play during the formation of the YBCO superconducting phase.

3.1 Background of ex-situ CSD techniques

Compared to the PLD and CVD techniques, the CSD techniques have advantages such as precise control of composition, high speed, and low-cost [1, 2], thus in the past two decades, substantial efforts have been devoted to the improvement of the ex-situ CSD deposition techniques in the aim of producing high-quality YBCO coated superconductors [3, 4]. Normally, a CSD technique can be divided into several steps: 1) Solution preparation: is on the one hand to ensure homogeneous dispersion of the metal cations without precipitation, on the other hand to obtain a proper viscosity, which can significantly affect the wetting property of the solution on the substrate and the thickness of a mono-layer; 2) Pyrolysis: is to decompose organic compounds, which are introduced by using the organic chelating agents, metallorganic salts, and solvents, giving rise to the formation of simpler yttrium, barium and copper compounds. A precise control during this process is essential for obtaining good macro structure of the final thin film products, as severe combustion of the organic compounds and abrupt gas emission may result in macro-cracks and high porosity in the films; 3) Annealing: is to form YBCO phase. Normally an inert gas atmosphere (N_2 or Ar) with low oxygen content (100-500ppm) is required for preparing YBCO thin films, as the use of low oxygen partial pressure can on the one hand facilitate the liquid phase formation, which is demonstrated as being responsible for the grain growth with preferred orientation and enhancing the interconnection between the YBCO grains, on the other hand low O_2 helps reducing the risk of oxidation of the metal substrates; 4) Oxygenation: is to transform YBCO phase from semiconducting tetragonal symmetry to superconducting orthorhombic symmetry.

Unfortunately, the early research on the CSD techniques failed in producing high quality YBCO films [5]. Scientists used to assign the low performance to the agglomeration of $BaCO_3$ at grain boundaries, which could severely hinder superconducting currents flow in the YBCO films [5]. In 1988, the Trifluoroacetates Metalorganic Deposition (TFA-MOD) process was was shown to be promising for fabricating YBCO films with high critical current densities (J_c) and thus became an alternative to the traditionally used CSD techniques and attracted extensive interest in the following years [6-8]. By using TFA precursor salts, BaF_2 appears to form as the substitute to $BaCO_3$ after decomposition of the organic compounds, due to the higher stability of BaF_2 compared to that of $BaCO_3$ [9].

However, with further development of the CSD techniques, because of their faster decomposition process and the relatively environmentally benign nature of the solvent [10], the non-fluorine sol-gel techniques were gradually found worthy of further investigation in order to enhance the productivity and improving the environmental safety in spite of the undesired formation of $BaCO_3$ after pyrolysis. In the non-fluorine sol-gel processes that were explored before the advent of the TFA-MOD, metal alkoxides were generally used as the metal-organic precursors for fabricating textured YBCO films [11]. By using alkoxides, the chemical homogeneity of the resulting gel was found to strongly depend on the reactivity of the individual metal alkoxides towards water or methanol. The fact that the hydrolysis and condensation rates of different metal alkoxides are generally different results in the formation of different sized clusters in the sol, which gives rise to inhomogeneity of the resulting gel. Difficulties then occur when using metal alkoxides that have very different rates of hydrolysis, such as those for rare-earth alkoxides and Cu-alkoxides, where the former are much more readily hydrolyzed than the latter even by very small amount of water [12]. Consequently, segregation of rare-earth elements can occur during the hydrolysis-condensation-polymerization process, which in turn makes it difficult to prepare homogeneously mixed rare-earth and Cu oxides of the required stoichiometry

[13]. To avoid the use of alkoxides and fluorides, some groups have applied other organic compouds as substitutes, for example trimethylacetates [14], acetylacetonates [15], nitrates [16] and ethylhexanoates [17]. Among all the existing non-fluorine CSD methods, depending on the choice of the organic compounds, the most commonly used solutions used to be categorized into: 1) chelating processes that using chelating agents to reduce the hydrolysis of the metal cations; 2) metal organic deposition (MOD) processes using high-molecular-weight, water-insensitive carboxylate precursors; 3) polymerized complex processes that use polymers to strongly bind the metal cations to the linear polymer chains in the precursor matrix. In contrast, in our research, another concept is introduced for categorizing the CSD methods. Depending on the barium products present after the decomposition of the organic precursors, the main processes are classified into several categories, barium hydroxide process, barium nitrate process, and barium carbonate process.

3.2 TFA-MOD process

3.2.1 Review of TFA-MOD process

Nowadays, the trifluoroacetate metalorganic deposition process (TFA-MOD) still remains the most promising route among the ex-situ CSD techniques for depositing high-quality YBCO superconducting thin films. The TFA-MOD route was initially reported by Gupta in 1988 [18] and has been intensively developed for more than two decades. In the very early stage of the development, the precursor solution was prepared by mixing Y_2O_3, $BaCO_3$, and metallic copper, followed by reaction with trifluoroacetic acid to give the products of $Y(TFA)_3$, $Ba(TFA)_2$, and $Cu(TFA)_2$. Finally, methanol was used to dissolve the produced trifluroacetate powders into a solution with the desired metal cation concentration and viscosity. After a pyrolysis process from room temperature up to 400℃ under oxygen gas flow with controlled water partial pressure, most of the organic compounds are removed to yield Y_2O_3, BaF_2, and CuO as the intermediate products before further transformation to YBCO phase. The purpose of the introduced water is to prevent the sublimation of the copper salts, which could lead to off stoichiometry in the final sintered films. However, during pyrolysis, the generation of the hazardous and corrosive HF gas requires that the ramping speed must be controlled at a very low level to prevent the formation of cracks, hence a very long duration is normally required by the TFA-MOD process, which necessitates more than 20 hours to yield a 200nm thick YBCO superconducting layer. After pyrolysis, the film is transformed into the YBCO tetragonal phase by increasing the temperature up to 750-800℃, where a ～50% reduction in thickness takes place. During annealing, water partial pressure is also necessarily introduced to help the removal of HF. The overall reaction that occurs during YBCO formation is presented in the following equation:

$$0.5Y_2O_3 + 2BaF_2 + 3CuO + 2H_2O \rightarrow YBa_2Cu_3O_{7-x} + 4HF\ (g) \quad (1)$$

By optimizing the parameters used throughout the manufacturing process, high critical current densities above 1MA/cm^2 (77K self-field) were first obtained on YBCO thin films produced via the TFA-MOD route in 1990 [19]. Now the TFA-MOD technique is better known and a well established sol-gel route used by several groups towards YBCO coated conductor fabrication [20-22]. American Superconductor Corporation (AMSC) has adopted the combination of TFA-MOD/RABiTs technology to produce YBCO long tapes (2G wire) for high-power application based on the low production price/performance ratio of the process [23]. However, although being a mature technique suitable for wide range of applications, the TFA-MOD process is still under development, particularly due to its time-costing pyrolysis process, which makes its productivity limited to quite a low level. Also for this reason, some low-fluorine and fluorine-free MOD methods have emerged as alternative candidates.

3.2.2 Trial of TFA-MOD process

In our research, in order to evaluate the potential of using candidate non-fluorine CSD processes, the traditional TFA-MOD process was initially applied to produce YBCO thin films, the microstructure and performance of which could give a reference target when trying to improve selected non-fluorine MOD methods.

In this work, the TFA-MOD precursor solution was produced by initially mixing acetates of Y, Ba and Cu (Alfa Aesar) at the molar ratio of 1:2:3. After five hours' continuous stirring in deionized water at 80℃, all the powders were dissolved resulting in a clear blue solution without any precipitation. Afterwards, trifluoroacetic acid was added at the ratio of metal: acid = 1:2 to chelate all the metal cations. This procedure took another five hours to ensure a full chelation. Finally, all the water and acetic acid generated during the reaction were removed by a rotation evaporator to give a dark blue gel. To coat the precursor onto substrates, a metal concentration of

1.5mol/*l* was favored, as it gives appropriate wetting properties. After the preparation of the precursor, the solution was spin-coated on 5×5mm^2 $LaAlO_3$ (LAO) substrates at a speed of 4000 rpm for 60 seconds.

The precursor films were then decomposed to amorphous films in a tube furnace by slowly heating up to 450℃ over ten hours under humid oxygen gas flow, in order to avoid severe crack formation. After cooling down, the furnace was heated to 760℃ at a ramping speed of 20℃/min and hold at this temperature for one hour under N_2 atmosphere with controlled oxygen and water partial pressure. During the last 10 minutes of holding at 760℃, the atmosphere was switched to dry gas. During cooling down, oxygenation was made at 450-525℃ for five hours in a flow of pure oxygen.

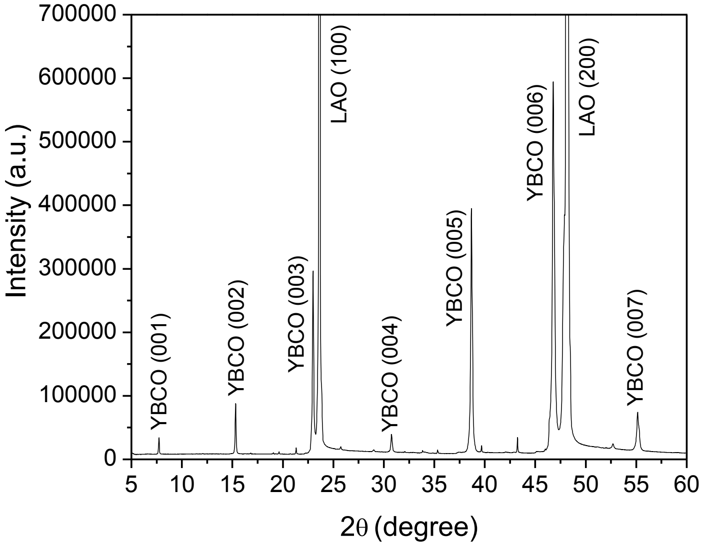

Fig 3.1 *X-ray pattern recorded on a TFA-MOD derived film sample converted at 760 ℃ in an Ar atmosphere containing 100ppm oxygen with a water partial pressure produced by flowing through water bath at 50 ℃.*

Fig 3.1 and **Fig 3.2** show the XRD pattern and a SEM picture of the TFA-MOD derived YBCO mono-layer film deposited on a LAO single crystal substrate. It is clear that liquid phase was formed when the annealing temperature was as low as 760℃, leading to a continuous and crack-free surface morphology. From the XRD pattern, strong (00*l*) peaks were seen, implying a preferred c-axis orientation without randomly oriented grain growth.

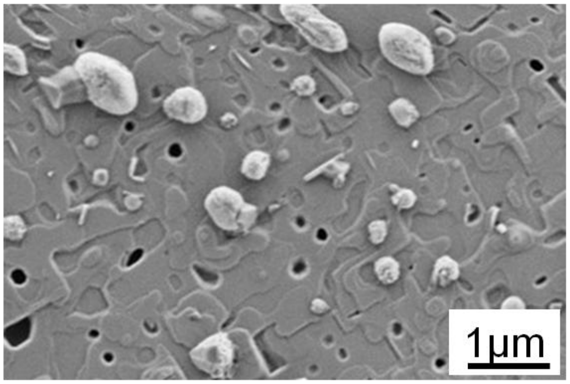

Fig 3.2 *SEM picture of the surface of a TFA-MOD derived film sample converted at 760 ℃ in an atmosphere of Ar with 100ppm oxygen and water partial pressure, which was produced by flowing through a water bath at 50 ℃.*

3.3 Barium hydroxide process

3.3.1 Review of Barium hydroxide process

The use of barium inorganic salts that don't contain carbon can be a promising route for producing high-performance YBCO thin films, if they can form as substitutes to the hard to decompose barium carbonate during the pyrolysis process. Keeping this in mind, the use of barium hydroxide can be a good choice. In 2002, Y. L. Xu et. al firstly reported the barium hydroxide process for producing YBCO thin films [24]. In the publications describing this process, the precursor solution was prepared by dissolving the mixture of barium hydroxide, yttrium trimethylacetate and copper trimethylacetate in propionic acid with the help of xylene, which can dramatically improve the solubility and viscosity of the precursor solution [25]. Because of the use of trimethylacetates as the yttrium and copper organic salts and the propionic acid as the main solvent, this process was briefly named as "TMAP". More importantly, besides the use of barium hydroxide as the starting chemical, the formation of barium hydroxide was further ensured via the introduction of a water partial pressure during the heating treatment. L. Lei et. al [26] demonstrated that proper control over the water vapor partial pressure can convert $BaCO_3$ into $Ba(OH)_2$, and then $Ba(OH)_2$ is used as the barium source to react with CuO and

Y_2O_3 to generate the YBCO phase, thus achieving the purpose of elimination of the $BaCO_3$ phase in the final YBCO films produced by fluorine-free sol-gel process. The formation of the YBCO phase under annealing conditions in the presence of water is shown by the chemical equations (2) and (3).

$$BaCO_3 + H_2O \rightarrow Ba(OH)_2 + CO_2\uparrow \quad (2)$$

$$4Ba(OH)_2 + 6CuO + Y_2O_3 \rightarrow 2YBa_2Cu_3O_{7-x} + xO_2 + 4H_2O\uparrow \quad (3)$$

Besides the demonstrated elimination of the $BaCO_3$ phase, related publications also claimed some other advantages of the barium hydroxide process, such as a long shelf life of more than two years [27], and low mass loss during the decomposition of the organic compounds, which results in a smooth and crackless surface of the pyrolyzed films [28].

In spite of the many advantages mentioned above and having been developed for one decade, the barium hydroxide process nowadays is still being developed by several groups at Cincinati University, Wollongong University and Tsinghua University who originally developed this method [29-35], and has not been successfully reproduced by other groups worldwide. The investigations on this process were also restricted to laboratory scale, as all the reports were describing the deposition of YBCO films on LAO single crystals whereas no reports about film deposition on long length buffered metal substrates were published. Most importantly, the J_c values obtained on the YBCO films derived from the barium hydroxide process were ranging from 0.5MA/cm^2 to 1MA/cm^2, which can hardly meet the requirements for potential large scale production [29-35].

3.3.2 Trial of Barium hydroxide process

To prepare the precursor solution, Barium hydroxide, Yttrium acetate and Copper acetate were mixed at the ratio of Y:Ba:Cu=1:2:3, dissolved in a mixture of propionic acid and ammonia, which was prepared at the volume ratio of 3:1. After one hour stiring at 80℃ on a heating plate, the solution became clear blue without any precipitation. Afterwards, all the extra solvent was removed by an evaporator. During this process, deionized water was added to help the removal of acid until a blue glassy gel was obtained. Finally, the gels were dissolved in methanol (Alfa Aesar), to yield a homogeneous solution with a total metal concentration (Y, Ba and Cu) of

1.5mol/L. The coating process was the same as that used in the TFA-MOD process. Thereafter, the pyrolysis process was performed up to 450℃ under humid oxygen flow during 60 minutes. After cooling down to room temperature, the pyrolyzed films were heated from 20℃ to 760℃, and then held at high temperature for one hour. A mixed gas atmosphere consisting of argon with 100ppm oxygen and water content generated by flowing the gas mixture through a water-bath at 30℃ was running through the tube furnace during the annealing process. During the last ten minutes of annealing, the atmosphere was switched to dry Ar/100ppmO_2. After crystallization, the samples were cooled to 450℃, and held for five hours under an atmosphere of pure oxygen.

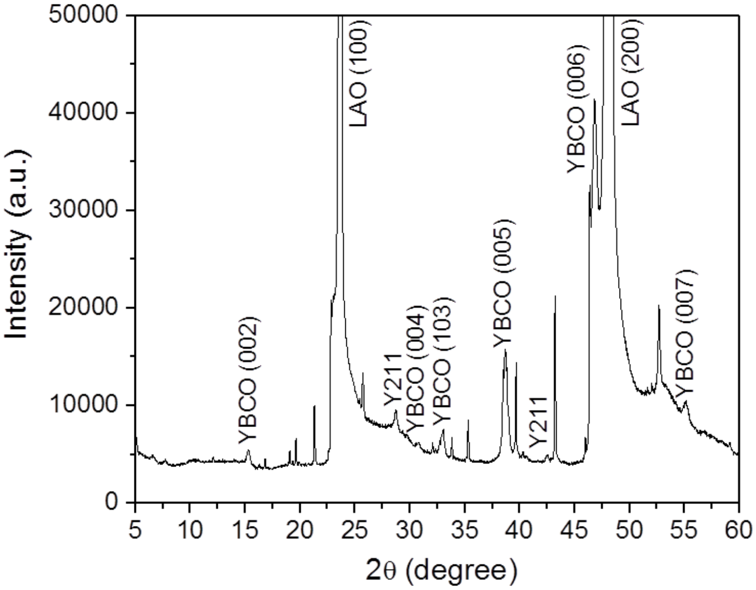

Fig 3.3 *X-ray pattern recorded on the barium hydroxide process derived film sample converted at 760℃ in Ar atmosphere containing 100ppm oxygen with water partial pressure, which was produced by flowing the gas through a water bath at 50℃.*

The XRD pattern and SEM picture of the TMAP process derived YBCO films can be seen on **Fig 3.3** and **Fig 3.4**. In contrast to the smooth and continuous surface obtained by using the TFA-MOD process, the morphology shown in **Fig 3.4** displays a uncontinuous surface, with needle-like grains covering the top of the film, implying an a-axis oriented grain growth. In the XRD pattern, although a-axis oriented grains are absent, the (103) peak of YBCO was clearly observed at 32.5 ° and the intensity of the c-axis peaks are relatively low compared to the TFA-MOD derived films. Besides, the Y_2BaCuO_5 (Y211) phase is also observed in the XRD pattern. According to the previous publications, the Y211 phase is considered as a desired by-product that forms during the partial melting of YBCO at high temperatures, as the Y211 particles can play a role as flux pinning centers which can improve the in-field performance of the YBCO films [36]. However, considering the low annealing temperature used in our experiments, the Y211 formation was probably not due to the YBCO melting, but to the decomposition of YBCO induced by water vapour, as shown in equation (4), which was proposed by L. Dusoulier et. al [37]. This is definitely a negtive sign for the use of water during sintering, as it hampers the formation of a favorable microstruture of YBCO thin films.

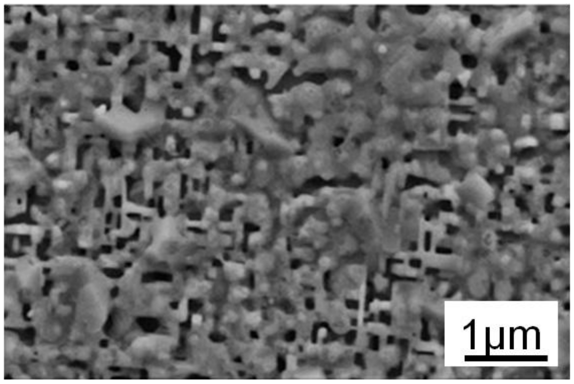

Fig 3.4 *SEM picture of the barium hydroxide process derived film sample converted at 760 ℃ in Ar atmosphere containing 100ppm oxygen with water partial pressure, which was produced by flowing the gas through a water bath at 50 ℃.*

$$YBa_2Cu_3O_{7-x} + 1.5H_2O \rightarrow 2.5CuO + 1.5Ba^{2+} + 3OH^- + 0.5Y_2BaCuO_5 + 0.25O_2 \quad (4)$$

3.4 Barium nitrate (PAD) process

3.4.1 Review of Barium nitrate process

When selecting an appropriate non-fluorine containing metalloganic compound as the substitute to trifluoroacetate, the most primary principle is that the organic anions in it can be decomposed and expelled in gas form during pyrolysis and annealing. Based on this, chlorine and sulphur elements should be avoided, because of the very high stability of chlorides and sulphides. In contrast, nitrates appear to be a possible choice for making YBCO precursors, not only because nitrogen can be expelled in the form of NO and NO_2 gas emission during heat treatment, but also because of the high solubility of the nitrates in polar solvents, which can result in high homogeneity of the precursor solution. The barium nitrate sol-gel process is actually not a novel method for fabricating YBCO superconducting materials, however, in most of the early publications, the method was just used for the synthesis of YBCO powders and bulk materials [38, 39], but not for YBCO thin films. Since 2003, laboratories in America, Spain, Germany, as well as India started efforts aiming at adopting the application of this nitrate-based technique to the synthesis of textured superconducting films and named it as "PAD" process, as polymers were used as assistant during the depositions. PAD is a flexible process for the production of complex oxide coatings. Jia et al. first reported the growth of epitaxial superconducting oxide films by using aqueous PAD in 2004, but J_c was not reported [40, 41]. One year later, Apetrii et al. [42] produced a 250 nm YBCO film by using a non-aqueous PAD process. A J_c value of $1MA/cm^2$ at 77 K was obtained on the YBCO thin film produced by using a "non-aqueous polyacrylic acid–nitrate precursor" solution in dimethylformamide.

Compared to the hydroxide and carbonate processes, the nitrate methods have many advantages. Firstly, in other sol-gel processes the complex solution preparation schemes often require multiple drying and re-dissolving steps, whereas by using the nitrate methods, all nitrates can be directly dissolved in a solvent resulting in a stable aqueous solution. This is one of the most important differences between the PAD processes and other acid-based or alcohol-based processes [40]. Besides, with the help of polyethylene glycol (PEG), the solubility of nitrates can be dramatically improved [43]. Secondly, there is no $BaCO_3$ phase formation during annealing.

However, the aqueous PAD process necessitates a hot coating to improve the concentration of the coating solution, and a rapid drying to prevent crystallization in the wet films [40]. This might be one of the greatest obstacles for the scaling-up of the PAD processes, thus like for the hydroxide processes, investigations on the PAD processes were limited on the deposition of YBCO thin films on single crystals such as LAO and YSZ.

3.4.2 Trial of Barium nitrate process

To prepare the precursor solution used for the Barium nitrate process, Yttrium nitrate, Barium nitrate, and Copper nitrate were initially mixed at the ratio of Y: Ba: Cu =1:2:3, and disolved in deionized water, to give a total metal concentration of 0.5mol/*l*. After that, polyethylene glycol 200 (PEG 200) was added into the solution, leading to a dramatically increase of viscosity, which improves the wetting properties of the solution on single crystal substrates. The coating process was the same as that used in the TFA-MOD process. Thereafter, the pyrolysis process was performed up to 450℃ under humid oxygen flow during 60 minutes. After cooling down to room temperature, the pyrolyzed films were heated from 20℃ to 760℃, and then held for one hour. A mixed gas atmosphere consisting of argon with 100ppm oxygen was flowing throughout the tube furnace during the annealing process. After crystallization, the samples were cooled to 450℃, and held for five hours under an atmosphere of pure oxygen.

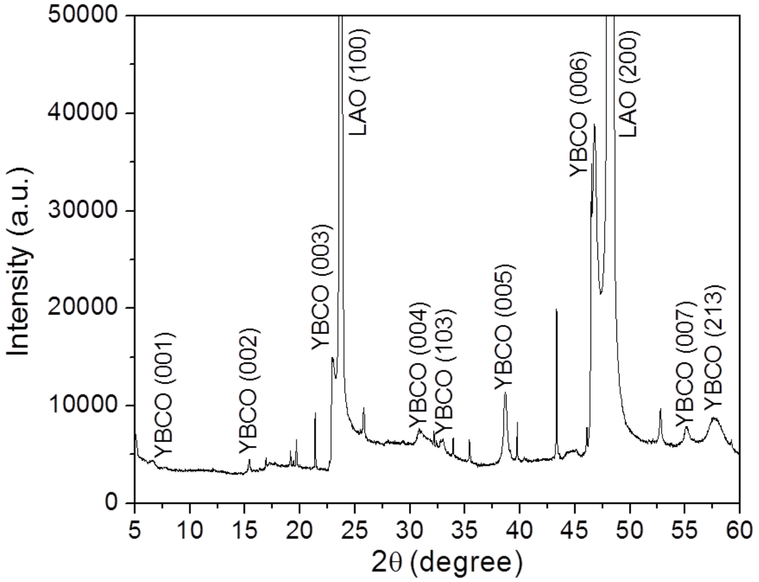

Fig 3.5 *X-ray pattern recorded on the barium nitrate process derived film sample converted at 760 ℃ in Ar atmosphere containing 100ppm oxygen.*

As shown in the XRD pattern (**Fig 3.5**), a good texture was obtained on the PAD process derived YBCO thin film, as all the (00*l*) YBCO peaks were clearly observed. However, randomly oriented grains as reflected from the (103) and (213) YBCO peaks were also found to coexist in the film, implying an inferior microstructure compared to the TFA-MOD derived

YBCO thin film. The SEM picture shown in **Fig 3.6** reveals a flate surface of the film. Plate-like particles are clearly seen anywhere, with some agglomerated big particles dispersed on some small regions on the surface. However, the SEM picture also shows a very limited thickness of the film, as the substrate is not totally covered, with some vacancies observed on the top. This is definitely due to the low metal concentration of the precursor solution, even with the help of PEG 200 in the aim of increasing the viscosity and enhancing the wetting properties of the solution. For this reason, multi-coating is necessary when applying the PAD process for producing YBCO thick films, thus the productivity can be seriously limited.

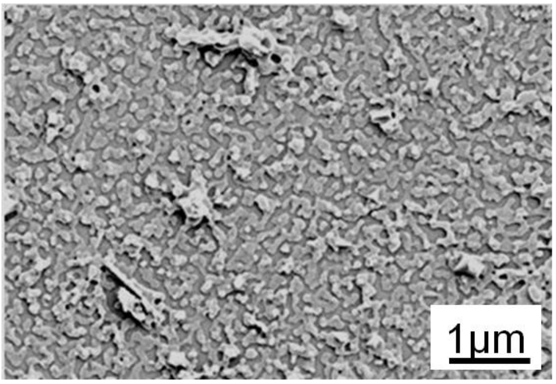

Fig 3.6 *SEM picture of the barium nitrate process derived film sample converted at 760 ℃ in Ar atmosphere containing 100ppm oxygen.*

3.5 Barium carbonate process

3.5.1 Review of barium carbonate process

Different from the barium hydroxide process and barium nitrate processes, where the metal cation suppliers are limited to specific metal inorganic salts, the diversity of the metallorganic compounds, chelating agents, and as well as solvents allows a wide selection of starting chemicals when making a recipe for a carbonate process for producing YBCO films. Generally, alkoxides [46-48] and metal organic salts [47, 48] are used as the metallorganic compounds in the barium carbonate processes. Surrounded by proper chelating ligands, the starting metallorganic compounds are homogeneously dispersed in the appropriate organic solvent.

Considering the homogeneity of the solution and compatibility between the solvent and the solute, the steric effect of chemicals is of great importance when selecting the organic anions of the metalorganic compounds and the corresponding solvent. In general, the principle obeyed when predicting the solubility of a specific metalorganic compound in a specific solvent is "like dissolves like", which means that the solute and the solvent should have similar molecular polarity. As described above, when using nitrates as the YBCO precursors, water is used for preparing a homogeneous solution because of the strong polarity of both water and the nitrates. In contrast, as alkoxides and acetates are often used in the carbonate processes, chelating agents are occasionally introduced when the compatibility between the solvent and the solute is unsatisfactory [46]. For example, TEA is used to improve the compatibility of acetates and water, since the hydrophilic functional groups provided by TEA molecules can make the polarity of metalorganic compounds similar to that of water. Besides, propionic acid and acetic acid are also promising solvents for dissolving acetates, however, ammonia and pyridine are normally necessarily used as chelating agents to enhance the polarity of the solvent.

Under the precondition of a suitable selection of the metalorganic compounds, chelating agents and solvent, a gelation step can take place, during which the precursor solution will form a homogeneous polymeric matrix [47-49]. In this step, the pH value of the solution dramatically affects the solubility and needs to be optimized by adjusting the ratio between the solvent and the chelating agent. In the publications by Harran university, a comparison was made on some commonly used metalorganic compounds (such as isopropoxide, 2-ethylhexanoate, methoxide, and pentanedionate) focusing on the optimum pH values for each solution [50-52]. Interestingly, the optimum pH values for the different precursor solutions were found in the same region, as they were all within the range between 5.5 and 6.5.

Throughout the development of the barium carbonate processes in producing YBCO superconducting thin films, it was unprecedented that KAIST in the Republic of Korea produced a 42cm-long YBCO conductor by using continuous reel-to-reel technology through the barium carbonate process [53]. The estimated critical current density of the product was $0.9MA/cm^2$. In 2005, AIST in Japan developed an acetylacetonate-based sol-gel process, by use of which high quality YBCO films were successfully deposited on a 30cm long LAO crystal. The J_c of the sample was as high as $2.6MA/cm^2$ [54] [55]. However, there was no further report about the application of that method for the YBCO deposition on buffered textured tapes. In spite of attempts done by many laboratories worldwide, the potential of the barium carbonate process to fabricate YBCO long tapes with good superconducting properties has still not been reached. The best J_c values obtained on the YBCO films deposited on RABiTs substrates nowadays still hardly exceed 1MA/cm^2 [53, 56], which are much lower compared to those shown in the publications describing the traditional TFA-MOD processes [7, 57].

3.5.2 Trial of barium carbonate process

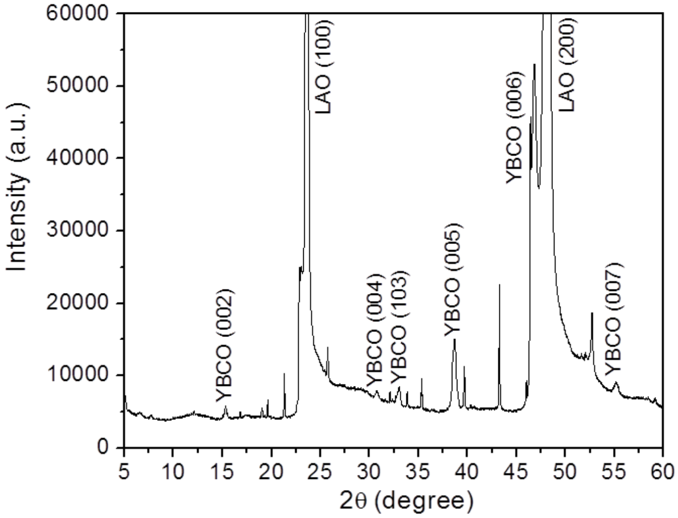

***Fig 3.7** X-ray pattern recorded on the barium carbonate process derived film sample converted at 760 ℃ in Ar atmosphere containing 100ppm oxygen.*

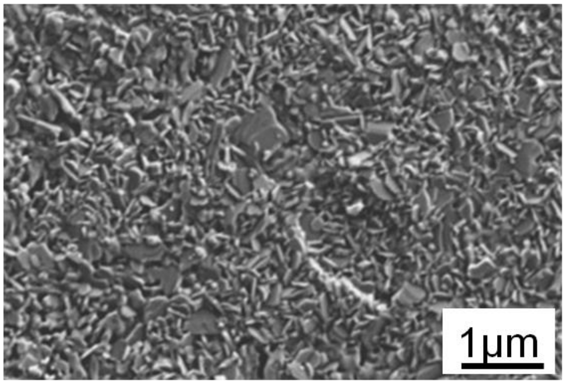

***Fig 3.8** SEM picture of the barium carbonate process derived film sample converted at 760 ℃ in Ar atmosphere containing 100ppm oxygen.*

To prepare the precursor solution, Barium acetate, Yttrium acetate and Copper acetate were mixed at the ratio of Y:Ba:Cu=1:2:3, dissolved in a mixture of propionic acid and ammonia at a volume ratio of 3:1. After one hour stirring at 80℃ on a heating plate, the solution became clear blue without any precipitation. Afterwards, all the extra solvent was removed in an evaporator. During this process, deionized water was added to help the removal of acid until a blue glassy gel was obtained. Finally, the gel was dissolved in methanol (Alfa Aesar), to yield a homogeneous solution with a total metal concentration (Y, Ba and Cu) of 1.5mol/L. The coating process and sintering process used in all organic process was the same as that used in the PAD process.

As can be seen from the XRD pattern (**Fig 3.7**), the intensity of the (00*l*) YBCO peaks is lower compared to traditional TFA-MOD produced films, the formation of randomly oriented YBCO grains is also reflected from the peak at 32.5 °. The SEM picture (**Fig 3.8**) also showed an inferior surface morphology compared to that of the TFA-MOD derived film. However, the microstructure was better compared to the films derived from the TMAP and the PAD processes from the point of view of both the absence of the a-axis orientated grains and better surface coverage, respectively.

3.6 Experiment on powder samples

Tab 3.1 *Starting reagents for the barium hydroxide, the barium nitrate and the barium carbonate based powder samples for in-situ XRD measurements.*

	Yttrium	Barium	Copper
Barium Hydroxide	Y_2O_3	$Ba(OH)_2$	CuO
Barium Nitrate	Y_2O_3	$BaNO_3$	CuO
Barium Carbonate	Y_2O_3	$BaCO_3$	CuO

To obtain deeper understanding on the mechanisms of YBCO formation through the different processes discussed in this chapter, in-situ XRD measurements were also done on the powder samples for each of the processes. Since the effect of the barium salts on the reaction mechanisms is being the object in this research, only the barium salts were changed depending on the process, whereas the yttrium salts and the copper salts were the same. The starting reagents for each powder sample are shown in **Tab 3.1**. During the in-situ measurements, $Ar/O_2$100ppm gas flow was used for each of the powder samples.

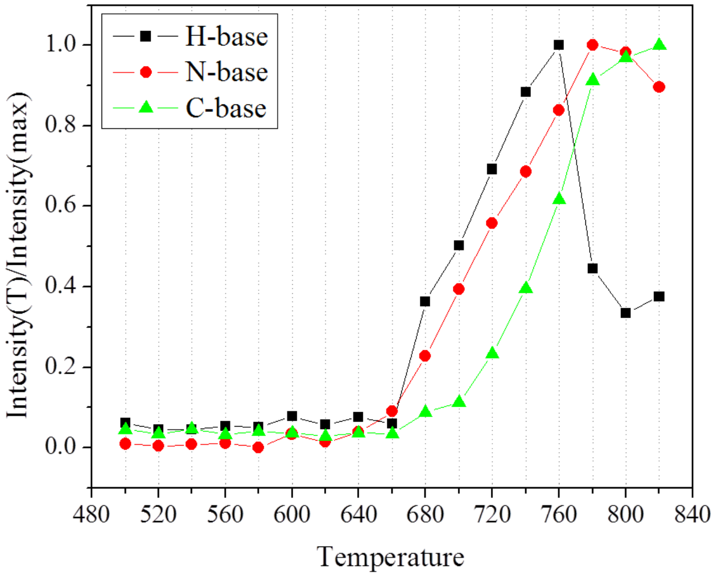

Fig 3.9 *Evolution of the intensity of YBCO X-ray diffraction lines during heating of the hydroxide-based (H-base), nitrate-based (N-base) and carbonate-based (C-base) powder samples.*

Fig 3.9 illustrates the YBCO formation progress rates for each powder sample as a function of temperature. It can be seen that for all samples, the YBCO phase formation started from 680℃. With further increasing the temperature, the reaction progressed much faster in the barium hydroxide based and the barium nitrate based samples compared to the barium carbonate based sample. The difference got even more conspicuous when the temperature reached 760℃, as the barium hydroxide based sample and barium nitrate based sample showed 100% and 80% phase formation, respectively, whereas the barium carbonate based sample only reached at a value lower than 60%. However, when the temperature was increased above 760℃, a dramatic decrease of YBCO phase content was clearly seen in the barium hydroxide based sample. This result is corresponding quite well to the XRD pattern (**Fig 3.3**) of the barium hydroxide process derived YBCO thin film, where the presence of Y211 phase was observed and assigned to the decomposition of YBCO. The facilitation of YBCO formation on the barium hydroxide based and barium nitrate based samples can be assigned to an increased reaction interface by changing the reaction from solid-solid state to solid-liquid state. This is due to the low melting points of $Ba(OH)_2$ and $BaNO_3$, which are 350℃ and 600℃, respectively. In contrast, $BaCO_3$ remains in the solid state up to 811℃. For this reason, in contrast to the case of $BaCO_3$, the hydroxide and nitrate based samples can go through solid-liquid state reactions as shown in equation (5) and (6), respectively.

$$\frac{1}{2}Y_2O_3 + 2Ba\,(OH)_2\,(L) + 3CuO \rightarrow YBa_2Cu_3O_{6+x} + 4H_2O \uparrow \qquad (5)$$

$$\frac{1}{2}Y_2O_3 + 2Ba\,NO_3\,(L) + 3CuO \rightarrow YBa_2Cu_3O_{6+x} + 2NO_2 \uparrow \qquad (6)$$

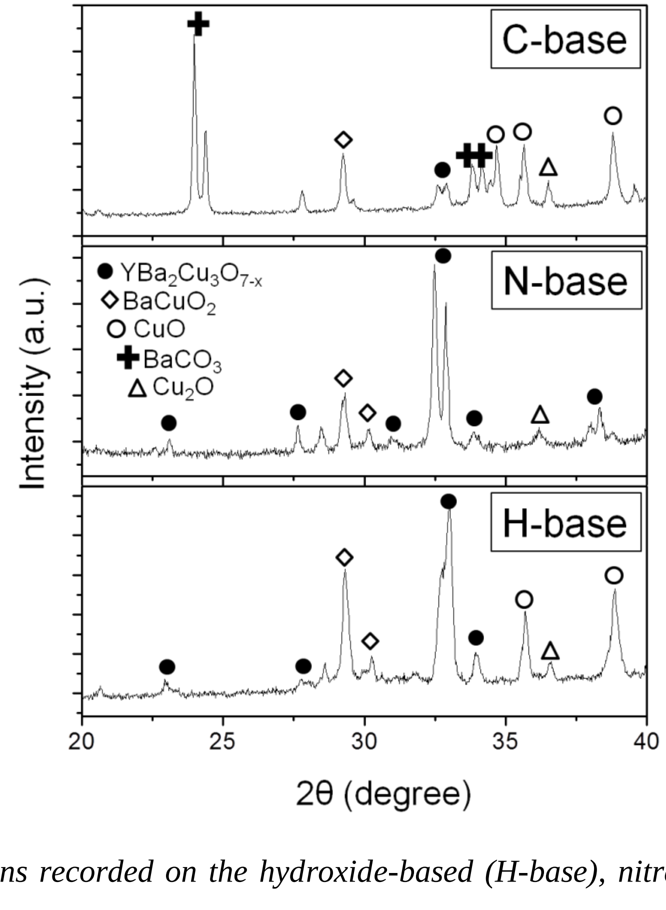

Fig 3.10 *XRD patterns recorded on the hydroxide-based (H-base), nitrate-based (N-base) and carbonate-based (C-base) powder samples sintered at 820 ℃ for 2 hours.*

The difference between the reaction progress rates of the different processes can be also reflected from the XRD results of the mixed solid powders quenched out after sintering at 760℃ for two hours. As shown in **Fig 3.10**, YBCO was the dominant phase in the hydroxide and nitrate samples, whereas in the carbonate sample, the intensity of the peaks corresponding to the reactants ($BaCO_3$ and CuO) were much higher than those of YBCO.

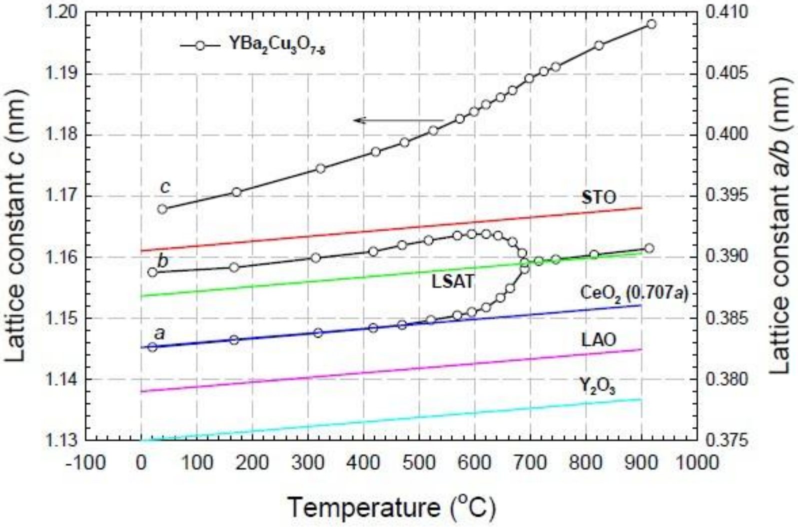

Fig 3.11 *Temperature dependence of cell parameters for YBCO and commonly used substrates [58].*

Fig 3.11 shows the temperature dependence of cell parameters for YBCO and commonly used substrates. It is obvious that the lattice constants of the substrates basically linearly increase with temperature. In contrast, the lattice constants of YBCO unit cell increase faster versus temperature. In the low temperature regime (T<700℃), the c value of the YBCO unit cell is roughly equal to that of 3(a+b)/2, which is close to the lattice constant of the substrates. In these conditions, heterogeneous nucleation takes place, where c-axis oriented grains form together with a-axis oriented grains. However, when the temperature further increases, the difference between the c value of the YBCO unit cell and the lattice constant of the substrates is broadened, thus a homogeneous nucleation takes place, where the formation of a-axis oriented grains is basically suppressed, due to the high mismatch induced strains that occur at the interface. The temperature dependence of the YBCO nucleation mechanism implies that though easy decomposition of the barium intermediate phase and the rapid formation of YBCO can be realized by using TMAP and PAD processes, the majority of YBCO formation takes place at low temperatures and is not benefitial to the epitaxial growth of YBCO thin films.

3.7 Conclusion

In the aim of improving the environmental safety and the productivity over those of the traditionally used TFA-MOD method, some fluorine-free CSD methods have been developed by many institutes. Depending on the barium products present after the decomposition of the precursors, the commonly used fluorine-free CSD processes were classified into barium hydroxide process (TMAP-MOD), barium nitrate process (PAD), and barium carbonate process. Due to the low melting and decomposition point of $Ba(OH)_2$ and $BaNO_3$, YBCO formation in the TMAP and PAD derived films was found to be considerably facilitated at low temperatures, resulting in heterogeneous nucleation of YBCO. On the other hand, the introduction of a H_2O partial pressure which could lead to the decomposition of YBCO and the inferior wetting performance of the precursor solution also appeared to be disadvantages for the TMAP and PAD methods, respectively. In contrast, in the fluorine-free processes where $BaCO_3$ forms as intermediate phase, the formation of YBCO was confirmed to be sluggish compared to the TMAP and PAD methods, however, the epitaxial growth of YBCO at high temperatures is beneficial for obtaining high-J_c values in the sintered films. In the following chapters, efforts to improve the superconducting performance of YBCO films derived from the barium carbonate processes will be described.

Reference

[1] Robert W. Schwartz. *Chem. Mater*, **9** (1997) 2325-2340.

[2] W. Cui, J. L. Tanner, T W Button. *Journal of Physics: Conference Series*, **97** (2008) 012257.

[3] K. Knoth, S. Engel, C. Apetrii, et al. *Current option in Solid State and Materials Science*, **10** (2006) 205-216.

[4] A. Sheth, K. Trembath. *Journal of Materials Processing Technology,* **123** (2002) 167-178.

[5] F. Parmigiani, G. Chiarello, N. Ripamonti, H. Goretzki, and U. Roll, *Physical Review B*, **36** (1987) 7148-7150.

[6] J. Gazquez, F. Sandiumenge, M.Coll, et al. *Chem. Mater*, **18** (2006) 6211-6219.

[7] M. Paranthaman, T. G. Chirayil, S. Sathyamurthy, D. B. Beach, A. Goyal, et al. *IEEE Transactions on Applied Superconductivity*, **1** (2001) 3146-3149.

[8] Y. Tokunaga, H. Fuji, R. Teranishi, et al. *Physica C*. **412-414** (2004) 910-915.

[9] P. C. McIntyre, M. J. Cima, J. A. Smith, R.B. Hallock, M.P. Siegal, and J.M. Phillips, *Journal of Applied Physics*, **71** (1992) 1868-1877.

[10] Y. R. Patta, D. E. Wesolowski, M. J. Cima. *Physica C*. **4** (2009)129-134.

[11] I. H. Mutlu, H. Acun, E. Celik, et al. *Physica C*. **451** (2007) 98-106.

[12] K. S. Mazdiyasni, C. T. Lynch, and J. S. Smith, *Inorg. Chem*. **5** (1966) 342-346.

[13] M. KAKIHANA, *Journal of Sol-Gel Science and Technology*, **6** (1996) 7-55.

[14] D. Marguillier, R. Cloots, A. Rulmont, et al. *Physica C*. **372-376** (2002) 715-718.

[15] T. Manabe, I. Yamaguchi, H. Obara, et al. *Physica C*. **378-381** (2002) 1017-1023.

[16] L. C. Pathak, S. K. Mishra, D. Bhattacharya, et al. *Materials Science and Engineering B*. **110** (2004) 119-131.

[17] Z. Aslanoglu, Y. Akin, M. I. El-Kawni, et al. *Physica C*. **384** (2003) 501-506.

[18] A. Gupta, R. Jagannathan, E. I. Cooper, E. A. Giess, J. I. Landman, and B.W. Hussey, *Applied Physics Letters*, **52** (1988) 2077-2079.

[19] P. C. McIntyre, M. J. Cima, M. F. Ng, R. C. Chiu, and W. E. Rhine, *Journal of Materials Research*, **5** (1990) 2771-2779.

[20] P. C. McIntyre, P.C., M.J. Cima, and M.F. Ng, *Journal of Applied Physics*, **68** (1990) 4183-4187.

[21] P. C. McIntyre, M.J. Cima, J.A. Smith, R.B. Hallock, M.P. Siegal, and J.M. Phillips, *Journal of Applied Physics*, **71** (1992) 1868-1877.

[22] J. A. Smith, M. J. Cima, and N. Sonnenberg, *IEEE Transactions on Applied Superconductivity*, **9** (1999) 1531-1534.

[23] A. Malozemoff, *Application of Coated Conductors International Workshop on Processing & Application of Superconductors, Gatlinburg Tennessee*, USA, 2002.

[24] D. L. Shi, Y. L. Xu, S. X. Wang, et al. *Physica C*. **371** (2002) 97-103.

[25] A. H. Li, M. Ionescu, H. k. Liu, et al. *Physica C*. **426-431** (2005) 1408-1414.

[26] L. Lei, G. Y. Zhao, J. J. Zhao, and H. Xu, *IEEE Transaction on Applied Superconductivity*, **20** (2010) 2286-2293.

[27] Y. Xu, A. Goyal, K. Leonard, et al. *Physica C*. **421** (2005) 67-72.

[28] X. X. Xu, W. C. Xu, Y. L. Bai, C. B. Cai and J. H. Fang, *Key Engineering Materials*, **537** (2013) 243-246.

[29] J. Lian, H. B. Yao, D. L. Shi, L. M. Wang, Y. L. Xu, Q. Liu and Z. Han, *Superconductor Science and Technology*, **16** (2006) 838-844.

[30] H. B. Yao, B. Zhao, K. Shi, Z. H. Han, Y. L. Xu, D. L. Shi, S. X. Wang, L. M. Wang, C. Peroz, C. Vilard, *Physica C*, **392-396** (2003) 941-945.

[31] D. L. Shi, Y. L. Xu, H. B. Yao, Z. Han, J. Lian, L. M. Wang, A. H. Li, H. K. Liu, S. X. Dou, *Superconductor Science and Technology*, **17** (2004) 1420-1425.

[32] Y. Xu, A. Goyal, J. Lian, N. A. Rutter, D. Shi, S. Sathyamurthy, M. Parathaman, L. Wang, P. M. Martin and D. M. Kroeger, *Journal of American Chemistry Society*, **87** (2004) 1669-1676.

[33] Y. L. Zhang, X. Yao, J. Lian, L. M. Wang, A. H. Li, H. K. Liu, H. B. Yao, Z. H. Han, L. F. Li, Y. L. Xu, D. L. Shi, *Physica C*, **436** (2006) 62-67.

[34] B. Zhao, H. B. Yao, K. Shi, Z. H. Han, Y. L. Xu and D. L. Shi, *Physica C*, **386** (2003) 348-352.

[35] W. T. Wang, X. F. Yang, M. H. Pu, H. Zhang, C. H. Cheng and Y. Zhao, *Journal of Superconductivity and Novel Magnetism*, **25** (2012) 39-44.

[36] F. Frangi, T. Higuchi, M. Deguchi, M. Deguchi and M. Murakmi, *Journal of Materials Research*, **10** (1995) 2241-2250.

[37] L. Dusoulier, R. Cloots, B. Vertruyen, J. Garcia-Fierro, R. Moreno, B. Ferrari, *Materials Chemistry and Physics*, **116** (2009) 368-375.

[38] C. Legros, C. Haut, L. Ponsonner-Mora, et al. *Jounal of the European Society*. **19** (1999) 165-173.

[39] L.Ciontea, V.Boffa, T.Petrisor, et al. *Physica C*. **257** (1996) 304-312.

[40] Q. X. Jia, T. M. Mccleskey, A. K. Burrell, et al. *Nature Mater*. **3** (2004) 529.

[41] Q. X. Jia, T. M. McCleskey, A. K. Burrell, et al, *United States Patent Application* 20050043184, 2005.

[42] C. Apetrii, H. Schlorb, M. Falter, et al. *IEEE Trans. Appl. Supercond*. **15** (2005) 2642.

[43] D.B. Braun, M.R. Rosen, *Rheology Modifiers Handbook-Practical Use and Application*, William Andrew Publishing, New York (2000) 193.

[44] C. E. Rice, R.B. Vandover, and G.J. Fisanick, *Applied Physics Letters*, **51** (1987) 1842-1844.

[45] P. Barboux, J. M. Tarascon, L. H. Greene, G. W. Hull, and B. G. Bagley, *Journal of Applied Physics*, **63** (1988) 2725-2729.

[46] A. A. Hussain and M. Sayer, *Journal of Applied Physics*, **70** (1991) 1580-1590.

[47] T. Kumagai, T. Manabe, W. Kondo, H. Minamiue and S. Mizuta, *Jpn. J. Appl. Phys*. **29** (1990) L940-L942.

[48] T. Manabe, M. Sohma, I. Yamaguchi, W. Kondo, K. Tsukada, S. Mizutaand T. Kumagai, *Supercond. Sci. Tech*, **17** (2004) 354-357.

[49] E.Celik, Y.Yamada, I.Hirabayashi, et al. *Materials Science and Engineering B* **110** (2004) 94.

[50] Ibrahim Halil Mutlu, Hediye Acun, Erdal Celik, et al. *Physica C*. **451** (2007) 98-106.

[51] G.Yi, M.Sayer, *Ceramic Bulletin*. **70** (1991) 1173.

[52] L.Arda, S.Ataoglu. *Jounal of Alloys and Componds* **471** (2009) 282-290.

[53] Jaimoo Yoo, Young-Kuk Kim, Kookchae Chung, et al. *IEEE Transaction on Applied Superconductivity*. **17** (2007) 3336-3339.

[54] T.Manabe, I.Yamaguchi, H.Obara, et al. *Physica C*. **378-381** (2002) 1017-1023.

[55] T.Manabe, M.Sohma, I.Yamaguchi, et al. *IEEE Transaction on Applied Superconductivity*. **15** (2005) 2923-2926.

[56] Z. Aslanoglu, Y. Akin, M. I. El-Kawni, L. Arda, W. Sigmund, and Y. S. Hascicek, *IEEE Transaction on Applied Superconductivity*. **13** (2003) 2755-2757.

[57] Y. Takahashi, T. Araki, K. Yamagiwaa, Yutaka Yamadaa, S.B. Kima, Y. Iiimab, K. Takedab, I. Hirabayashi, Physica C, **357-360** (2001) 1003-1006.

[58] M. Nevriva, E. Pollert, L. Matejkova, A. Triska, *Journal of Crystal Growth*, **91** (1988) 434-438.

Chapter 4

Influence of initial pH on the microstructure of $YBa_2Cu_3O_{7-x}$ superconducting thin films derived from DEA-aqueous sol-gel method

(Accepted by International Ceramics)

A fluorine-free aqueous sol-gel technique was used to fabricate YBCO superconducting thin films. Acetic acid was added in order to modify the complexation process taking place between the metal cations and the organic chelating agents. The electrical resistance and the pH value were used as indicators of the quality of the precursors. When pH=6.5, the precursor solution had the lowest resistance, implying a good ionization of the starting metal elements. By using the optimal precursor, the film was found to have very small size particles after pyrolysis. In consequence, the annealed YBCO films are characterized by a sharp superconducting transition, and their J_c (77k) reaches 0.25MA/cm^2.

4.1 Introduction

Chemical solution deposition (CSD) routes are promising for the industrialization of $YBa_2Cu_3O_{7-x}$ superconducting films, owing to the low cost of this technique, which doesn't require any high vacuum equipment [1]. Especially in the past decade, the trifluoroacetate metal-organic deposition (TFA-MOD) process has attracted much interest because it results in high critical current densities (J_c) and reproducibility of the product [2]. The TFA-MOD has however two intrinsic disadvantages, one being the released hazardous HF gas as a byproduct, while the other is the resulting time-consuming decomposition process, which has been an insurmountable obstacle to fast manufacturing scaling-up [3]. Therefore, it is of high interest to develop environmentally friendly and faster CSD methods. For this reason, some Non-fluorine techniques have been explored, such as the trimethylacetate-propionic acid (TMAP) process [4], the so-called advanced MOD process by using naphthenates [5], as well as sol-gel methods involving chelation between metal cations and citric acid (CA) [6] or ethylenediaminetetraacetic acid (EDTA) [7].

In this paper, an environmentally friendly water-based sol-gel method was used to synthesise YBCO superconducting films. Diethylamine (DEA) was introduced to the solution as the chelating agent, in order to prevent segregation and precipitation. As shown in table 1, compared to other standard chelating agents, one of the most important advantages of DEA is its low molecular weight, which can help suppressing the crack and porosity formation during pyrolysis [8].

However, according to previous publications on sol-gel techniques for producing YBCO films, the window of the optimal pH value of the precursor solution is quite narrow [9] [10]. On the other hand, publications relating to the production of other functional materials through some similar sol-gel processes confirmed that precursors with different pH values can lead to various kinds of bonding behaviors within the polymeric network, which in consequence may further influence the morphology of the sintered products as well [11] [12].

In the aim of obtaining high-quality YBCO superconducting films, we systematically investigated the effect of pH value of the YBCO sol-gel precursor on the chelation and polymerization mechanisms. The optimization of the annealing process is discussed as well.

Tab 4.1 *The molecular weight of some commonly used organic complexants.*
EDTA: ethylenediaminetetraacetic acid; TEA: triethanolamine; DEA: diethanolamine; TA: Tartaric acid; CA: citric acid.

Complexant	**EDTA**	**TEA**	**DEA**	**TA**	**CA**
Molecular Weight (g/mol)	292.24	149.88	105.14	150.09	192.14

4.2 Experimental details

4.2.1 Preparation of the samples

Precursor solution was prepared by mixing stoichiometric amounts of the metal acetates $Y(CH_3COO)_3 \cdot 4H_2O$ (Purity 99.9%, Alfa Aesar), $Ba(CH_3COO)_2$ (Purity 99%, Alfa Aesar), and $Cu(CH_3COO)_2 \cdot H_2O$ (Purity 98%, Alfa Aesar) at the ratio of Y: Ba: Cu= 1:2:3 and dissolving in deionized water. After one hour's constant stiring at 90℃, DEA (Purity 99%, Alfa Aesar) was added as chelating agent at the ratio of DEA: Metal= 1.7:1, yielding immediately a dark blue homogeneous solution. After 12 hours reaction at 60℃, extra water was removed by using a rotary evaporator, until the total metal cation concentration reached 1.5M/l. Finally, acetic acid (Purity 99%, Alfa Aesar) was added in order to obtain solutions of different pH values. For the investigation of the thin films, selected precursor solutions were dip-coated onto 5mm×10mm lanthanum aluminate $LaAlO_3$ (LAO) substrates at a withdrawing speed of 5mm/min. Prior to coating, all the substrates were cleaned with 35.5% hydrochloric acid and pretreated at 700℃ for five hours in pure oxygen. The coated films were dried in a furnace at 80℃ for two hours to evaporate most of the solvent. Thereafter, the pyrolysis process was performed up to 450℃ under pure oxygen flow during 60 minutes, in order to decompose the organic compounds present in the precursor. This coating-pyrolysis procedure was repeated to increase the film thickness. After cooling down to room temperature, the pyrolyzed films were heated from 20℃ to 770-810℃, and then held for one hour. A mixed gas atmosphere consisting of argon with 100ppm oxygen was flowing throughout the tube furnace during the whole annealing process. After crystallization, the samples were cooled to 450℃, and held for five hours under an atmosphere of pure oxygen, in order to obtain a perfect superconducting orthorhombic crystal structure. Finally, furnace cooling was done to room temperature.

4.2.2 Characterization of the samples

The pH value of the initial solutions was measured by using a pHmeter. The resistivity and the IR spectra of the gel samples were measured by a FLUKE (8020B) multimeter and a Bruker Tensor 27 spectrometer, respectively. The morphology of the pyrolyzed amorphous films and annealed crystallized films was observed by a DualScope atomic force microscope (AFM) and a supra 35 scanning electron microscope (SEM) from Zeiss, respectively. The microstructure of the samples was characterized by using a BrukerD8 advance x-ray diffractometer with CuKa radiation. AC suscepitibility measurements combined with hysteresis loops were carried out in a CRYOGENIC cryogen free measuring system (CFMS). The critical current density (J_c) of the samples was calculated by using the extended Bean critical state model [13], for which the key parameter t (thickness) was measured on a F20 ellipsometer produced by Filmetrics Company.

4.3 Results and discussion

In order to control the chelation-polymerization process, the pH value was carefully monitored. In the beginning, the basic idea is to suppress the hydrolysis of the metal ions by stimulating complexation with DEA ligands. In this situation, soluble chelate complexes are favored instead of the precipitation of aquo-hydroxo complexes [1]. The possible complex structure is shown in **Fig 4.1**.

Similarly to a previous publication where conductivity had been chosen as an index to characterize the quality of a precursor solution [14], we measured the resistance of solution samples that were stored in open dishes of the same size, as a function of time, while water is slowly evaporating. **Fig 5.2** shows the gel samples with initial pH values of 6.5 and 8.3 after ten hours evaporation. The different colors imply different chelating and polymerization processes that happened during evaporation.

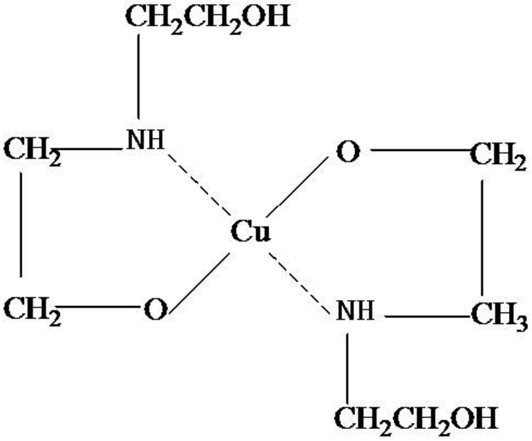

Fig 4.1 *Possible conformation of Cu metal ion with DEA ligands.*

As shown in **Fig 4.3**, the resistance increases gradually with time. Meanwhile, the total metal concentration was progressively increasing, resulting in a rising contribution to the precursor conductivity. As a result, the resistance of the samples with different pH values was increasingly differentiated. This is because diverse crystallization or complexation phenomena occurred in the different samples. During the process, several reactions may take place in the solution, as expressed in the reaction equations (A) (B) (C), where M is the metal ion, A is the complexant, AC stands for acetic acid, n and m are the coordination numbers of M and A respectively, z and m are the valences of M and A respectively [1]. There is a competition between reactions (A) and (B) when a complexant is present in the solution.

$$\text{Hydrolysis: } [M(H_2O)_n]^{z+} + hH_2O \rightarrow [M(OH)_h(H_2O)_{n-h}]^{(z-h)+} + hH_3O^+ \quad (A)$$

$$\text{Complexation: } [M(H_2O)_n]^{z+} + aA^{m-} \rightarrow [M(H_2O)_w(A)_a]^{(z-am)+} + (n-w)H_2O \quad (B)$$

$$\text{Ionization: } [M(H_2O)_n]\,(AC)_z \rightarrow [M(H_2O)_n]^{z+} + zAC^- \quad (C)$$

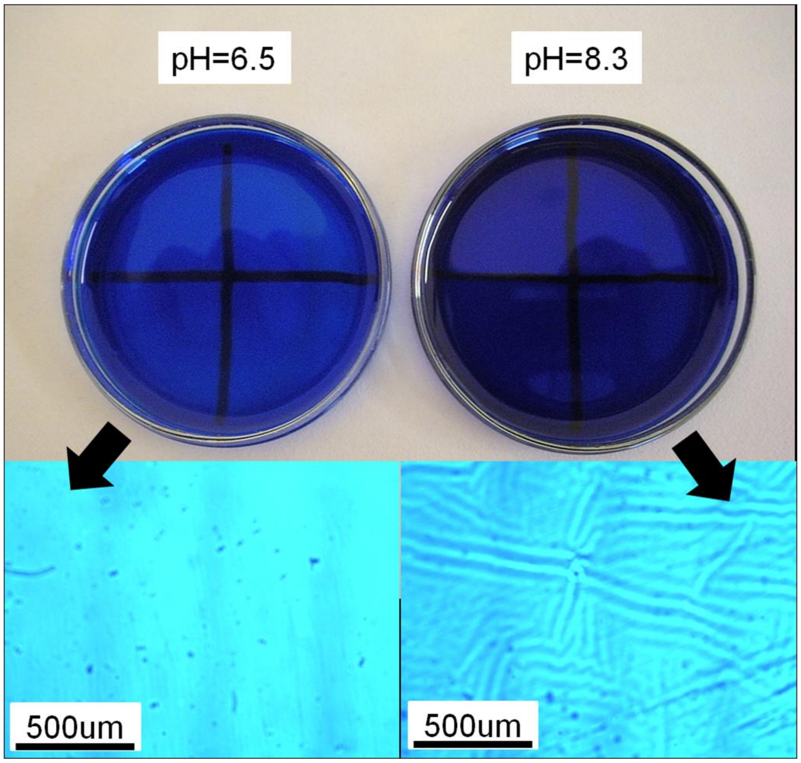

Fig 4.2 *Picture and OPT micrograph of the gel samples with pH=6.5 and pH=8.3.*

In the regime of high pH value, although without any precipitation, the samples were heterogeneous and of high resistance. This is due to the formation of hydroxide $[M(OH)_z]$. Previous publications proposed that the unionized hydrolyzates resulted from the uncontrolled hydrolysis, where the reaction as shown in equation (A) was rapidly carried out without any interruption, till all the complexed H_2O are substituted by OH^- [1] [9]. With the addition of acetic acid, the pH value of the samples was approaching to 6, and a minimum appears on the resistance versus pH plot around 6.5, revealing a better ionization of the metal components. This results from the complexation between the metal ions and DEA ligands, according to equation (B). In this process, two pentadentates were established of one metal ion and two DEA moleculars [15], hence the metal ions are well enveloped and prevented from the attack of free OH^-. Also, some other reports claimed that higher acidity of the precursor can help preventing hydrolysis of the organic metal salts to hydrolysis [16], even without participation of a complexant. After long-time exposure, samples of pH value in the range around 6.5 can transit from wet rubber to brittle polymer glass, without any loss of homogeneity. However, as the pH value decreases with the addition of acetic acid, the resistance climbed again (Fig.3), while some white regular shaped crystals were separated out from the solution. This phenomenon can be assigned to the re-crystallization of acetates [1] [9]. With the addition of acetic acid, the concentration of AC^- is increased. In consequence the balance of equation (C) is shifted back to the left side and thus the ionization of $[M(H_2O)_n]\ (AC)_z$ is undermined.

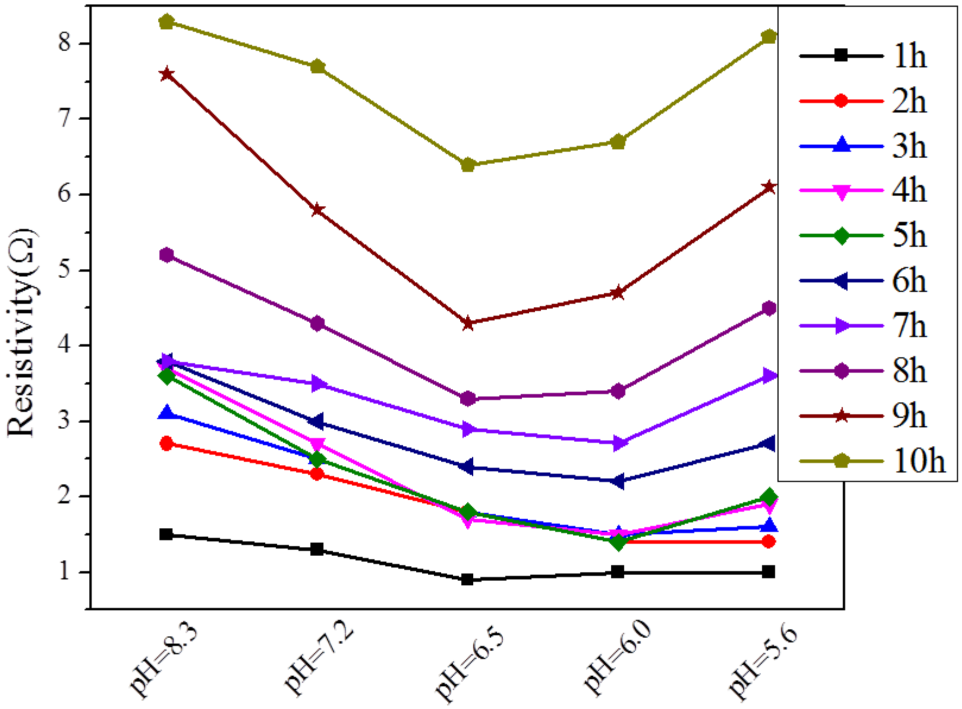

Fig 4.3 Resistance evolution of the samples with different pH values as a function of evaporation time.

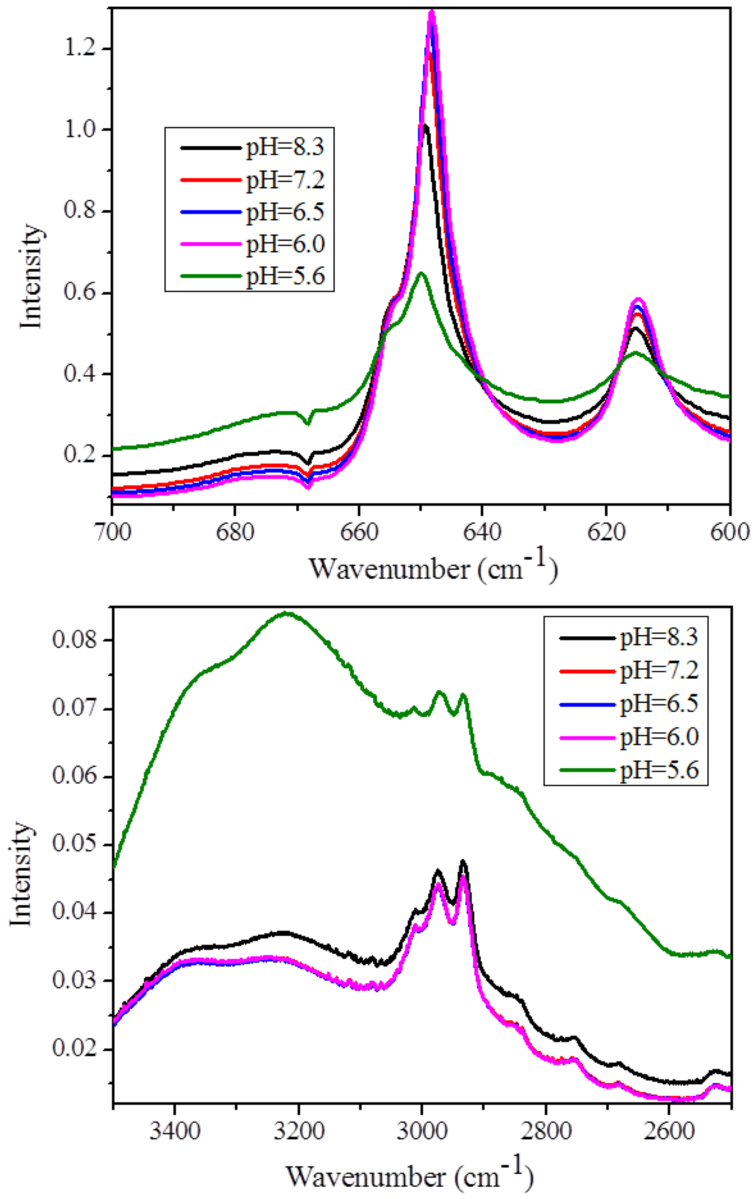

Fig 4.4 *FTIR spectra of the gels derived from sol samples with different pH values. Samples of pH=6.0, 6.5 and 7.2 show quite similar spectras in high wavenumber regime, thus the plots of them are overlapped.*

The complexation extent of the metal ions can be followed by the FTIR spectra, as shown in figure 4. According to previous publications [17] [18], vibrations in the wavenumber range from 800 to 400cm^{-1} are due to Metal-O bonds. However, it is impossible to assign them here to individual Metal-O bond, because of the complexity of the precursor which contains three different metal cations. The broad peak at wavenumbers around 3000-3500cm^{-1} is assigned to the vibration of O-H bonds in the sample, and the three peaks at 3016, 2925 and 2971cm^{-1} are assigned to the C-H stretching vibrations of DEA. As most water had evaporated out from the gel, the O-H bonds originate primarily from the two -CH_2CH_2OH branches of DEA. The spectra of the samples with pH values in the vicinity of 6.5 almost coincide and have the lowest and the highest intensity levels in the ranges of 3000-3500cm^{-1} and 600-700cm^{-1}, respectively, implying the tendency of Metal-O bonds formation and the consumption of O-H bonds. However, the samples with the highest (8.3) or the lowest (5.6) pH values, showed a totally inverse behavior. Especially for the sample of pH=5.6, the O-H peak remains high, with quite little generation of Metal-O bonds. These observations correspond quite well to the expectation of $[M(H_2O)_n]$ $(AC)_z$ crystallization, when no complexation with DEA occurs with the metal-organic salts.

Fig 5.5 shows the morphology of pyrolyzed films derived from the precursors with pH=6.5 and pH=8.3 values respectively. The low-pH sample exhibits small particle size and distinct grain boundaries. In contrast, the high-pH sample shows a surface composed of much coarser particles, resulting in a high roughness of 22.8nm, which is almost two times that of the low-pH sample (14.8nm). The morphology difference might originate from the different gelations processes that occur in the samples of different pH values [19] [20].

In the low pH regime, the network formation is governed by the hydronium ion (H_3O^+), where hydration rate is higher than polymerization rate， thus olation takes place, as shown in **Fig 5.6**. In this case straight linear chains are believed to form, which in consequence can induce formation of small size particles after decomposition. Furthermore, under this mechanism the film coating and drying procedure can also benefit from the greater flexibility of the solution and large interstices of the gel respectively. This can be seen from the optical microscope as in figure 2, where the gel sample of pH=6.5 shows a quite smooth surface, implies the release of stress due to its higher flexibility. On the contrary, on the sample of pH=8.3, massive wrinkles are seen on the surface. Similar surface was also observed on TFA-MOD derived samples by J. T. Dawley and was described as “pencil-maze structure”, which was believed to be harmful to thick film development via multilayering [21]. This is because in the high pH regime, for the high concentration of hydroxyl (OH), the polymerization process was conducted vigorously, leading to entanglement among branched chains, which is the so-called oxolation. This will on the other hand lead to particle size enlargement, which is harmful to further solid state reaction during the sintering process. As in the annealing process, a typical solid reaction of the components $BaCO_3$, CuO and Y_2O_3 takes place. Theoretically, homogeneously distributed fine particles can enlarge the surface area [12] and shorten the diffusion paths [1]. This is advantageous for the formation of the YBCO superconducting phase at high temperature.

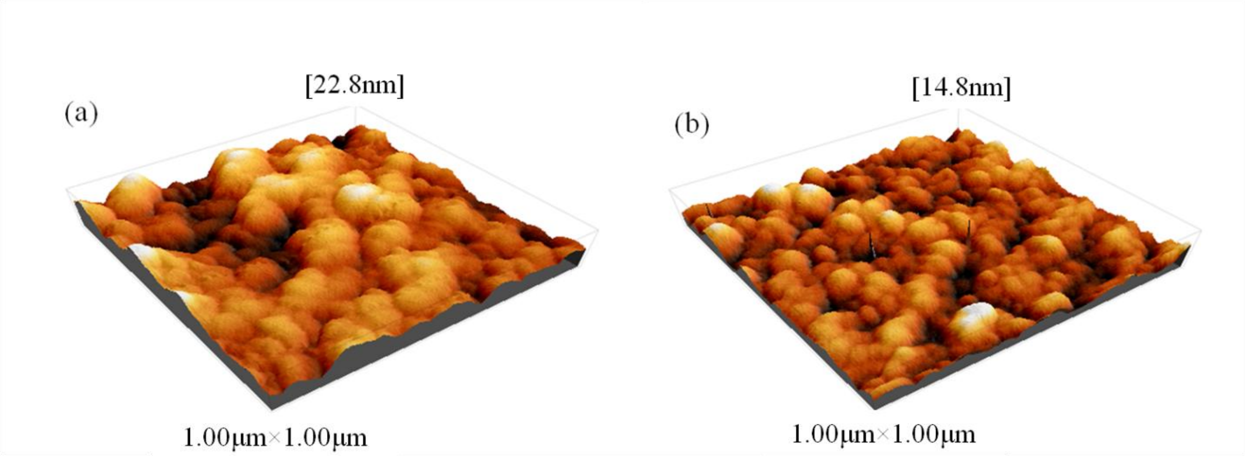

Fig 4.5 *AFM micrograph of the pyroplyzed films derived from the precursor of (a) pH=8.3 and (b) pH=6.5.*

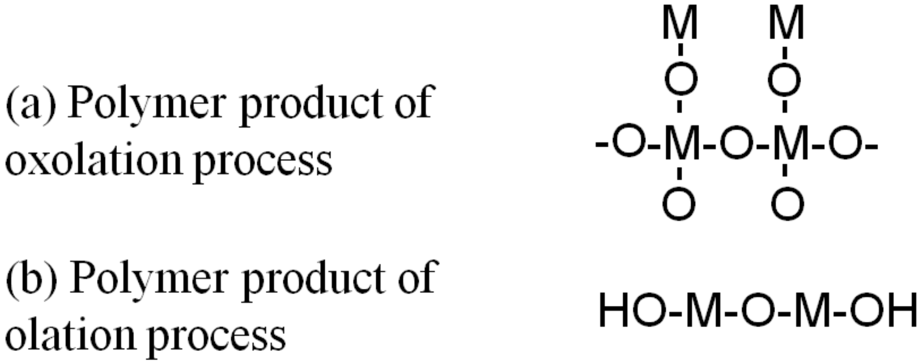

Fig 4.6 *Polymer products of (a) oxolation and (b) olation processes, where M is metal ion.*

As high critical current density can only be achieved on epitaxially grown YBCO thin films, the samples were characterised by XRD measurements (**Fig 4.7**). In sample 1, derived from the precursor with pH=8.3, though no peaks of secondary phases were detected, the intensity of YBCO (00*l*) peaks were quite low, implying only a rather low amount of YBCO. From the SEM picture (**Fig 4.8a**), it can be seen that the morphology of sample 1 is coarse and discontinuous. Some needle-like particles, probably a-axis oriented YBCO grains, were found agglomerating on some parts of the surface. Though too small to be noticed on the XRD pattern, these randomly oriented grains can cause weak links, which dramatically undermine the superconducting performance. By using the optimal solution (pH=6.5) as precursor, samples showed much better (00*l*) preferred growth orientation, except that annealed at the lower annealing temperature of 770℃. The sample annealed at 790℃ exhibits the most intense YBCO (005) peak. Further increasing the annealing temperature to 810℃ results in a poorer texture. This is also reflected in the SEM pictures. From figure 8c, it is seen that sample 3 has a continuous and dense surface, totally covered by flaky particles, indicating a preferential c-axis orientation.. In contrast, samples annealed at lower (sample 2) or higher (sample 4) temperatures showed porous and melted-like surface respectively, both of which are not promising for good superconducting performance.

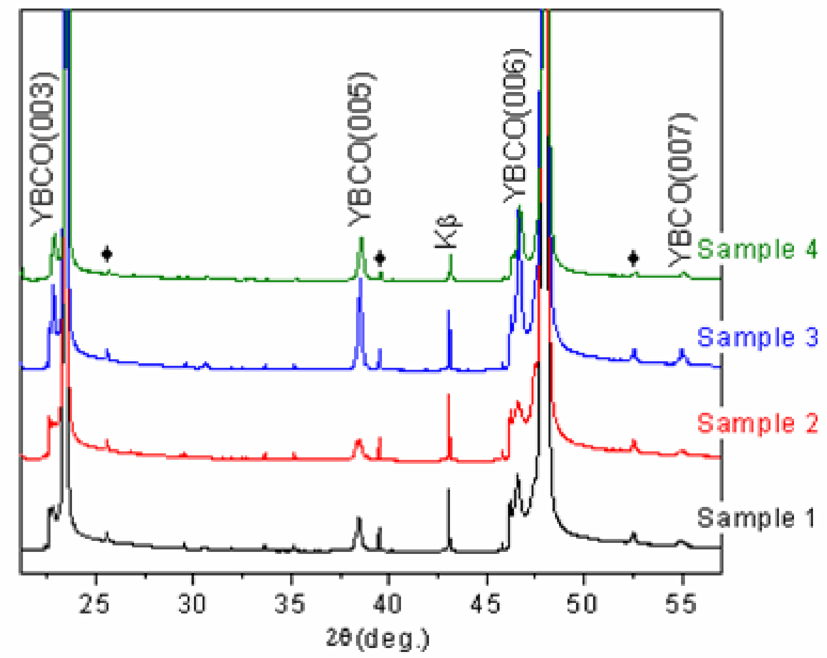

Fig 4.7 *XRD pattern of YBCO thin films. Sample 1: Precursor of pH=8.3, annealed at 790℃ for 1 hour; Sample 2: Precursor of pH=6.5, annealed at 770℃ for 1 hour; Sample 3: Precursor of pH=6.5, annealed at 790℃ for 1 hour; Precursor of pH=6.5, annealed at 810℃ for 1 hour. Peaks marked by ♦ are from background.*

Good out-of-plane and in-plane orientations of samples 3 are reflected by phi-scan and omega scan, as shown in **Fig 4.9**, where the FWHM values are 0.4 ° and 1.6 °, respectively. These results confirm that sample 3 has superior microstructure compared to the others.

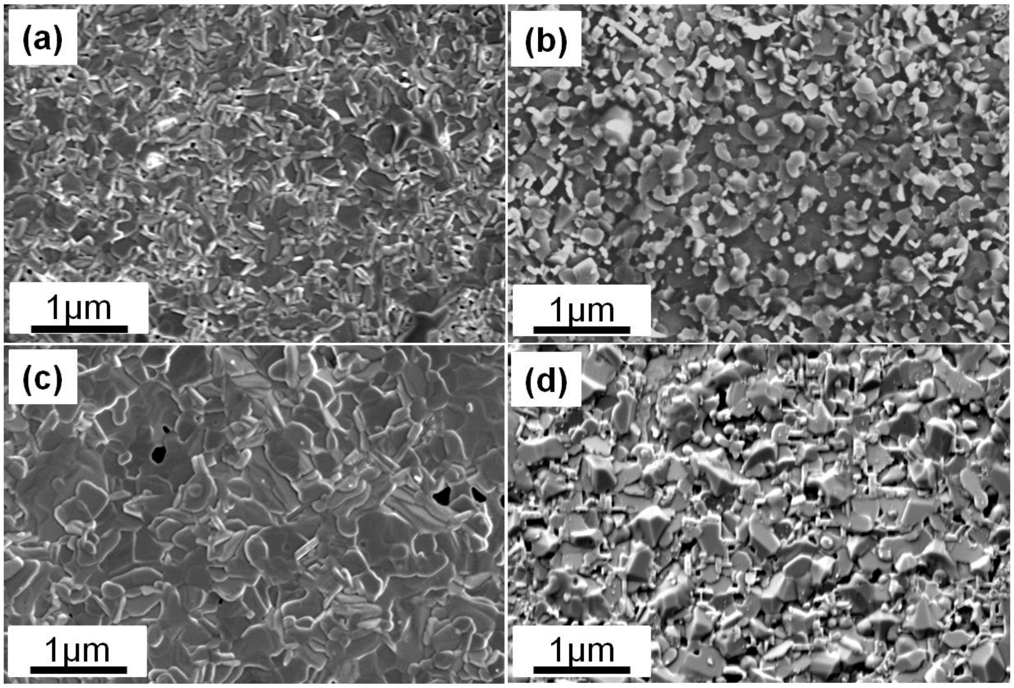

Fig 4.8 *Surface morphology (SEM) of YBCO thin films. Sample 1: Precursor with pH=8.3, annealed at 790 ℃ for 1 hour; Sample 2: Precursor with pH=6.5, annealed at 770 ℃ for 1 hour; Sample 3: Precursor with pH=6.5, annealed at 790 ℃ for 1 hour; Precursor with pH=6.5, annealed at 810 ℃ for 1 hour.*

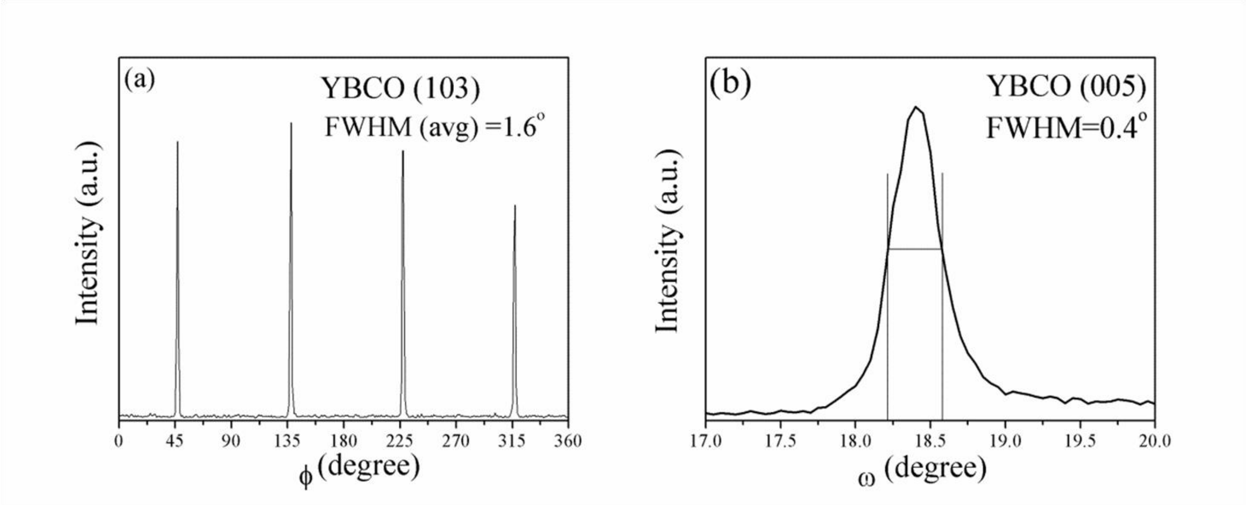

Fig 4.9 *(a) (103) phi-scan of the sample 3; (b) (005) omega-scan of sample 3.*

AC susceptibility of the annealed YBCO samples was measured to characterize their superconducting behaviour. The real component of the AC susceptibility of two samples between 30K and 110K are shown in figure 10. Obviously sample 3 displays a very sharp superconducting transition, which starts from 87.6K, with a temperature width of less than 5K. In contrast, sample 1 shows a sluggish transition, which is not even finished until 30K. Estimating the thickness to 150nm, by using the extended Bean critical state model, the critical current density (J_c) of sample 3 is approximately 0.25MA/cm^2 at 77K under self field, while the J_c of sample 1 is so low that it can be neglected. This result is well consistent with the anticipation based on the microstructural investigation.

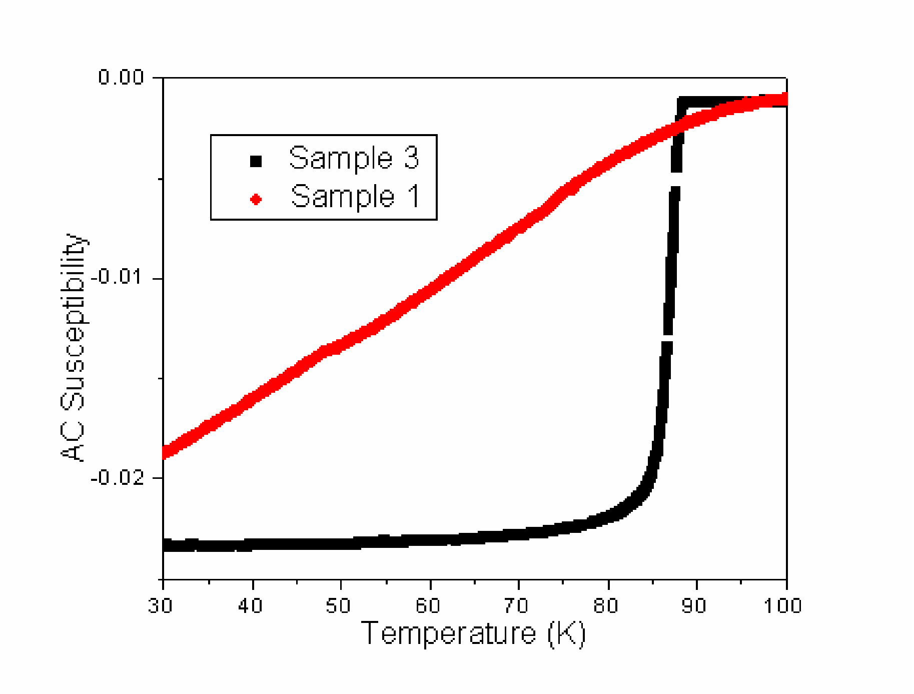

Fig 4.10 *Superconducting transition of sample1: Precursor of pH=8.3, annealed at 790℃ for 1 hour; and Sample 3: Precursor of pH=6.5, annealed at 790℃ for 1 hour.*

4.4 Conclusion

In this report, an aqueous non-fluorine sol-gel method was successfully used to deposit YBCO superconducting thin films on LAO single crystals. DEA was used as a complexant to protect the metal ions from severe hydrolysis. Resistances were used as the indicator to the quality of precursor solutions with different pH values. The effect of pH value of precursor solution to the reaction behavior and final microstructure and superconducting performance is briefly summarized in Table 2. By optimizing the pH value of the starting solution, a homogeneous and well polymerized precursor was fabricated. After pyrolysis, fine particles were seen on the amorphous films. After the annealing process, a J_c of 0.25MA/cm^2 was obtained.

Tab 4.2 *Brief summary of the influence of initial pH value on YBCO products at different processing steps.*

	Chelation	**Polymerization**	**Pyrolysis**	**Annealing**	**Superconducting performance**
pH=5.6	Precipitation of acetates (High resistance)	×	×	×	×
6.0<pH<7.2	Homogeneous solution (Low resistance)	Olation (straite chain)	small particles	Good microstructure	J_c=0.1-0.2MA/cm^2
pH=7.2	Homogeneous solution (High resistance)	Oxolation (entanglement)	large particles	Bad microstructure	×

Reference

[1] M. Kakihana, (1996) *J Sol-Gel Sci Technol,* **6** (1996) 7-55.

[2] K. Zalamova, A. Pomar, A. Palau, T. Puig, and X. Obradors, *Supercond Sci Technol,* **23** (2010) 014012.

[3] B. A. Glowacki, M. Mosiadz, *J Sol-Gel Sci Technol*, **51** (2009) 335-347.

[4] D. L. Shi, Y. L. Xu, H. B. Yao, Z. Han, J. Lian, L. M. Wang, A. H. Li, H. K. Liu, S. X. Dou, *Supercond Sci Technol*, **17** (2004) 1420-1425.

[5] K. Yamagiwa, T. Arakia, Y. Takahashia, H. Hieib, S. B. Kima, K. Matsumoto, J. Shibatad, T. Hirayamad, H. Ikutae, U. Mizutanib, I. Hirabayashi, *J Cryst Growth*, **229** (2001) 353-357.

[6] W. Cui, P. Mikheenko, L. M. Yu, T. W. Button, J. S. Abell, A. Crisan, *J Supercond Nov Magn*, 22 (2009) 811-815.

[7] T. Brylewski, K. Przybylski, *Appl Supercond*, **1** (1993) 737-744.

[8] W. T. Wang, G. Li, M. H. Pu, R. P. Sun, H. M. Zhou, Y. Zhang, H. Zhang, Y. Yang, C. H. Cheng, *Physica C,* **468** (2008) 1563-1566.

[9] T. T. Tuy, S. Hoste, G. G. Herman, K. De Buysser, P. Lommens, J. Feys, D. Vandeput, I. Van Driessche, *J Sol-Gel Sci Technol*, **52** (2009) 124-133.

[10] G. V. Rama Rao, D. S. Suryanarayana, U. V. Varadaraju, T. Geetha Kumari, S. Venkadesan, *Mater Chem Phys*, **39** (1994) 149-156.

[11] P. K. Sharma, V. V. Varadan, *J Eur Ceram Soc*, **23** (2003) 659-666.

[12] P. K. Shama, M. H. Jilavi, V. K. Varadan, H. Schmidt, *J Phys Chem Solids*, **63** (2002) 171-177.

[13] E. M. Gyorgy, R. B. van Dover, K. A. Jackson, *Appl Phys Lett*, **55** (1989) 283-285.

[14] J. Yang, W. J. Weng, Z. S. Ding*, J Sol-Gel Sci Technol,* **4** (1995) 187-193.

[15] S. Grigoryan, A. Manukyan, A. Hayrapetyan, A. Arzumanyan, A. Kuzanyan, Y. Kafadaryan, E. Vardanyan, *Supercond Sci Technol* **16** (2003) 1202-1206.

[16] E. R. Savinova, A. L. Chuvilin, V. N. Parmon, *J Mol Catal*, **48** (1988) 217-229.

[17] M. Motta, C. V. Deimling, M. J. Saeki, P. N. Lisboa-Filho, *J Sol-Gel Sci Technol*. **46** (2008) 201-207.

[18] A. Baranauskas, D. Jasaitis, A. Kareiva, *Vib Spectrosc*, **28** (2002) 263-275.

[19] E. J. A. Pope, J. D. Mackenzie, *J Non-Cryst Solids,* **87** (1986) 185-198.

[20] Y. W. Chen, T. M. Yen, C. P. Li, *J Non-Cryst Solids,* **185** (1995) 49-55.

[21] J. T. Dawley, P. G. Clem, M. P. Siegal, D. R. Tallant and D. L. Overmyer*, J Mater Res,* **17** (2002) 1900-1903.

Chapter 5

Characterization of microstructure and performance of $YBa_2Cu_3O_{7-x}$ films synthesized through sol-gel aqueous precursors with DEA/TEA addition

(*Journal of Superconductivity and Novel Magnetism, 26 (2013) 1883–1886****)***

$YBa_2Cu_3O_{7-x}$ (YBCO) superconducting thin films are synthesized through non-fluorine sol-gel aqueous processes. Diethanolamine (DEA) and triethonalamine (TEA), which have similar molecular structures but different complexation abilities and molecular weights, are separately used as chelating agents. Compare to DEA, the precursor with TEA additive exhibits higher stability and yields films of superior microstructure and surface mophorlogy. Finally, the YBCO film produced from the TEA precursor displays a sharp superconducting transition, with a J_c of 1.7MA/cm^2 estimated at 77K in self field.

5.1 Introduction

In the field of YBCO thin film production, Chemical Solution Deposition (CSD) has attracted much attention, given its advantages such as being a low-cost non-vacuum technology, with easy control of chemical stoichiometry, and high potential for industrialization [1]. However, the industrialization of the most mature CSD process, trifluoroacetate metal organic deposition (TFA-MOD) process [2], is obstructed by the hazardous HF gas release. In this report, an environmentally friendly aqueous sol-gel method was applied to synthesis YBCO thin films. Diethanolamine (DEA) and triethonalamine (TEA), which have similar molecular structures but different complexation abilities and molecular weights, are separately used as chelating agents and their influence on the microstructure and superconducting performance of YBCO thin films was investigated.

5.2 Experimental Details

The precursors were prepared by dissolving metal salts of $Y(CH_3COOH)_3 \cdot 4H_2O$, $Ba(CH_3COOH)_2$, and $Cu(CH_3COOH)_2 \cdot H_2O$ at the ratio of 1:2:3 in deionized water. After stiring at 90℃ for 1 hour, TEA or DEA was added as chelating agent into the solution at the ratio of DEA/TEA: Metal= 1.7:1. The chelating process was conducted by placing the solution on a heating plate at 60℃ for more than 12 hours, until the cation (Y+Ba+Cu) concentration reaches 1.5mol/L.

The precursor was coated on the $LaAlO_3$ single crystals (Size: 10mm×5mm) by means of dip-coating with a withdrawing speed of 10mm/min. After drying at 90℃ for more than one hour, all the coated precursor samples were pyrolyzed at 450℃ in humid oxygen atmosphere with a heating rate of 10℃/min. In the annealing process, samples were sintered at 789℃ for one hour under argon atmosphere with an oxygen partial pressure of 100ppm. Post oxygenation was conducted for five hours after furnace cooling to 450℃.

Viscosity was measured in an AR2000 viscometer from TA instruments. The morphology of the pyrolyzed films was observed by using DualScope Microscope (DS 9550). A Bruker D8 x-ray diffractometer with Cu Kα radiation was used to characterize the phase content and texture of the annealed samples. The surface morphology of the samples was investigated in a Supra 35 (SEM) electron microscope in secondary electron mode. The measurement of the superconducting performance was carried out in a CRYOGENIC cryogen free measuring system (CFMS). The determination of the critical current density (J_c) is based on the magnetisation loops and was calculated using the Bean model [3].

5.3 Results and discussion

5.3.1 Characterization of the solutions and wet films

Fig 5.1 shows possible coordination between the alkanolamines and metal cation. Each metal cation can form coordinating bonds with two nitrogen atoms and two oxygen atoms that are respectively situated at the center and the branch endings of the alkanolamine molecules. Surrounded by the two complexing molecules, the metal cations are protected from the external attacks of free OH^- ions. In this way, precipitates like $M(OH)_x$ are well prevented [4]. Compared to DEA, each TEA molecule has one more hydroxyl functional group, which in theory can make the chelation process much easier and enhance the cation solubility in water.

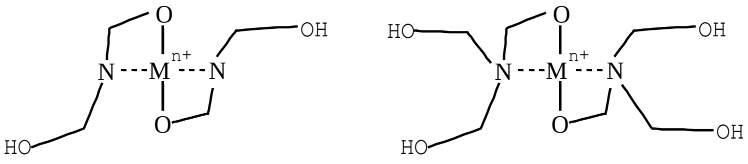

(a) DEA **(b)** TEA

***Fig 5.1** The molecular structure of $[M (DEA)_2]^{n+}$ and $[M(TEA)_2]^{n+}$ complexes.*

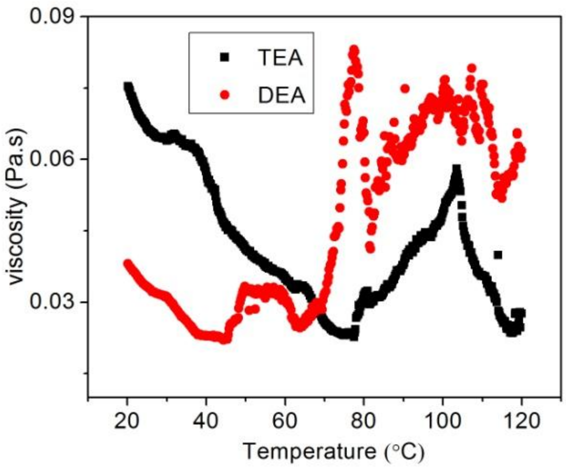

***Fig 5.2** Viscosity evolution of the TEA and DEA precursors versus temperature.*

The chelating process of the DEA and TEA precursors can be studied by high-temperature viscosity measurements (**Fig 5.2**). In the low temperature region, the viscosity of the TEA sample decreases with increasing temperature, which is a common feature of liquids. After that, a gradual rise of viscosity is seen when the temperature reaches 75.5℃. This phenomenon is linked to the oligomerization that takes place between the chelated metal-organic complexes. As the monomers connecting to each other, the molecular mobility decreases, leading to an obvious change in the viscosity of the solution. When the temperature is higher than 100℃, the viscosity drops again, as the organic system collapses with a very fast removal of water. In contrast, in the case of the DEA-added sample, the viscosity decreases with temperature only at the very beginning, as the first increase was seen before 50℃. The oligomerization happens earlier and much faster compared to the TEA-chelated sample, as evidenced from the dramatical increase of viscosity between 60℃ and 80℃. However, the established system is remarkably fragile, as when temperature exceeds 80℃, the viscosity starts to fluctuate severely. Based on the results of viscosity evolution measurement, different H_2O escaping paths from the DEA and TEA precursor films are proposed and schematized in **Fig 5.3**. Due to the low stability of the organic network in the DEA precursor, which is reflected in **Fig 5.2**, the long-chain polymers formed by oligomerisation tend to be broken into shorter chains during the long-time drying process. In this case, water can escape from nearly everywhere on the film surface. This hypothesis can be demonstrated in **Fig 5.4**, where hollow ring like plates are densely dispersed on the wet films quenched after 30min treatment at 120℃. The hole in the middle of each round plate results from the evaporation of water through the film surface. In contrast, as the polymer network in the TEA precursor system is more stable (**Fig 5.2**), it keeps a higher stiffness during the drying process. Water molecules thus need to diffuse over long length to seek breakpoints of the relatively long-chain oligomers, from where they accumulate and escape from the film. The differences in polymer network stability and the consequence for water evaporation lead to a quite different morphology of the two dried films, where the same hollow ring like plates are observed but are sparsely dispersed on the surface and have larger size in the TEA-based film (**Fig 5.4**).

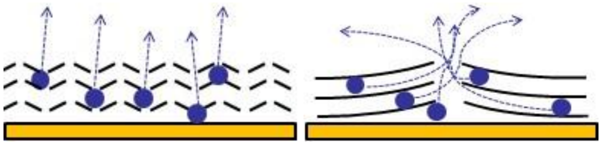

Fig 5.3 *The schematic diagram of H_2O escaping paths from the DEA (a) and TEA (b) precursor films.*

5.3.2 Microstructure and superconducting performance

The XRD patterns of TEA and DEA precursor derived YBCO films are shown in **Fig 4.5**. Both films were annealed at 789℃ for 1hour, under an atmosphere of Argon with 100ppm oxygen. Though a non-fluorine precursor was used in present case, no $BaCO_3$ phase is detected in the patterns. In the TEA sample, all (*00l*) peaks from (*001*) to (*007*) are well detected and have high intensities, implying a good c-axis oriented grain growth. In contrast, in the DEA sample, except for the two peaks corresponding to (*005*) and (*007*) reflections, most of other (*00l*) peaks are too weak to be observed. This indicates that the growth of the YBCO grains is severely suppressed during the annealing period in this film.

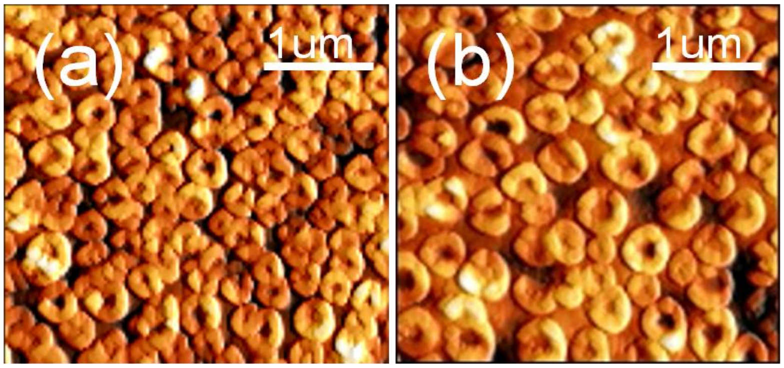

Fig 5.4 *AFM micrographs of DEA (a) and TEA (b) precursor films dried at 120℃ for 0.5 hour.*

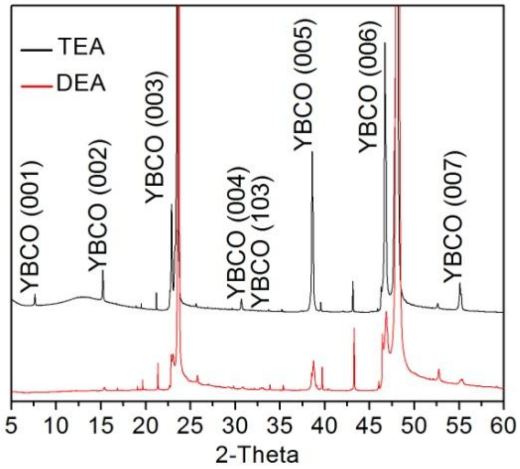

Fig 5.5 *XRD patterns of the films that annealed at 789℃ for 1hour, under the atmosphere of Argon with 100ppm oxygen.*

Fig 5.6 (a) and (b) shows the SEM images of the TEA and DEA precursor derived YBCO films. The surface of the TEA sample is totally continuous and crack-free, with plate-like particles homogeneously covering the surface. In contrast, the DEA sample represents a coarse and uncontinuous surface, where tiny needle or flack shaped particles are randomly dispersed without any preferential orientation.

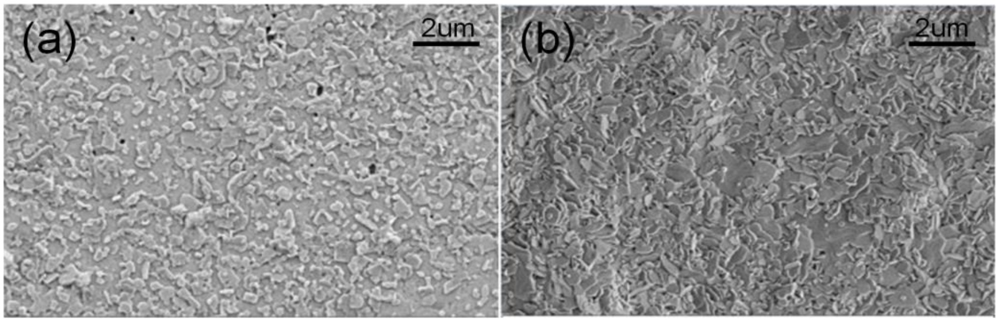

Fig 5.6 *SEM morphology of the TEA (a) and DEA (b) films that annealed at 789 ℃ for 1hour, under the atmosphere of Argon with 100ppm oxygen.*

The different microstructures of the YBCO films can be accounted by the different behavior of the TEA and DEA precursors during heat treatment as revealed by viscosimetry measurements.

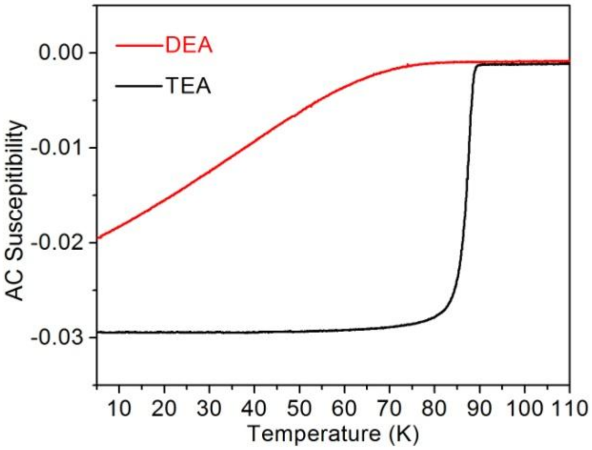

Fig 5.7 *AC suscepitiblity measurement of the YBCO films.*

Finally, the YBCO film produced from the TEA precursor displays a sharp superconducting transition, as shown in **Fig 5.7**. The transition width is just 5K and in spite of a relatively low onset point of 87.5K, a J_c of 1.7MA/cm^2 is estimated at 77K in self field. This result is based on the estimation of an effective area of 0.45×0.42 cm^2 within a 0.5×0.5 cm^2 sized sample. Resulting from the bad microstructure, a much wider transition is observed in the DEA sample, and the J_c of this film is negligible.

5.4 Conclusion

A non-fluorine aqueous sol-gel technique was used to produce YBCO superconducting thin films. The influence of DEA and TEA added as chelating agents was investigated. Though yielding a higher mass loss during the decomposition process, the TEA was demonstrated to be beneficial to the microstructure and superconducting performance of the thin films. As a result, the J_c of the YBCO films produced from TEA chelated precursor reached 1.7MA/cm^2 at 77K, a value approaching that of TFA-MOD derived films.

References

[1] Obradors, X., Puig, T., Pomar, A., Sandiumenge, F., Mestres, N., Coll1, M., Cavallaro, A., Rom`a, N., Azquez, J, G´., Gonz´alez, J, C., Casta˜no, O., Gutierrez, J., Palau, A., Zalamova, K., Morlens, S., Hassini, A., Gibert, M., Ricart, S., Moret´o, J, M., Pi˜nol, S., Isfort, D., Bock, *Supercond. Sci. Technol.* **19**, S13-S26 (2006)

[2] Nakaoka, K., Yoshizumi, M., Izumi, T., Yamada, Y., Shiohara, Y, *Physica C*. **470**, 1242–1245 (2010)

[3] Gyorgy, E, M., van Dover, R, B., Jackson, K, A., Schneemeyer, L, F., *Appl. Phys. Lett*. **55**, 283-285 (1989)

[4] Thuy, T, T., Hoste, S., Herman, G, G., De Buysser, D., Lommens, P., Feys, J., Vandeput, D., Van Driessche, I, *J. Sol-Gel Sci Technol*. **52**, 124-133 (2009)

Chapter 6

Manufacture of $GdBa_2Cu_3O_{7-x}$ superconducting thin films using high thermal stability precursors playing the role of intermediate phase grain-growth inhibitors

(Submitted to IEEE Applied Superconductivity)

We have developed a fluorine-free MOD method using acrylic acid as the solvent for the synthesis of GdBCO superconducting thin films. The commonly used propionic acid was also used so as to make a comparison to acrylic acid. Acrylic acid was found to be polymerized during drying and resulted in a high-thermal-stability of the precursor solution. Due to the elevated decomposition temperature of the organic compounds in the acrylic acid based precursor, the formation of intermediate phases such as CuO was delayed and therefore the grain growth and phase segregation were suppressed. The superior quality of the pyrolyzed films induced by the use of polymerizable acrylic acid is reflected in the J_c of the GdBCO films, which achieved 1.2MA/cm^2.

6.1. Introduction

Large efforts are concentrated on the development of $REBa_2Cu_3O_{7-x}$ (REBCO, RE= rare earth) materials, which are considered as the most promising high temperature superconducting ceramics (HTSC) for power applications including fault current limiters, transformers and wind turbines [1-3]. Among the REBCO materials, due to its higher critical temperature (T_c) and higher critical current density (J_c), GdBCO has became an alternative material to the commonly used YBCO [4], especially when considering magnetic field applications [5].

By now, pulsed laser deposition (PLD) has been successfully used to produce high performance GdBCO films on various substrates. However, keeping the cost and productivity in mind, chemical solution deposition (CSD) can be a more promising method for the scaling-up of the production of GdBCO thin films. As a mature CSD technology, the trifluoroacetate metal organic deposition (TFA-MOD) process had been applied by Iguchi at al. to produce GdBCO thin films with a J_c=2.9MA/cm^2 at 77K [6], however, some intrinsic drawbacks such as complicated pyrolysis process and harmful HF gas release hinders further development of the TFA-MOD technique [7]. To avoid the disadvantages induced by the introduction of TFA, many fluorine-free methods have been developed for producing REBCO thin films. Among the investigations on the fluorine-free methods, some have shown a deterioration of the pyrolyzed amorphous films upon exposure to higher temperature for even very short time [8-10]. W. T. Wang et al. [10] assigned this phenomenon to the undesired growth of CuO nanocrystals and phase segregation in the precursor film during long time pyrolysis. However, between the temperatures required for pyrolysis and for sintering, subsequent long time exposure of the pyrolyzed film to high temperature before the REBCO formation can not be totally avoided, particularly when considering relatively slow motion of tapes in the temperature gradient of reel-to-reel systems for production of long REBCO tapes. Thus it is imperative to explore feasible routes that prevent fast grain growth of the precursor REBCO films before sintering.

In this paper, we shall report on a new fluorine-free CSD method for producing GdBCO thin films by using acrylic acid as polymer solvent. Polymer agents have been widely used in the production of functional ceramics to improve the homogeneity of the precursor solution by forming a gel network [11]. However, in this work, our attention was focused on the effect of the high-thermal-stability of polymerized acrylic acid to suppress the grain growth of intermediate phases forming during and after pyrolysis in the aim of producing high quality GdBCO thin films.

6.2 Experimental Details

For the preparation of the polymer-based GdBCO precursor solution, acetates of gadolinium, barium and copper (Alfa Aesar; 99.9% purity) were mixed in the ratio of Gd:Ba:Cu=1:2:3 by dissolution in acrylic acid (Alfa Aesar; 98% purity). In the following, this solution and the sample made from it will be named “A-based”. To obtain a homogeneous solution, stirring at 60℃ for 1 hour was required. To make a comparison, propionic acid (Alfa Aesar; 98% purity) was also used as solvent for the mixed acetates to obtain a “P-based” solution by using the same preparation process. By adjusting the volume of acid solvent, the total cation concentration of both solutions was controlled at 1.5mol/*l*. For the deposition process, the precursor solutions were spin-coated with a rotation-speed of 6000rpm onto 5×5 LAO single crystal substrates. After coating, the wet precursor films were placed in a tabular furnace and heated up to 500-600℃ with a ramp speed of 10℃/min in a pure oxygen atmosphere. Sintering was then made at temperatures ranging from 790 to 820℃ for one hour under Ar/100ppmO_2 mixed atmosphere. The samples were finally cooled down to 450℃ at the rate of 5℃/min and held at this temperature for 15 hours under pure oxygen to transform the phase from tetragonal to orthorhombic.

The thermogravimetry (TG), differential thermal analysis (DTA) and Fourier transform infrared (FTIR) measurements were carried out using a model 449C device from Netzsch with a Bruker Tensor 27 spectrometer connected for monitoring the released gas. The samples for TG/DTA measurement were prepared by drying the precursor solutions at 90℃ for 10 hours on a heating plate in order to remove the excess solvent. The P-based sample was dried into powders, however, due to the polymerization that occurred during drying, polymerized acrylic acid was retained in the precursor and the A-based sample remained in gel form. The phase assemblage and microstructure of the pyrolyzed and sintered films were characterized by X-ray diffraction (Bruker D8, Cu Kα radiation) and scanning electron microscopy (SEM Supra 35). AC susceptibility and hysteresis loops were measured in a CRYOGENIC cryogen free measuring system (CFMS). The critical current density (J_c) of the samples was calculated by using the extended Bean critical state model [12].

6.3 Results and Discussion

The high thermal stability of the acrylic acid based precursor is illustrated in the TG and FTIR measurements, as shown in **Fig 6.1** and **Fig 6.2**, respectively. The mass loss of the P-based precursor sample took place from 50℃ to 450℃, and is divided into three main steps, resulting in a mass loss of 55%. In contrast, the A-based sample underwent decomposition only in two broad steps and results in a higher mass loss of 65%, which is completed at 600℃.

Considering the overlapping decomposition steps of the individual acrylates and propionates, it is difficult to interpret in details the whole decomposition behavior of the A-based and P-based precursors. However, previous publications studying the individual thermal behaviors of related propionates [13-15] and acrylates [16-18] showed that the decay of the acrylates follows decomposition processes analogous to the propionate counterparts and results in the same final products as shown in the equations (1-3):

$$Cu\,(CH_3CH_2COO)_2 \rightarrow Cu \rightarrow CuO \quad (1)$$

$$Ba\,(CH_3CH_2COO)_2 \rightarrow BaCO_3 \quad (2)$$

$$Gd\,(CH_3CH_2COO)_3 \rightarrow Gd_2O_2CO_3 \rightarrow Gd_2O_3 \quad (3)$$

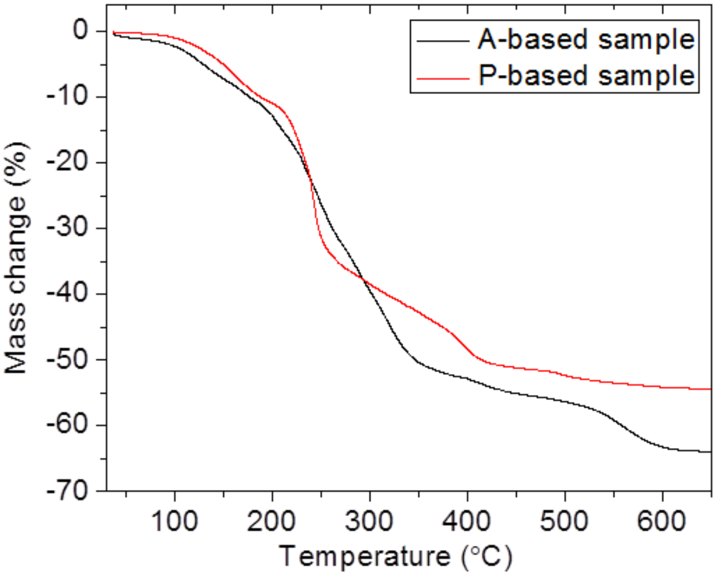

Fig 6.1. *TG curves of the Acrylic acid based precursor (A-based sample) and the Propionic acid based precursor (P-based sample) measured in a flow of pure oxygen.*

In view of the similar molecular weight of acrylic acid (72 g/mol) and propionic acid (74 g/mol) and considering that the same inorganic salts of Gd, Ba, and Cu were left after pyrolysis, it is reasonable to assign the higher mass loss of the A-based precursor to the polymerization of acrylic acid during drying, as the formation of long molecular chains from a fraction of the solvent may increase the thermal stability of the gel and postpone the release of part of the solvent to a temperature higher that used for drying, i. e. a part of the solvent was only released during the TG measurement.

This hypothesis can be confirmed from the FTIR spectra recorded in situ on the evolved gases during decomposition of the samples as depicted in **Fig 6.2**. In the spectra recorded at 180℃, the P-based sample showed a qualitatively evenly matched release of both CO_2, H_2O, and the symmetrical ketone product 3-pentanone, which is featured by the anhydride C-O-C stretch at 1760cm^{-1} accompanied with the C-O stretch at 1169-1240cm^{-1} [13]. In contrast, the anhydride C-O-C and C-O stretches were found dominant in the gas released from the A-based sample. Besides, the presence of the double carbon bond initially present in acrylic acid is reflected in the C=C stretch visible at 1620cm^{-1} in the gaseous products released from the A-based sample. The presence of this signature probably implies a release of 1,4-pentadien-3-one. The higher fraction of anhydrides released from the A-based sample compared to that from the P-based sample was on the one hand due to the high amount of residual acrylic acid after drying, on the other hand due to the stable C=C bonds in acrylic acid, which are hardly decomposed into CO_2 and H_2O at low temperatures. With the temperature rising to 330℃, only CO_2 and H_2O were found as the combustion products in both samples. At 520℃, the gas release was found to be practically finished in the P-based sample, however, the CO_2 release was found still in progress in the A-based sample, implying a delayed combustion of the polymerized acrylic acid to higher temperatures. This result corresponds well to the second mass loss step from 400℃ to 600℃ in the A-based sample as shown in **Fig 6.1**.

Based on the delayed decomposition of the organic compounds of the A-based sample at temperatures up to 600℃, it is conceivable that the grain growth of the intermediate phases could be somehow suppressed during the so-called intermediate temperature stage taking place after the removal of the organic compounds and before the GdBCO formation. Our hypothesis is demonstrated in the XRD patterns shown in **Fig 7.3**. The P-based film already showed the crystallized $BaCO_3$ and CuO phases when quenched out at 400℃. However, the A-based film revealed a totally amorphous structure without any peaks as expected from the unfinished decomposition that has been observed in the TG and FTIR results. The $BaCO_3$ and CuO phases appeared on the A-based film as the temperature increased to 600℃, however, the intensities of the peaks were much lower compared to those of the P-based film, implying a greatly suppressed growth of $BaCO_3$ and CuO grains.

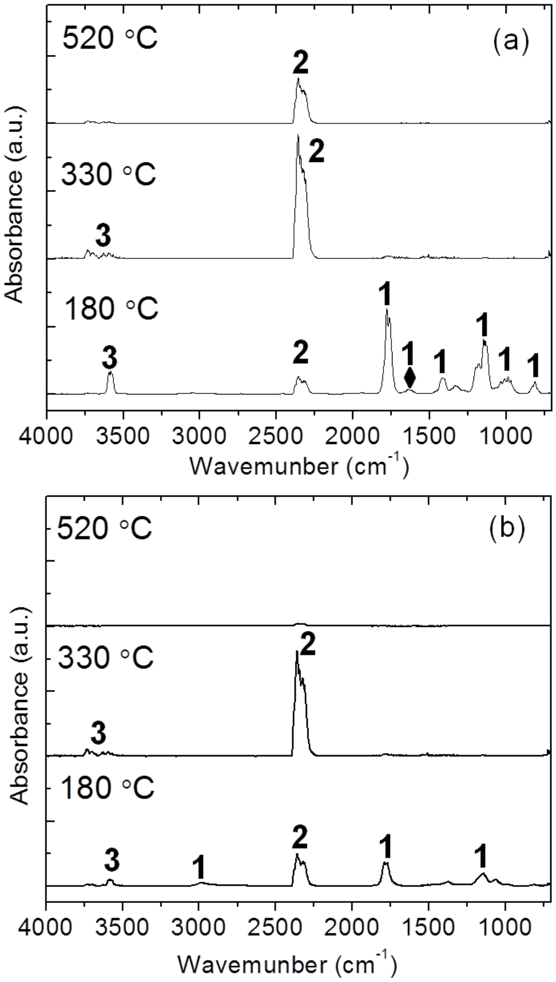

Fig 6.2 *FTIR spectra of gaseous phases evolved from the Acrylic acid based precursor (a) and Propionic acid based precursor (b) at different temperatures during decomposition. Peaks marked with "1" correspond to* $C_2H_3COC_2H_3$ *and* $C_2H_5COC_2H_5$ *phases in Acrylic acid based precursor and Propionic acid based precursor, respectively; peaks marked with "2" correspond to* CO_2*; peaks marked with "3" correspond to* H_2O *phase; the peak marked with "♦"corresponds to the vibration of C=C double bonds.*

The morphology of the A and P based films quenched out at 600℃ as shown in **Fig 6.4** (a) and **(c)** also supports this conclusion. The A-based film showed a homogeneous wrinkling morphology with some very tiny particles dispersed on the surface. In contrast, some square shaped particles up to 200-300nm in length were clearly observed on the surface of the P-based film. EDX analysis performed on the particles showed a copper rich composition, corresponding exactly to the statement by W. T. Wang et al. [10]. The XRD and SEM results on the quenched samples revealed the fact that the polymer matrix around the metal centers up to 600℃ can play a key role on the size control of the intermediary phase.

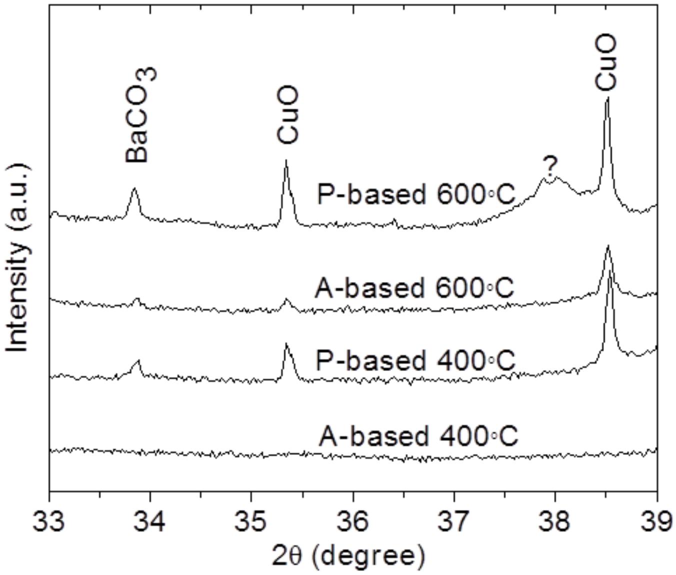

Fig 6.3 *XRD patterns collected on Acrylic acid based precursor (A-based sample) and Propionic acid based precursor (P-based sample) quenched out at 400 ℃ and 600 ℃.*

Due to the narrowed gap between the temperature required for the decomposition of organic compounds and for the formation of the GdBCO superconducting phase, a greater surface area was provided by the refined reactant particles without any undesired grain growth and segregation. As a consequence, the crystallization of GdBCO with preferred orientation was dramatically enhanced after sintering at 820℃ for one hour. As shown in the XRD pattern in **Fig 6.5**, the intensity of the GdBCO (00*l*) peaks of the A-based film was nearly three time higher than that of the P-based film. Also in **Fig 6.4 (c)**, a continuous surface morphology was observed on the A-based film, whereas the P-based film showed a more randomly oriented polycrystalline structure (**Fig 6.4(d)**), which gives rise to weak links between the GdBCO grains.

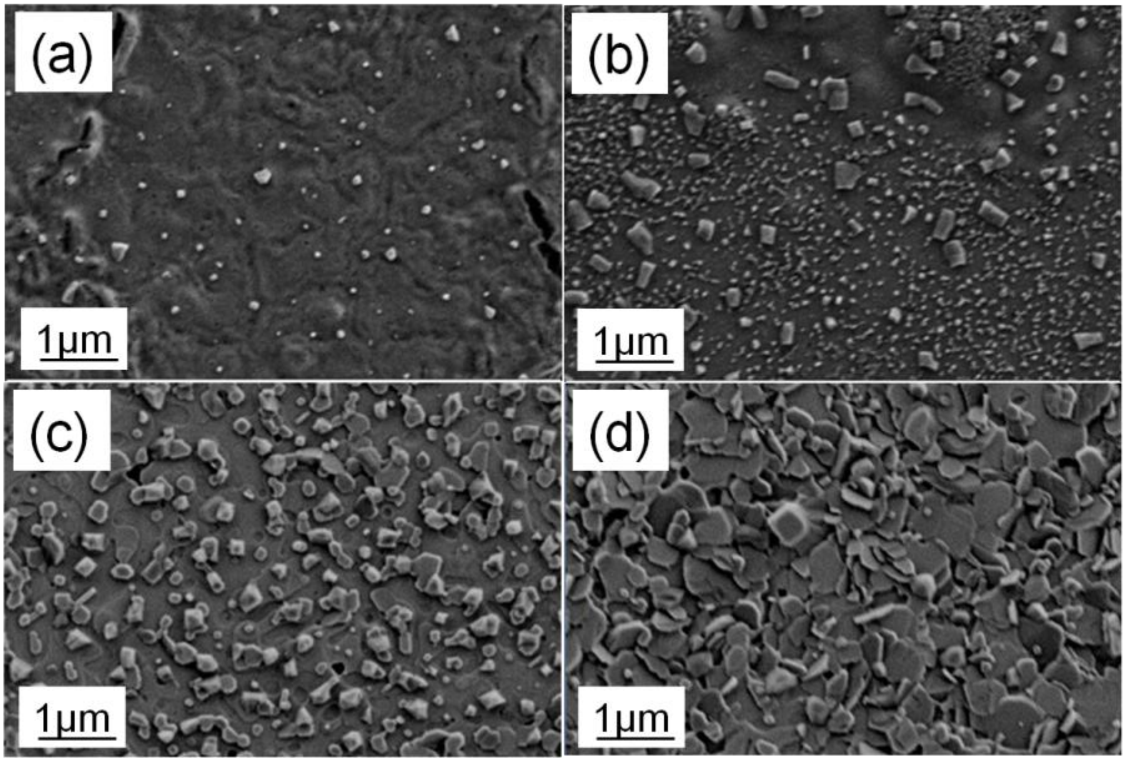

Fig 6.4. *SEM micrograph of Acrylic acid based films (a, c) and Propionic acid based films (b, d) quenched out at 600 ℃ (a, b) and sintered at 820 ℃ for one hour (c, d).*

The result of AC susceptibility measurements of the sintered GdBCO films is shown in **Fig 6.6** Obviously the A-based sample displays a very sharp superconducting transition, which starts from 91.5K and finished within 5K. In contrast, the P-based film shows a sluggish transition, which contains two steps. The second step that starts from 82K, which is accurately corresponding to the T_c of $GdBa_2Cu_4O_8$ (Gd124) phase [19], suggesting the possibility of the formation of some Gd124 phase in the vicinity of the copper-rich phases shown in **Fig 6.4 (b)**. By using the extended Bean critical state model, the critical current density (J_c) of the A-based GdBCO film is estimated to approximately 1.2MA/cm^2 under self field, while that of the P-based film is only 0.32MA/cm^2 at 77K.

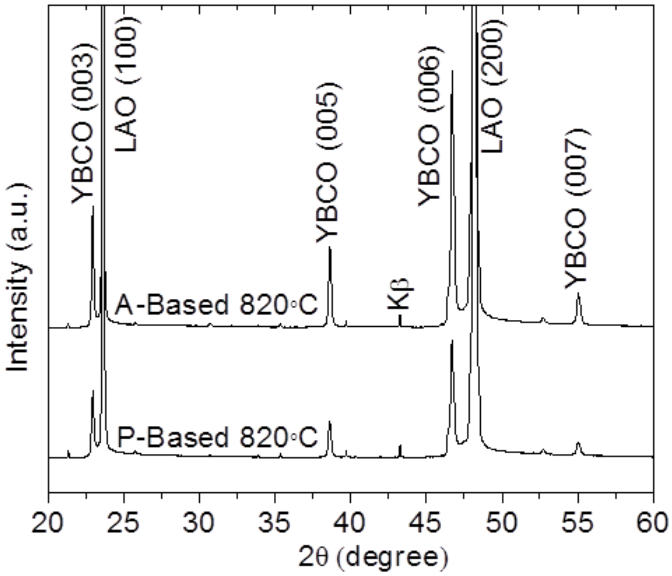

Fig 6.5 *XRD patterns collected on Acrylic acid based precursor (A-based sample) and Propionic acid based precursor (P-based sample) annealed at 820 ℃ in Ar/100ppm*O_2 *for one hour.*

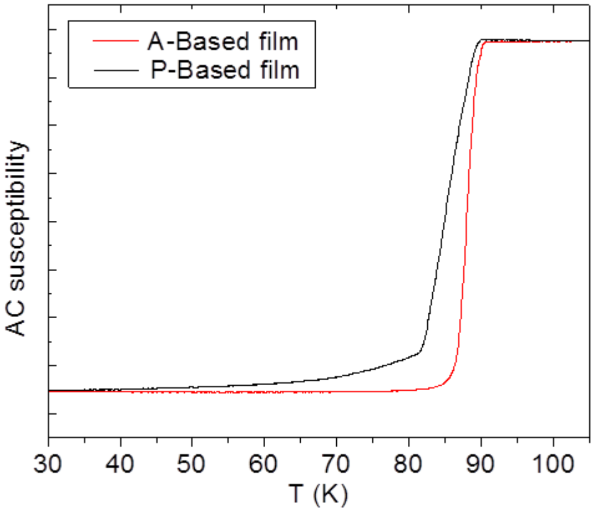

Fig 6.6 *AC susceptibility (real part) measured on films made with Acrylic acid based precursor (A-based film) and Propionic acid based precursor (P-based film) annealed at 820 ℃ in Ar/100ppm*O_2 *for one hour.*

7.4 Conclusion

GdBCO superconducting films have been prepared by a fluorine-free MOD method using either propionic acid or acrylic acid as the solvent. Polymerization occurred in the acrylic acid based solution during heating and resulted in high thermal stability of the precursor. Consequently the grain growth and segregation of CuO was greatly suppressed in the films made from this precursor. Due to the more homogeneous distribution and smaller particle size of the intermediate phases after pyrolysis, superior microstructure and superconducting performance was obtained in the acrylic acid based GdBCO thin film in comparison to the propionic acid based thin film.

References

[1] D. K. Park, M. C. Ahn, S. E. Yang, Y. S. Yoon, B. Y. Seok, C. Lee, H. M. Chang, T. K. Ko, *IEEE Trans. Appl. Supercond*. **17** (2007) 1863.

[2] H. Okubo, C. Kurupakorn, S. Ito, H. Kojima, N. Hayakawa, F. Endo, M. Noe, *IEEE Trans. Appl. Supercond*. **17** (2007) 1768.

[3] A. B. Abrahamsen, B. B. Jensen, E. Seiler, N. Mijatovic, V. M. Rodriguez-Zermeno, N. H. Andersen, J. Ostergard, *Physica C*. **471** (2011) 1467.

[4] H. Fukushimaa, A. Ibia, H. Takahashia, R. Kurikia, S. Miyataa, Y. Yamadaa, Y. Shiohara, *Physica C*, **463-465** (2007) 501.

[5] M. Murakami, N. Sakai, T. Higuchi, S. I. Yoo, *Supercond. Sci. Technol*. **9** (1996) 1015.

[6] T. Iguchi, T. Araki, Y. Yamada, I. Hirabayashi, H. Ikuta, *Supercond. Sci. Technol*. **15** (2002) 1415.

[7] Y. Xu, A. Goyal, N. A. Rutter, D. L. Shi, *J. Mater. Res*. **18** (2003) 677.

[8] T. Nakamura, R. Kita, O. Miura, A. Ichinose, K. Matsumoto, Y. Yoshida, M. Mukaida, S. Horii, *Physica C*, **468** (2008) 1542-1545.

[9] Y. Xu, A. Goyal, N. A. Rutter, D. Shi, M. Paranthaman, S. Sathyamurthy, P. M. Martin, D. M. Kroeger, *J. Mater. Res*, **18** (2003) 677-681.

[10] W. T. Wang, X. F. Yang, M. H. Pu, H. Zhang, C. H. Cheng, Y. Zhao, *Journal of Superconductivity and Novel Magnetism*, **25** (2012) 39-44.

[11] A. L. Quinelato, E. Longo, E. R. Leite, M. I. B. Bernardi, J. A. Varela, *JOURNAL OF MATERIALS SCIENCE*. **36** (2001) 3825.

[12] E. M. Gyorgy, R. B. van Dover, K. A. Jackson, L. F. Schneemeyer, J. V. Waszczak, *Applied Physics Letters*. **55** (1989) 283.

[13] J.-C. Grivel, *Journal of Thermal Analysis and Calorimetry*, **109** (2012) 81 – 88.

[14] E. Gobert-Ranchoux, F. Charbonnier, *Journal of Thermal Analysis and Calorimetry*, **65** (1977) 33-42.

[15] A. Kaddouri, C. Mazzocchia, *Journal of Analytical and Applied Pyrolysis*, **65** (2002) 253 – 267.

[16] E. I. Aleksandrova, G. I. Dzhardimalieva, A. S. Rosenberg, A. D. Pomogailo, *Russian Chemical Bulletin*, **42** (1993) 295-263.

[17] P. H. Mccluskey, G. S. Fischman, R. L. Synder, *Journal of Thermal Analysis*, **34** (1988) 1441-1448.

[18] W. Balcerowiak, J. Hepter, J. Beres, J. Olkowska, *Journal of Thermal Analysis*, **11** (1977) 101-107.

[19] M. Baran, V. Dyakonov, L. Gladczuk, G. Levchenko, S. Piechota, H. Szymczak, *Physica C*, **241** (1995) 383-388.

Chapter 7

High-J_c $YBa_2Cu_3O_{7-x}$-Ag superconducting thin films synthesized through a fluorine-free MOD method

(Status suspended due to the confidentiality of the patent)

(A Novel SAFF-MOD Technique to Produce High-Jc YBCO Superconducting Films, European Patent, 2013)

Obtaining high critical current density (J_c) remains the main challenge of the development of fluorine-free metal organic deposition (MOD) methods to fabricate YBCO superconducting thin films. Silver-doping is applied to enhance the J_c values. By reacting with propionic acid and ammonia, $AgNO_3$ was initially mixed with YBCO carboxylate precursors dissolved in methanol. High-temperature in-situ XRD measurements of the YBCO-Ag powders revealed that silver addition lowers the incongruent melting temperature of YBCO, which results in a smooth surface morphology of the YBCO films at a temperature as low as 760℃. Grain growth and intergranular conductivity were also found to be improved by silver doping. After annealing under optimized conditions, a high J_c of 4.6MA/cm^2 was obtained in a YBCO-Ag thin film with 10 wt% Ag.

7.1 Introduction

Fabricating films with high phase purity and good orientation at high efficiency and low cost, remains the challenge for the production of $YBa_2Cu_3O_{7-x}$ (YBCO) coated superconductors. Among all the techniques to fabricate YBCO films, metal-organic deposition using trifluoroacetes as precursors (TFA-MOD), which was firstly proposed by Gupta et al in 1988 [1], has been extensively studied and is one of the most promising routes [2-4], as it requires no vacuum equipment and is applicable for long-length tape fabrication. Although a critical current density (J_c) exceeding 10MA/cm^2 can be achieved by using the TFA-MOD process [3], the sluggish removal of the by-product HF gas results in a time-consuming pyrolysis process [5].

As alternatives to the TFA-MOD process, some fluorine-free MOD methods are being developed to avoid the release of hazardous products taking place during the decomposition of the precursor materials and to speed up the pyrolysis step [6-8].

However, the J_c values of the films derived from early developed fluorine-free MOD methods are generally below 1MA/cm^2 [6-8]. This drawback often results from the formation of $BaCO_3$ residues, which is quite stable during sintering and suppresses the formation of the YBCO phase [9]. This is the most important factor that hinders the further development of fluorine-free MOD processes. By further optimizing the method described in [6], L. Li et al. obtained a J_c value of 1.83MA/cm^2. This was assigned to a water vapor partial pressure induced intermediate phase conversion from $BaCO_3$ into $Ba(OH)_2$, which can serve as barium source to generate the YBCO phase [10]. Meanwhile, with the help of UV-lamp irradiation, a group in Japan achieved a J_c value higher than 6MA/cm^2 on films deposited on single crystals by using a novel solution [11].

Silver addition might be another promising route to increase the J_c of YBCO thin films produced by means of fluorine-free MOD methods. Many studies have been done to investigate the effect of silver addition on YBCO thin films. With pulsed laser deposition (PLD), a remarkable high J_c of 14MA/cm^2 was achieved by using an YBCO-Ag target [12]. This impressive result was attributed to the supply of active oxygen from Ag_2O, which facilitates the growth of YBCO grains. Similarly, P. Selvam et al [13] reported an enhanced J_c in Ag-doped YBCO thin films by using the PLD technique. In contrast to D. Kumar et al. [12], they described the positive impact of silver as forming improved YBCO grain boundaries and better grain alignment, more than behaving as oxygenation catalyst.

Athough there are plenty of reports on PLD manufactured YBCO-Ag films as well as bulk materials prepared from solid state reaction [14-16], studies on the synthesis of YBCO-Ag thin films by MOD methods are scarce. A reason could be the bad adaptability of silver salts to the YBCO precursor solution. In fluorine-free MOD methods, silver tends to precipitate as a result of its reaction with the amino-group containing complexants which are normally indispensable to prevent the metal salts from hydrolysis, in the absence of trifluoroacetic acid.

In this work, we developed a homogeneous fluorine-free YBCO-Ag precursor solution in order to make the J_c of fluorine-free MOD derived YBCO films comparable to that from traditional TFA-MOD films.

7.2 Experimental details

Acetates of Y, Ba and Cu (Alfa Aesar) weighed to obtain a molar ratio of 1:2:3, and mixed with different weight percentages (0, 5, 10, 15, 20%) of $AgNO_3$ (Alfa Aesar), were dissolved in a mixture of propionic acid and ammonia, which was prepared at the volume ratio of 3:1. After one hour stiring at 80℃ on heating plates, the solutions became clear blue without any precipitation. Afterwards, all the extra solvent was removed by an evaporator. During this process, deionized water was added to help the removal of acid until a blue glassy gel was obtained. Finally, the gels were dissolved in methanol (Alfa Aesar), to yield a homogeneous solution with a total metal concentration (Y, Ba and Cu, without Ag) of 1.5mol/L. Precursor films were prepared by spin coating on $5\times5mm^2$ $LaAlO_3$ (LAO) substrates at a speed of 4000 rpm/min for 60 seconds. The precursor films were then decomposed to amorphous films in a tube furnace by heating up to 450℃ at a ramping speed of 10℃/min under humid oxygen gas flow. After cooling down, the furnace was heated to 790℃ at a ramping speed of 20℃/min and holding for one hour under N_2 atmosphere with controlled oxygen partial pressure. During cooling down, oxygenation was made at 450-525℃ for five hours in pure oxygen. The pellets used for shrinkage measurement were composed of YBCO and YBCO-Ag precursor powders pyrolyzed at 500℃ and were pressed into cylinders of a size of 5mm in diameter and 2mm in thickness.

High-temperature in-situ and room temperature theta-two-theta X-ray scans, phi scans and rocking curves were collected by means of a BrukerD8 advance X-ray diffreactometer with CuKa radiation. The microstructure and morphology of the films were investigated in a supra 35 scanning electron microscopy (SEM) from Zeiss. The resistivity the film samples was measured by a FLUKE (8020B) multimeter at room temperature. The shrinkage of the pure YBCO and YBCO-Ag pellets were measured by using a DIL 402 E dilatometer under Argon atmosphere, followed by density measurements using an ultrapycnometer 1000 density analyzer. Simultaneous TG/DTA (STA449C) was used to investigate reaction behavior of the decomposed YBCO and YBCO-Ag powders.

The cross-section microstructure of the YBCO-Ag thin film was characterized by using a JEOL 3010-F-type high-resolution transmission electron microscope (HRTEM).

AC susceptibility and hysteresis loops were measured by CRYOGENIC cryogen free measuring system (CFMS). The critical current density (J_c) of the samples was calculated by using the extended Bean critical state model [17].

7.3 Results and Discussion

7.3.1 Mechanism of the improvement by silver-doping

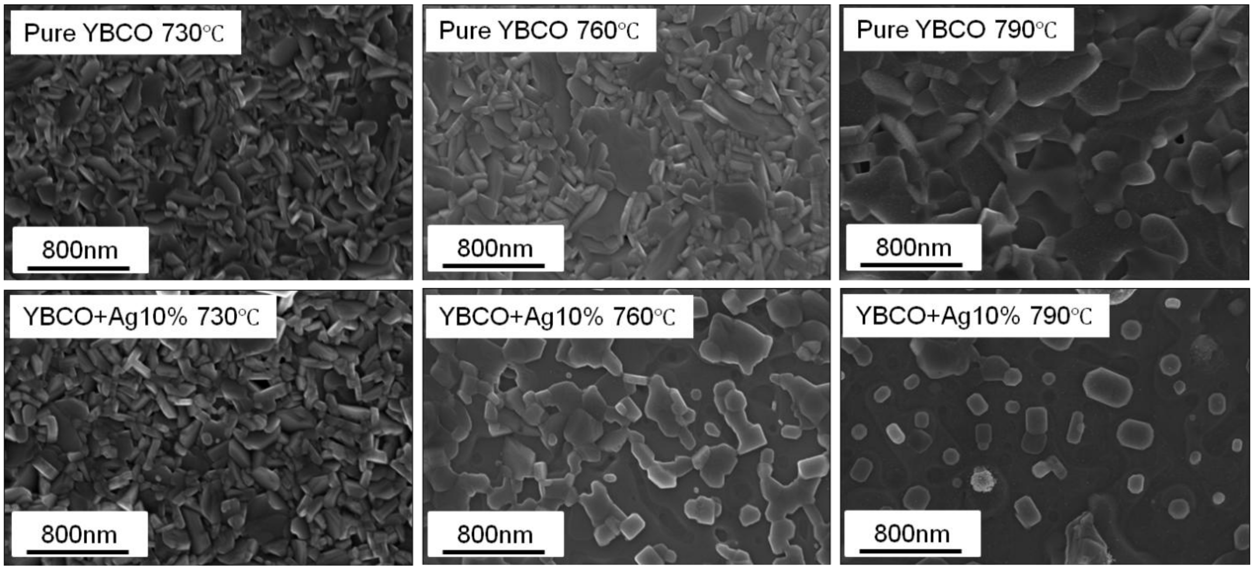

Fig 7.1 *SEM images of pure YBCO and YBCO+Ag10wt% films sintered at different temperatures for one hour in an atmosphere of* N_2 *mixed with 100ppm oxygen.*

Fig 7.1 shows the SEM micrographs of pure YBCO and YBCO+Ag10wt% films sintered at different temperatures for one hour in an atmosphere of N_2 mixed with 100ppm oxygen. No obvious difference can be seen from the samples sintered at 730℃. However, when the temperature increases to 760℃, grains in the silver-doped film have nearly melted together without clear grain boundaries, in contrast to the pure YBCO film, which still shows randomly oriented grain growth. As the temperature further increases, the difference between the films becomes less evident. However, the silver-doped films still show higher smoothness and lower porosity.

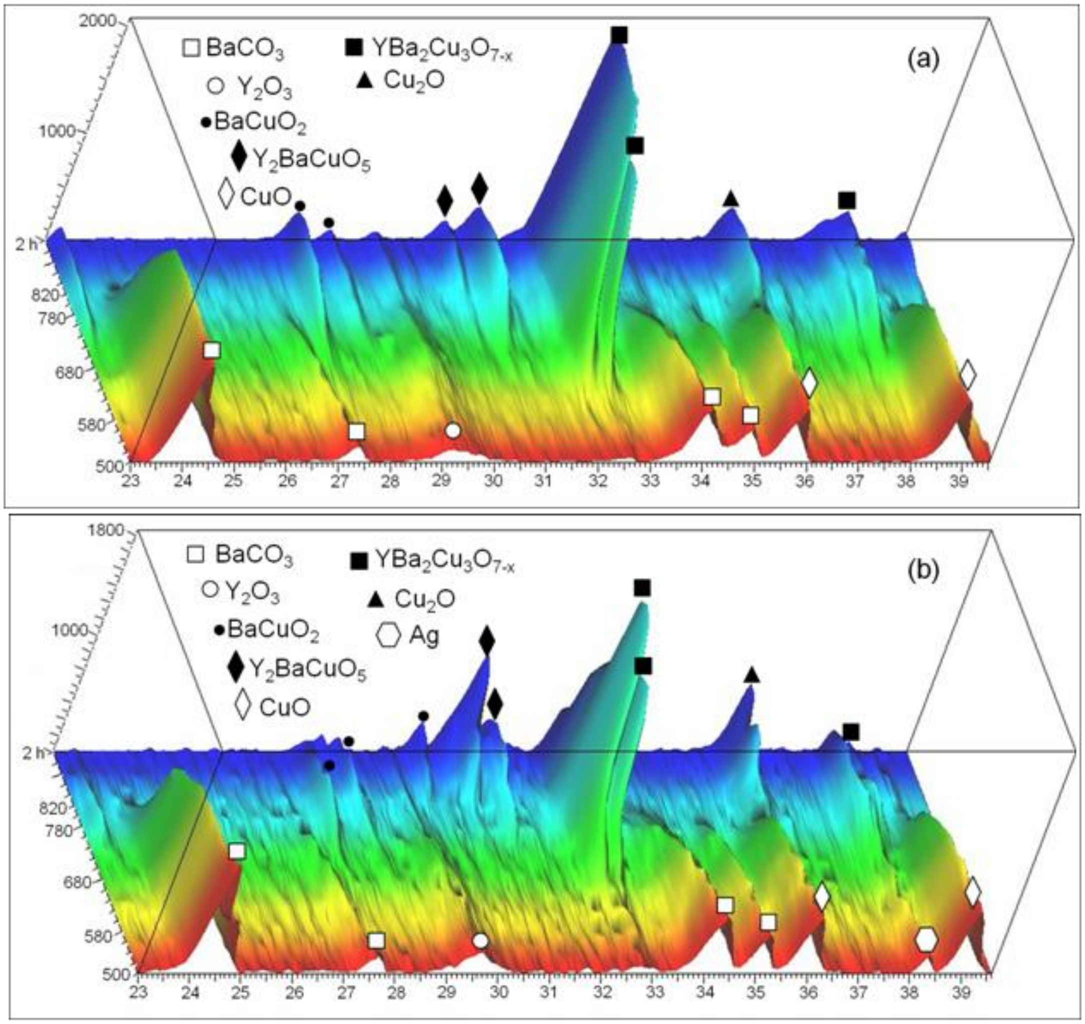

Fig 7.2 *3D view of high-temperature in-situ XRD measurements on (a) pyrolysed pure YBCO precursor powder. (b) pyrolysed YBCO-Ag precursor powder.*

A similar phenomenon was observed on TFA-MOD derived YBCO-Ag composite films by Obradors et al. [18]. These authors claimed that silver doping results in a larger temperature window for YBCO thin film processing temperatures. Although using totally different processes, where $BaCO_3$ and BaF_2 appear as dominant Ba-containing intermediate products respectively after decomposition, we propose that a similar mechanism is at play to explain the YBCO growth enhancement by silver, that silver can dramatically reduce the peritectic temperature, which is crucial to the YBCO formation along the c-axis, by enhancing the atomic mobility of the reactants.

To investigate and prove the reaction mechanism induced by silver addition, high-temperature in-situ XRD measurements were conducted on pyrolysed YBCO and YBCO-Ag precursor powders. To accurately simulate the reaction process of the thin films, the oxygen partial pressure was also controlled at around 100ppm.

As shown in **Fig 7.2(a) and (b)**, $BaCO_3$, CuO and Y_2O_3 are the products of carboxylates after pyrolysis while metallic silver can be observed in the silver-doped sample. The most intensive reflections of the $BaCO_3$, CuO, YBCO and Y211 phases are plotted as a function of temperature in **Fig 7.3**.

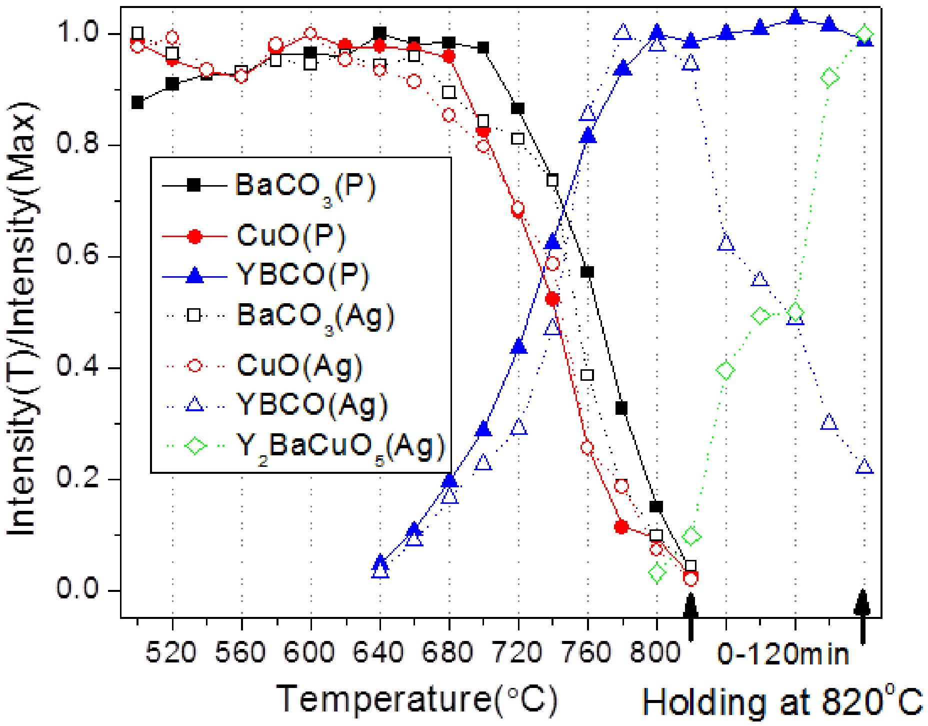

Fig 7.3 *Evolution of important phases in pyrolysed pure YBCO and YBCO-Ag powders during sintering.*

For both samples, YBCO starts forming at a temperature as low as 640℃ upon the consumption of Y_2O_3, $BaCO_3$ and CuO, and is dominant above 750℃. The reaction behavior of the samples is corresponding well to the established model for YBCO formation through fluorine-free methods during annealing in low oxygen content atmosphere, which is basically governed by two steps, where the liquid (L1) is composed of barium and copper [19]:

$$2BaCO_3 + 3CuO \rightarrow L1 + \frac{3}{4}O_2 + 2CO_2 \qquad (1)$$

$$\frac{1}{2}Y_2O_3 + L1 \rightarrow YBa_2Cu_3O_{6+x} \qquad (2)$$

Although the decomposition of $BaCO_3$ and CuO seems promoted by silver addition, especially within the low temperature region, the formation of YBCO is not facilitated. Thus the phase evolution at low temperature can not provide an explanation for the fast grain growth at 760℃ as shown in the SEM figures.

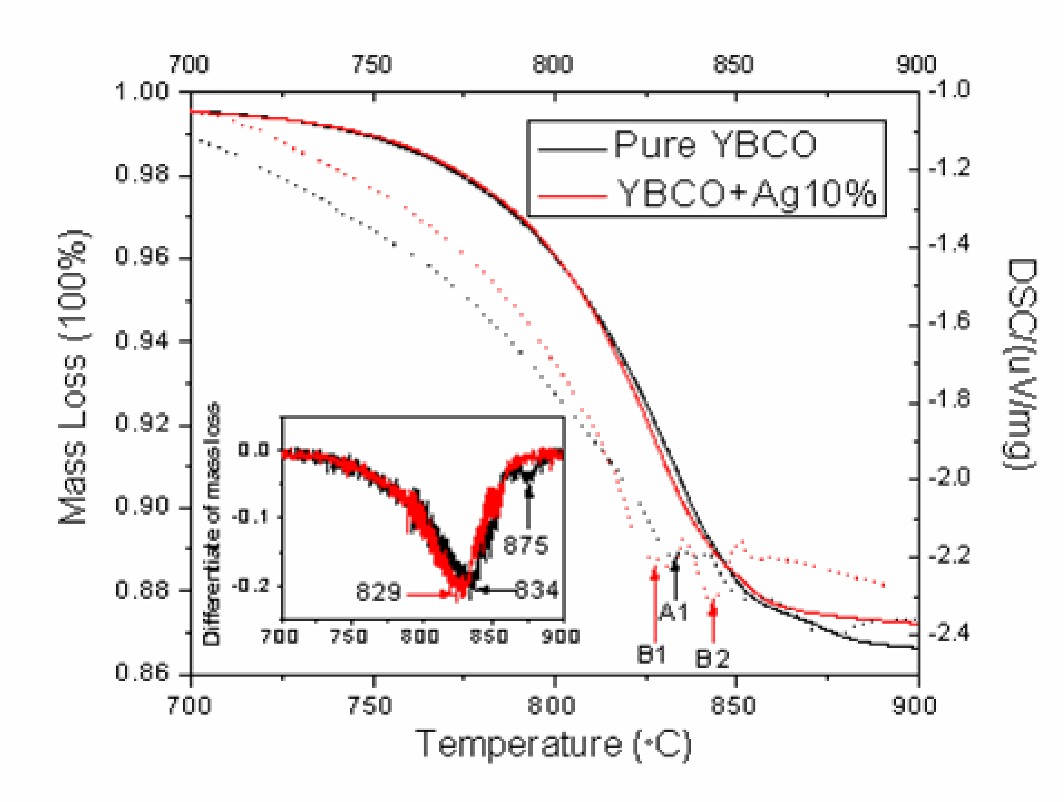

Fig 7.4 *TG-DSC spectra in Ar for pyrolysed pure YBCO precursor powder and pyrolysed YBCO-Ag precursor powder.*

Compared to the pure sample, when the temperature reaches at 800°C and during holding at 820°C, decomposition of YBCO takes place in the presence of silver, and results in the formation of $BaCuO_2$, Y_2BaCuO_5 (Y211) and Cu_2O phases. Although the Y211 phase was detected in the pure YBCO sample as well, its most intense reflection was not dominant, as shown in **Fig 7.2 (a)**. This so-called peritectic reaction is described as [20]:

$$CuO + YBa_2Cu_3O_{6+x} \rightarrow Y_2BaCuO_5 + BaCuO_2 + Cu_2O \qquad (3)$$

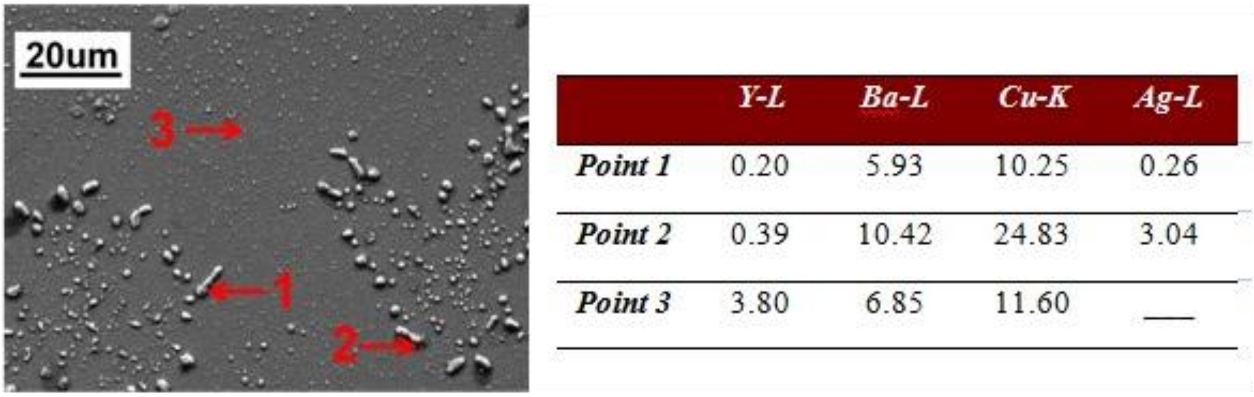

	Y-L	*Ba-L*	*Cu-K*	*Ag-L*
Point 1	0.20	5.93	10.25	0.26
Point 2	0.39	10.42	24.83	3.04
Point 3	3.80	6.85	11.60	—

Fig 7.5 *EDX measurements on the YBCO+Ag10wt% film sintered at 790 ℃ for one hour in an atmosphere consisting of* N_2 *mixed with 100ppm oxygen.*

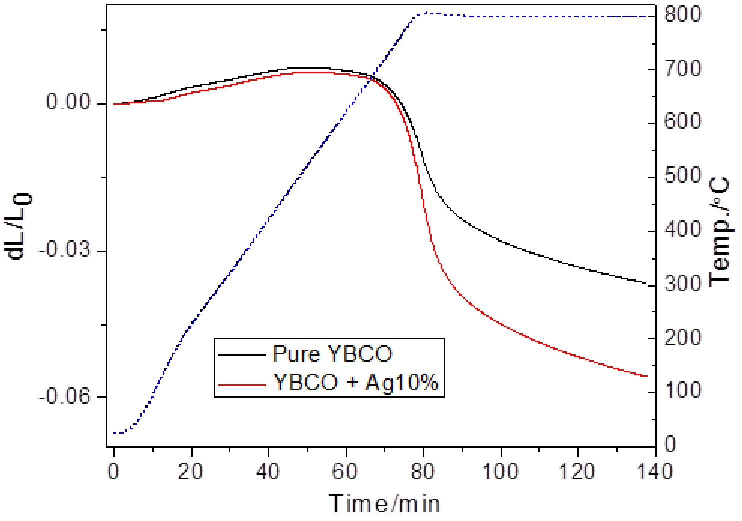

Fig 7.6 *Shrinkage measurement of the pellets composed of pure YBCO and YBCO-Ag powders in Ar atmosphere.*

The decomposition of the YBCO superconducting phase is not favorable. However, it is associated to the incongruent melting of YBCO, which is beneficial for achieving dense and textured films. W. T. Wang et al. [21] and T. H. Tiefel et al. [22] reported the enhanced grain growth and improved surface morphology by pure YBCO partial melting heating treatment at 815℃ with oxygen partial pressure at a ppm level, and at 980℃ in pure oxygen with silver catalyst, respectively. Peir-Yung Chu et al. described [23, 24] these melting-assisted processes as rearrangement towards the desired orientation that happens at high-temperature in low P_{O2} after the crystallization of the YBCO phase, which remains the key to the production of any type of solution-derived YBCO thin films.

The reaction behavior of the decomposed YBCO and YBCO-Ag powders was also investigated by means of TG and DSC measurements as shown in **Fig 7.4**. Under Ar atmosphere, a 12% weight loss was seen on both powders, with and without silver addition from 700℃ to 850℃, caused by the release of CO_2 related to $BaCO_3$ consumption during YBCO formation. The derivative plots of the mass loss of the pure YBCO and YBCO+Ag10% samples show inflection points at 834℃ and 829℃ respectively, where the endothermic peak A1 and B1 can be seen in the DSC trace. Interestingly, following the main mass loss, another minor mass loss of 0.75% can be seen only in the pure YBCO sample. The maximum rate of this mass loss is found at 875℃. According to P. Vermeir et al [19], this can be attributed to the reduction of the remaining CuO, where the release of O_2 takes place. However, the remaining CuO can be consumed in another way. This can be inferred from the endothermic peak (B2) that takes place at the end of the YBCO formation, simultaneously without any acceleration of the mass loss. Relating to the results of the in-situ XRD measurements, it is rational to assign peak B2 to the melting and decomposition of YBCO, associated to the remaining CuO. As a result, no obvious mass loss relating to the reduction of CuO can be seen at higher temperature in the Ag-doped sample.

The EDX results also support our speculation. It is easy to spot clustered particles anywhere on the surface of the 10wt% Ag-doped sample. Silver is absent in the flat regions, where yttrium, barium and copper are basically within the theoretical stoichiometry of YBCO. Interestingly, trace amounts of silver were found in association with the agglomerated particles, which don’t contain significant amounts of yttrium. This means that the decomposition of YBCO, as expressed in equation (3), might have happened on the thin film to some extent, although not severely. Upon the decomposition of YBCO, silver was dissolved in the Ba/Cu liquid, and pushed out onto the surface.

Shrinkage measurements can allow a better understanding of the effect of silver-induced incongruent melting of YBCO on the morphology of the YBCO thin films. As shown in **Fig 7.6**, compared to the 4% shrinkage of the pure sample, the silver-doped sample shows a shrinkage value of 6% after one hour sintering. Density measurements were also done on these two samples and revealed that the pure YBCO pellet had a density of 5.8g/cm^3 whereas that of the YBCO-Ag pellet is 6.1g/cm^3. This reveals a higher densification and a lower porosity resulting from the incongruent melting of YBCO. By adding silver, a similar behavior might happen in the thin films at a relatively lower temperature, leading to surface morphologies as shown in **Fig 7.1**.

Although the mechanisms for the YBCO powder formation and YBCO thin films formation might be relatively different, it is conceivable that silver doping has a similar role in both of them. Here, according to the SEM figures accompanied by in-situ XRD and TG-DSC measurement results, we rationally speculate a much more lowered incongruent melting point of non-fluorine MOD method derived YBCO thin film at 760℃ when annealing with low oxygen content atmosphere, with the silver additive catalyst. On the other hand, the severe decomposition of YBCO as shown in the in-situ XRD results couldn’t happen simultaneously with the melting of YBCO in the YBCO-Ag thin films. This can be reflected from the high J_c values as shown in the following. Different from the long duration of in-situ XRD measurements, where the YBCO phase has completely formed during the long time continuous theta-to-theta scanning before the temperature reaches the set point, in the thin film production, the YBCO content was certainly still low as the temperature was swiftly ramped to target. Thus the equilibrium of equation (3) was shifted to the left side and the decomposition of YBCO was limited at quite a low level, so that the melting could only take place to some extent. According to our understanding, by modifying the equation (2), here, we propose a direct liquid-phase YBCO formation that is allowed by the addition of silver:

$$\frac{1}{2}Y_2O_3 + L1 + L\ (Ag) \rightarrow L\ (YBa_2Cu_3O_{6+x}) + L\ (Ag) \qquad (4)$$

7.3.2 Silver-doping dependence of microstructure of the YBCO-Ag films

Fig 6.7 shows XRD patterns of YBCO films with different Ag-doping levels annealed at 790℃ for one hour. Only (00*l*) peaks characteristic for c-axis orientation are observed on both the pure and Ag-doped YBCO films. The intensity of the (00*l*) YBCO peaks, especially the (005) peaks, increase with Ag-doping, while the FWHM values decrease as shown in **Fig 7.8** for the (005) peaks, implying a better crystallization induced by Ag-doping. The peak corresponding to metallic silver (111) is only visible in the 20wt% Ag-doped sample and not detected in the others.

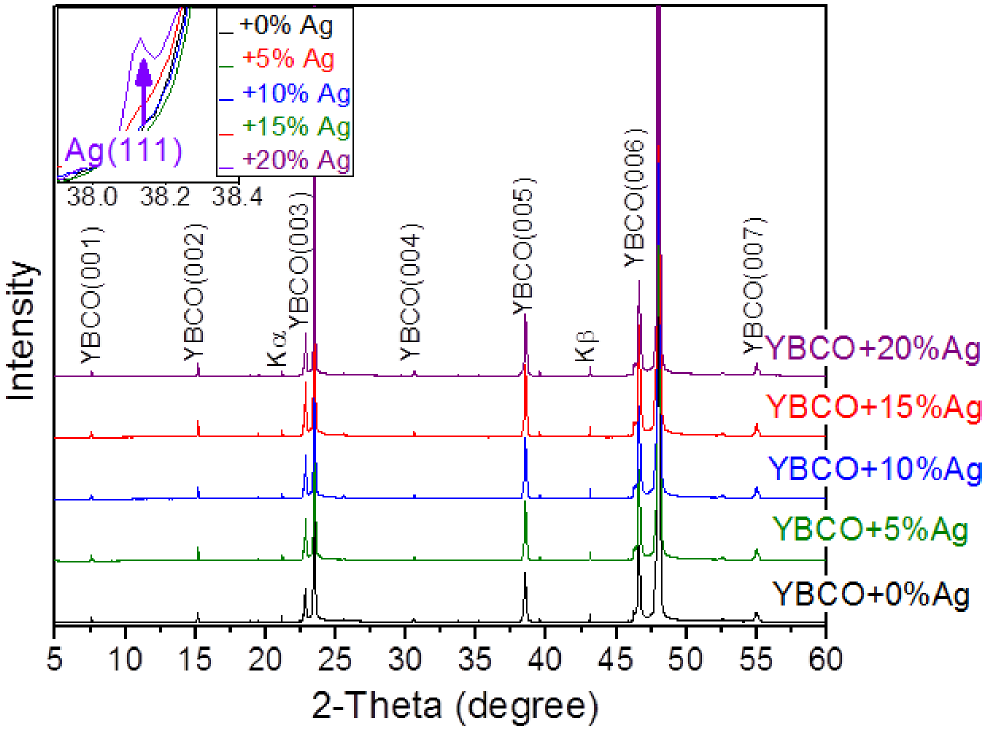

Fig 7.7 XRD patterns of YBCO-Ag films annealed at 790℃ for one hour with different percentages of silver addition.

As shown in **Fig 7.8**, the FWHM value of the YBCO (005) peaks of the films were measured to characterize the film crystallization. The as-grown and fully-sintered samples were quenched out when the temperature just reached 770℃ and after holding for 1 hour at 790℃, respectively.

It clearly appears that the FWHM value of the pure YBCO film decreases gradually, due to the YBCO grain growth with the synthesis going on. Although the FWHM values don't decrease monotonically with the addition of silver, especially for the as-grown samples, where an increase is seen by raising the Ag-doping level from 5wt%, a significant general improvement is evident by comparison between the samples with and without Ag-doping at any level.

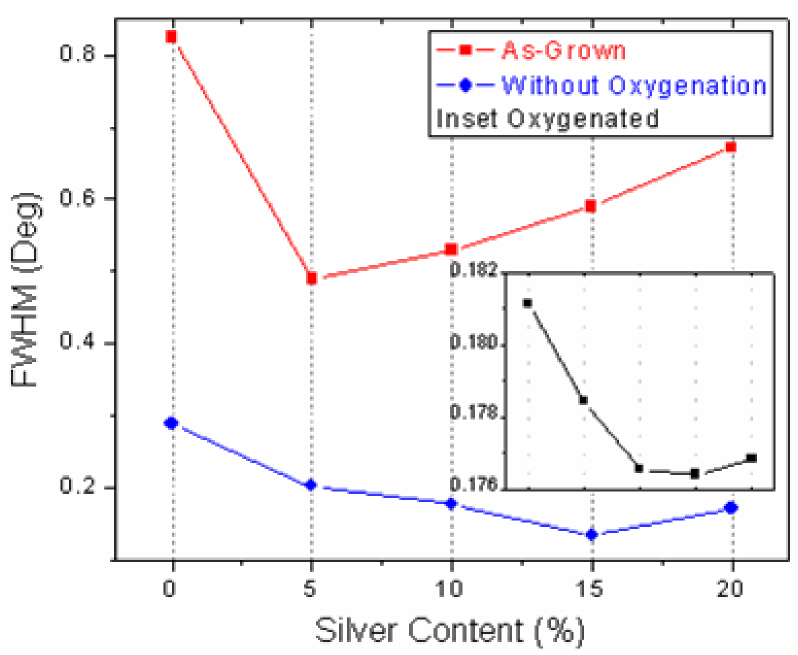

Fig 7.8 .*Silver-doping dependence of the FWHM value of the YBCO (005) peak of the films quenched at different processing steps.*

The room-temperature electrical resistance of the samples displayed in **Fig 7.8** was measured and is as shown in **Fig 7.9** as a function of Ag-doping level. The resistances of the samples quenched at all stages decreases invariably with the addition of silver. This can be due to two reasons. One is the enhanced crystallization as mentioned above, as increased grain size can lead to a decreased number of grain boundaries, which are a main factor for increased resistivity. Another possible reason originates from the reduced intergrain resistance as silver may tend to segregate at grain boundaries and in pores [25]. The mechanism of this conductivity enhancement has been described as film conducting behavior changing from SIS

(Superconductor-Insulator-Superconductor) to SNS (Superconductor-Normal conductor-Superconductor) by silver doping [26].

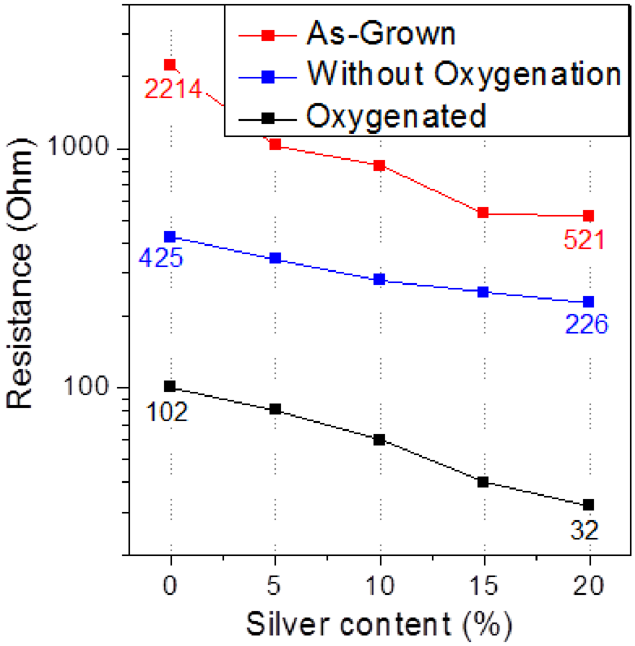

***Fig 7.9** Silver-doping dependence of room temperature resistance of YBCO-Ag films quenched at different processing steps.*

FWHM values extracted from Phi-scans of the (103) reflection and rocking curves of the (005) reflection of the annealed films are shown in **Fig 7.10**. The results reveal that the silver-doping induced melting of YBCO is beneficial to the out-of-plane texture. However, the in-plane texture is not improved. This can be assigned to the Y211 by-product phase. When YBCO grains grow within the a-b plane and encounter a Y211 particle, the migrating facets tend to change direction and the grain alignment is somehow disturbed [27].

It can be seen from **Fig 7.11** that the deposited monolayer of the YBCO+10wt%Ag film is approximately 200nm thick. The indexing result of the SAED pattern reveals a well textured YBCO phase structure, without any interruption induced by silver. However, no silver particles was observed.

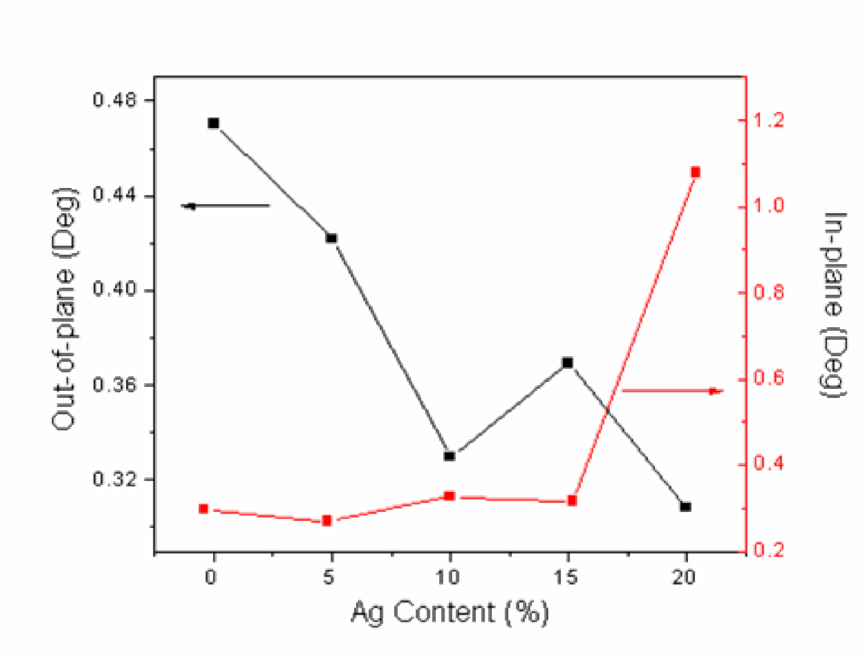

Fig 7.10 *Silver-doping dependence of the in-plane and out-of-plane texture of YBCO-Ag films annealed at 790℃.*

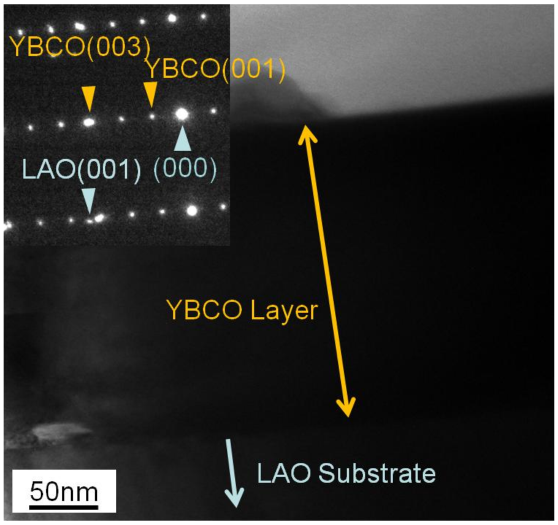

Fig 7.11 *TEM image of the YBCO+10%Ag film annealed at 790℃.*

7.3.3 Superconducting properties

The AC susceptibility of the YBCO films was measured to characterize the superconducting transition. The real components are shown in **Fig 6.12**. The T_c values for the samples with different silver doping levels show no appreciable difference, as all of them show a $T_{c,\ onset}$ of approximately 90K and a ΔT within 1K.

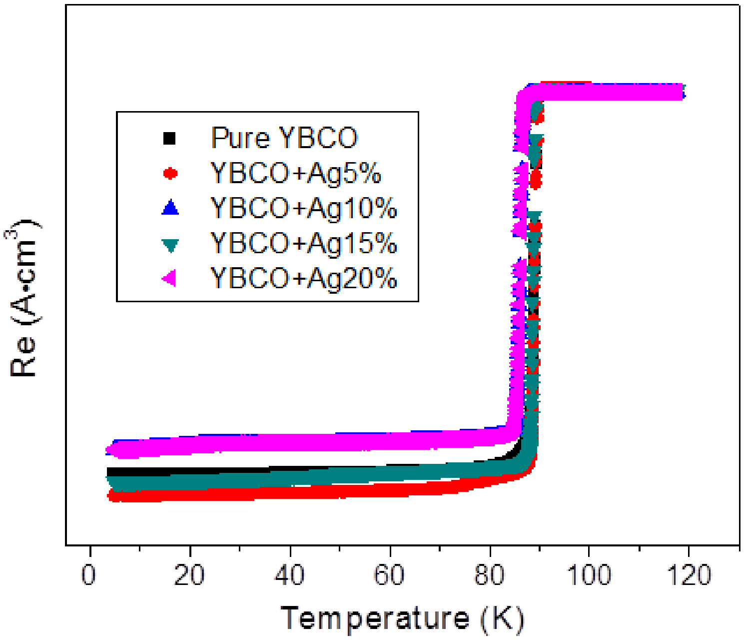

Fig 7.12 *AC susceptibility of the YBCO-Ag samples annealed at 790℃.*

Fig 7.13 shows the J_c of the YBCO films versus the magnetic field applied perpendicularly to the film plane. The J_c values were calculated based on a thickness of 200nm measured by TEM. Y. P. Li et.al [28] found enhanced in-field performance by introducing silver as flux pinning centers through the PLD method. However, by use of the MOD technique we don't observe any significant J_c-improvements in the silver-added samples.

Fig 7.14 shows the J_c values of the samples annealed in N_2/200ppm O_2 versus silver-doping levels and the J_c values versus oxygen partial pressure. It is obvious that the J_c values tend to increase with the addition of silver. We attribute this tendency to both the enhanced grain growth during melting sintering and the reduced intergrain resistance as mentioned above. It is noteworthy that the sample with 10wt% silver addition annealed under 400ppm oxygen partial pressure shows a J_c as high as 4.6MA/cm^2, which is comparable with most of the TFA-MOD derived samples [29, 30].

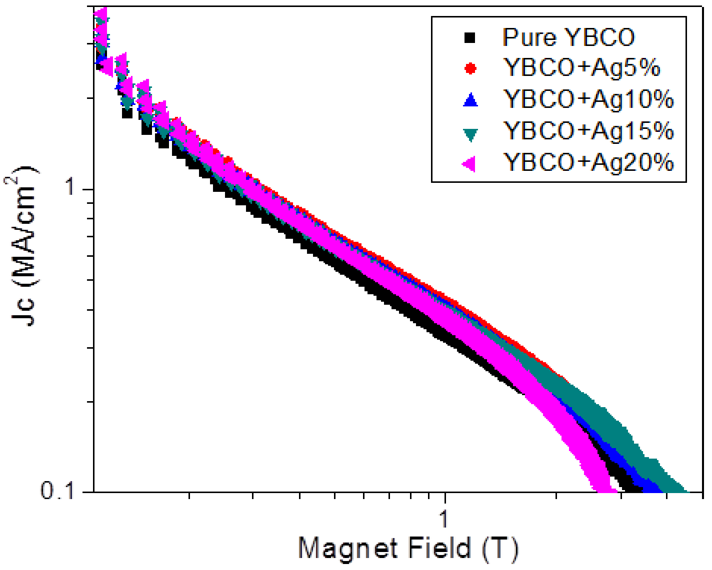

Fig 7.13 *Field dependence of J_c of the YBCO-Ag samples annealed at 790℃.*

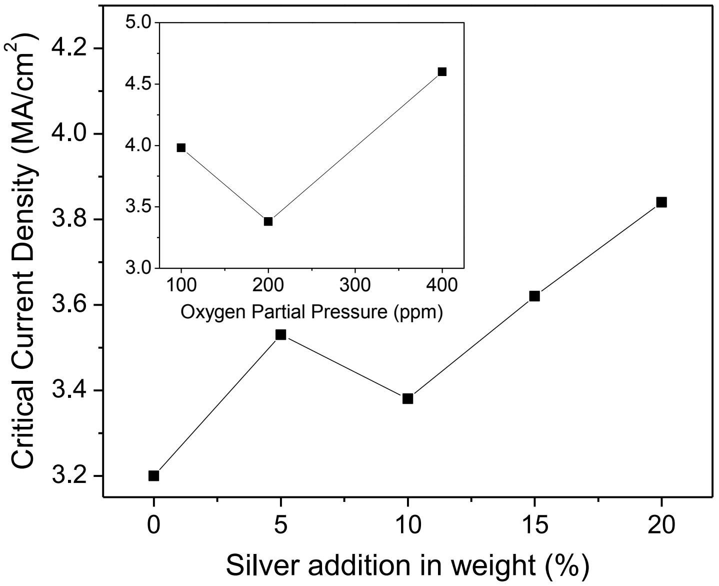

Fig 7.14 *Silver-doping dependence of J_c of the YBCO-Ag thin films annealed at 790℃ under N_2 gas containing 200ppm oxygen partial pressure. Inset: J_c values of YBCO+10wt%Ag thin films annealed at 790℃ under different oxygen partial pressures.*

7.4 Conclusion

In this work, a non-fluorine MOD method was successfully used to deposit YBCO-Ag superconducting thin films on LAO single crystals. Silver addition results in improved surface morphology and enhanced superconducting critical current. A remarkably high J_c (77K, sf) of 4.6MA/cm^2 was obtained on a sample with 10wt% Ag additive annealed under optimized conditions. This makes the performance of non-fluorine method derived YBCO films comparable to that of traditional TFA-MOD processed films. However, the role of Ag in the improvement is quite complicated and not totally clear. According to the results shown in this report, we attribute the improvement to two possible causes. One is the lowered incongruent melting point of the YBCO phase, which is not only beneficial to the c-axis YBCO grain growth but can as well help avoiding the oxidation of the metallic substrate at high annealing temperatures. The other could be that silver enhances the J_c by increasing the transparency at grain boundaries.

Reference

[1] A. Gupta, R. Jagannathan, E. I. Cooper, E. A. Giess, J. I. Landman, *Applied physics Letters*. **52** (1988) 2077-2079.

[2] J. A. Smith, M. J. Cima, N. Sonnenberg, *IEEE TRANSACTIONS ON APPLIED SUPERCONDUCTIVITY*. **9** (1999) 1531-1534.

[3] T. Araki, K. Yamagiwa, I. Hirabayashi, K. Suzuki, S. Tanaka, *SUPERCONDUCTOR SCIENCE AND TECHNOLOGY*. **14** (2001) L21-L24.

[4] J-A. Jee, B. Ma, V. A. Maroni, M. Li, B. L. Fisher, U. Balachandran, *SUPERCONDUCTOR SCIENCE AND TECHNOLOGY*, **14** (2001) 285-291.

[5] T. Arakil, I. Hirabayashi, J. Shibata, Y. Ikuhara, *SUPERCONDUCTOR SCIENCE AND TECHNOLOGY*. **15** (2002) 913-916.

[6] Y. L. Xu, A. Goyal, J. Lian, N. A. Rutter, D. L. Shi, S. Sathyamurthy, M. Paranthaman, L. Wang, P. M. Martin, D. M. Kroeger, *Journal of America Ceramics Sociaty*. **87** (2004) 1669-1676.

[7] G. Risse, B. Schlobach, W. HaÈûler, D. Stephan, T. Fahr, K. Fischer, *Textured YBCO-Film Formation by Sol-Gel Process and Post Annealing*. *Journal of the European Ceramic Society*. **19** (1999) 125-130.

[8] A. J. Bubendorfer, T. Kemmitt, L. J. Campbell, N. J. Long, *IEEE TRANSACTIONS ON APPLIED SUPERCONDUCTIVITY*. **13** (2003) 2739-2742.

[9] F. Parmigiani, G. Chirallo, N. Ripamonpi, *PHYSICAL REVIEW B*. **36** (1987) 7148-7150.

[10] L. Lei, G. Y. Zhao, J. J. Zhao, H. Xu, *IEEE TRANSACTIONS ON APPLIED SUPERCONDUCTIVITY.* **20** (2010) 2286-2293.

[11] M. Sohma, T. Tsuchiya, K. Tsukada, I. Yamaguchi, T. Manabe, T. Kumagai, K. Koyanagi, T. Ebisawa, H. Ohtsu, *Physica C*. **463-465** (2007) 891-894.

[12] D. Kumar, M. Sharon, R. Pinto, P. R. Apte, S. P. Pai, *Applied Physics Letters*. **62** (1993) 3522-3524.

[13] P. Selvam, E. W. Seibt, D. Kumar, R. Pinto, P. R. Apte, *Applied Physics Letters*. **71** (1997) 137-139.

[14] M. Farbod, M. R. Batvandi, *Physica C*. **471** (2011) 112-117.

[15] C. H. Kao, Y. S. Shiue, S. R. Sheen and M. K. Wu, *Physica C*, **205** (1993) 186-190.

[16] U. Wiesner, G. Krabbes, M. Ueltzen, C. Magnerkurth, J. Plewa, H. Altenburg, *Physica C*, **294** (1998) 17-22.

[17] E. M. Gyorgy,R. B. van Dover, K. A. Jackson, L. F. Schneemeyer, J. V. and Waszczak, *Applied Physics Letters*. **55** (1989) 283-285.

[18] X. Obradors, F. Martinez-Julian, K. Zalamova, V. R. Vlad, A. Pomar, A. Palau, A. Llordes, H. Chen, M. Coll, S. Ricart, N. Mestres, X. Granados, T. Puig, M. Rikel, *Physica C*. **482** (2012) 58-67.

[19] P. Vermeir, I. Cardinael, J. Schaubroeck, K. Verbeken, M. Backer, P. Lommens, W. Knaepen, J. D’haen, K. D. Buysser, I. V. Driessche, *Inorganic Chemistry*. **49** (2010) 4471-4477.

[20] J. S. Kim and D. R. Gaskell, *Journal of American Ceramic Sociaty*. **77** (1994) 753-758.

[21] W. T. Wang, M. H. Pu, W. Wang, H. Zhang, C. H. Cheng, Y. Zhao, *Journal of Superconductivity and Novel Magnetism*. 23 (2010) 989-993.

[22] T. H. Tiefel, S. Jin, R. C. Sherwood, M. E. Davis, G. W. Kammlott, P. K. Gallagher, D. W. Johnson, *Materials Letters*, **7** (1989) 363-366.

[23] P. Y. Chu, R. C. Buchanan, *Journal of Materials Research*. **8** (1993) 2134-2142.

[24] P. Y. Chu, R. C. Buchanan, *Journal of Materials Research*. **9** (1994) 844-851.

[25] R. Kalyanaraman, S. Oktyabrsky J. Narayan, The role of Ag in the pulsed laser growth of YBCO thin films. Applied Physics Letters. 85 (1999) 6636-6641.

[26] T. S. Orlova, B. I. Smirnov, J. Y. Laval, Yu. P. Stepanov, *Superconducting Science and Technology*, **12** (1999) 356-359.

[27] D. L. Shi, *High-temperature superconducting materials science and engineering*, 1995, pp360

[28] Y. P. Li, J. R. Liu, X. T. Cui, Y. Cao, Z. J. Qu, Q. Y. Chen, C. W. Chu, W. K. Chu, *Physica C*. **282-287** (1997) 653-654.

[29] P. C. McIntyre, M.J. Cima, J.A. Smith, R.B. Hallock, M.P. Siegal, and J.M. Phillips, *Journal of Applied Physics*, **71** (1992) 1868-1877.

[30] J. A. Smith, M. J. Cima, and N. Sonnenberg, *IEEE Transactions on Applied Superconductivity*, **9** (1999) 1531-1534.

Chapter 8

Effect of $BaZrO_3$/Ag hybrid doping to the microstructure and performance of fluorine-free MOD method derived $YBa_2Cu_3O_{7-x}$ superconducting thin films

(Status suspended due to the confidentiality of the patent)

It is known that $BaZrO_3$ and Ag can improve the magnetic and transport performance of YBCO thin film through totally disparate ways. $BaZrO_3$ plays the role of flux pinning centers and Ag improves the transparency of the YBCO grain boundaries. However, similar research is rare on the fluorine-free derived YBCO films. In this research, $BaZrO_3$-doped, Ag-doped and $BaZrO_3$/Ag hybrid-doped YBCO films were synthesized through a fluorine-free MOD method. $BaZrO_3$ was found to deteriorate the microstructure and performance of YBCO, while Ag-doping was found to enhance the crystallization of YBCO and resulted in a high J_c of 3.87MA/cm^2 in self-field at 77K. However, the microstructure and performance of the $BaZrO_3$/Ag hybrid-doped YBCO film showed that the positive impact of Ag-doping was totally overwhelmed by that of $BaZrO_3$.

8.1 Introduction

For the advantages such as low cost, high productivity, and ease of scaling-up, the development of Chemical Solution Deposition (CSD) routes for high performance $YBa_2Cu_3O_{7-x}$ (YBCO) thin films remains one of the hot spots in the research on the Second Generation High Temperature Superconductor wires (2G HTS) since the discovery of REBCO (RE=rare earth) in 1986 [1].

Among all the CSD routes that can be potentially used for fabricating YBCO thin films, metal-organic deposition using trifluoroacetates as precursors (TFA-MOD) nowadays is undoubtedly the most extensively studied one [2-4]. However, the hazardous HF gas evolving as a byproduct makes the decomposition process of the TFA-MOD technique very sluggish and not environmentally friendly [5]. Therefore, Fluorine-free MOD (FF-MOD) techniques have been attracting increasing attention in recent years [6-8]. Though varied efforts have been done in the aim of improving the microstructure and J_c values of the FF-MOD derived YBCO films, to meet the requirements for the application in high-current-carrying wires and high magnetic field engineering [9-10], it is essential to further improve the transport and magnetic performances of the products [11]. In the aim of enhancing the in-field J_c value, Ba-related nonconductor materials, particularly $BaZrO_3$, have been introduced as Artificial Pinning Centers (APC) to provide strong pinning force, which can greatly prevent the magnetic flux lines from creeping in the applied field [12]. However, the structural integrity of YBCO was found to be severely deteriorated by the doping process at the expense of the enhanced in-field performance [13]. On the other hand, Ag normal conductor nano-dots have also been introduced to enhance the electrical performance of YBCO [14-16]. Different from the mechanism of $BaZrO_3$ dopping, previous investigations showed that Ag additions can greatly improve the integrity and performance of the films by accelerating the grain growth of YBCO and improving the conductivity at the YBCO grain boundaries [16]. Regarding the disparate but complementary characteristics of the Ag doping and the $BaZrO_3$ doping, it will be very meaningful to investigate the effect of $BaZrO_3$/Ag hybrid doping onto the microstructure and performance of FF-MOD derived YBCO films.

8.2 Experimental details

The fluorine-free precursor solution for producing pure YBCO films was prepared by initially mixing stoichiometric amounts (1:2:3) of $Y(CH_3COO)_3 \cdot 4H_2O$ (Purity 99.9%, Alfa Aesar), $Ba(CH_3COO)_2$ (Purity 99%, Alfa Aesar), and $Cu(CH_3COO)_2 \cdot H_2O$ (Purity 98%, Alfa Aesar). The solid mixture was then dissolved in a mixture of propionic acid (Purity 99%, Alfa Aesar) and ammonia (Purity 99%, Alfa Aesar) at the volume ratio of 3:1. After one hour stiring at 80℃ on a heating plate, the solution became clear blue without any precipitation. Afterwards, all the extra solvent was removed by an evaporator. During this process, deionized water was added to help the removal of acid until a blue glassy gel was obtained. Finally, the gel was dissolved in methanol, to yield a homogeneous solution with a total metal concentration (Y, Ba and Cu, without Ag) of 1.5mol/L. The solutions for producing doped YBCO films were prepared through a process similar to that used for the pure YBCO solution. For the solution used for preparing Ag-doped and $BaZrO_3$/Ag-doped films, $AgNO_3$ (Purity 99.9%, Alfa Aesar) was initially added into the mixture of Y/Ba/Cu acetates at the molar ratio of Ag: Y= 5:100. For the solution used for preparing $BaZrO_3$ doped and $BaZrO_3$/Ag-doped films, quantitative additional Barium acetates was used to compensate for the formation of $BaZrO_3$. Zirconium (IV) Acetylacetonate (Alfa Aesar) was separately dissolved in propionic acid at 60℃ and then evaporated into a yellow gel. Afterwards, the gel was moderately diluted by methanol and mixed with pure YBCO precursor solution at the molar ratio of Zr: Y = 6: 100. By adjusting the volume of methanol, the metal concentration (ignoring the metal content of Ag and Zr) for each of the solutions was controlled at 1.5mol/*l*.

The precursor solutions were deposited onto LAO single crystals by spin coating at 6000rpm and pyrolyzed at 450℃ in humid oxygen atmosphere with a heating rate of 5℃/min. After pyrolysis, the atmosphere was switched into Ar/100ppmO_2 and the films were heated up to 790℃ with a heating rate of 20℃/min. After 1h holding at 790℃, the samples were cooled down to 450℃ at a ramping speed of 5℃/min, and then holding for 15h in pure oxygen to convert the tetragonal phase to orthorhombic superconducting phase.

A Bruker D8 X-ray diffractometer with Cu Kα radiation was used to characterize the microstructure of the annealed thin films. The surface morphology of the samples was investigated in a Supra 35 (SEM) electron microscope in secondary electron mode. AC suscepitibility measurements combined with hysteresis loops were carried out in a CRYOGENIC cryogen free measuring system (CFMS). The critical current density (J_c) of the samples was calculated by using the extended Bean critical state model [17].

8.3 Results and discussion

Fig 8.1 shows the XRD patterns of the pure and doped YBCO films. Sharp (00*l*) diffraction peaks of YBCO were clearly observed, without any random orientation peaks detected, implying a well textured microstructure for all films. However, the intensity of the YBCO (00*l*) peaks in the $BaZrO_3$-doped film was much lower compared to the pure YBCO film, implying a deteriorated crystallization of YBCO. Observation by SEM (**Fig 8.2 (a)** and **(b)**) also showed that flaky and needle-like particles were more randomly oriented on the surface without conspicuous interconnections. According to the absence of the peaks corresponding to randomly oriented YBCO in the XRD pattern, we hypothesis that epitaxial grain growth occurred near the substrate interface and was maintained to a certain extent in thickness, but degraded significantly when approaching to the surface, thus the randomly oriented grains observed in the SEM picture didn't contribute much to the XRD result.

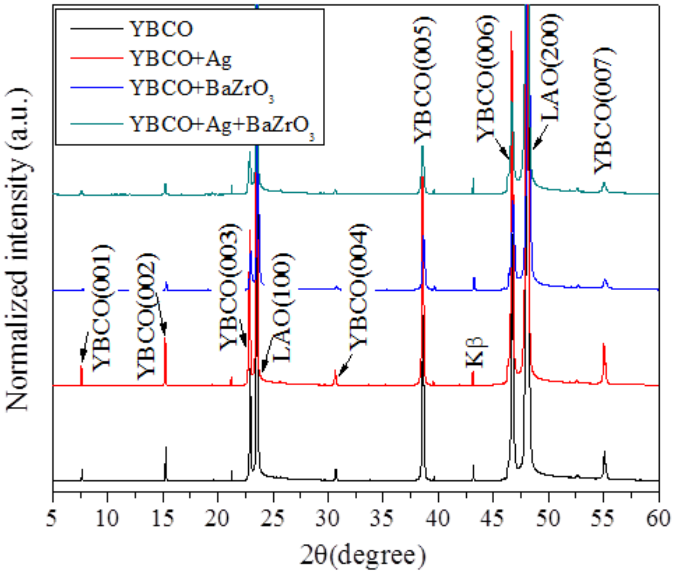

Fig 8.1 *XRD patterns of the pure YBCO film, Ag-doped YBCO film,* $BaZrO_3$*-doped YBCO film, and Ag-*$BaZrO_3$*-doped YBCO film sintered at 790 ℃ for 1h.*

M. Veith et.al [18] have confirmed that by using acetates as precursors, the formation of $BaZrO_3$ starts from 500-600℃, which is prior to the initial nucleation of YBCO at 620℃ in the FF-MOD method [19]. However, during the formation of $BaZrO_3$, a certain amount of $BaCO_3$ was found as a stable contaminant existing up to 1000℃. More serious is the formation of by-product Ba-rich phases Ba_2ZrO_4 [18], which in our research could have resulted a lack of Barium in the growing YBCO film. The liquid phase containing barium and copper plays a significant role in forming epitaxial YBCO films by using FF-MOD, as shown in equation (A) and (B). Therefore the lack of barium induced by the formation of Ba_2ZrO_4 undoubtedly reduces the availability of liquid interferes with the growth mechanism of the growing epitaxial films.

To further investigate the influence of the $BaZrO_3$-doping on the crystallization of YBCO, XRD and SEM were measured on the pure YBCO and $BaZrO_3$-doped YBCO films that were annealed at different temperatures for comparison. **Fig 8.3** shows the YBCO (005) peak' intensities of pure YBCO and YBCO-5%$BaZrO_3$ films on the annealing temperature. It is obvious that the crystallization of YBCO along the preferred orientation was most enhanced with an annealing temperature of about 790℃ in both the pure and $BaZrO_3$-doped YBCO thin films. However, this deteriorated with further increases in the temperature due to the decomposition of YBCO at high temperatures. In the temperature regime below the melting point of YBCO, with increasing temperature, the YBCO crystallization along the c-axis orientation and the interconnection between the YBCO grains are improved by the enhanced formation of $BaCuO_2$ liquid phases. The much inferior YBCO crystallization in the $BaZrO_3$-doped YBCO films compared to that at the pure YBCO films implies the possibility of a weakened liquid phase formation resulting from the introduction of Zirconium, which could snatch the barium contents to form $BaZrO_3$ or Ba_2ZrO_4.

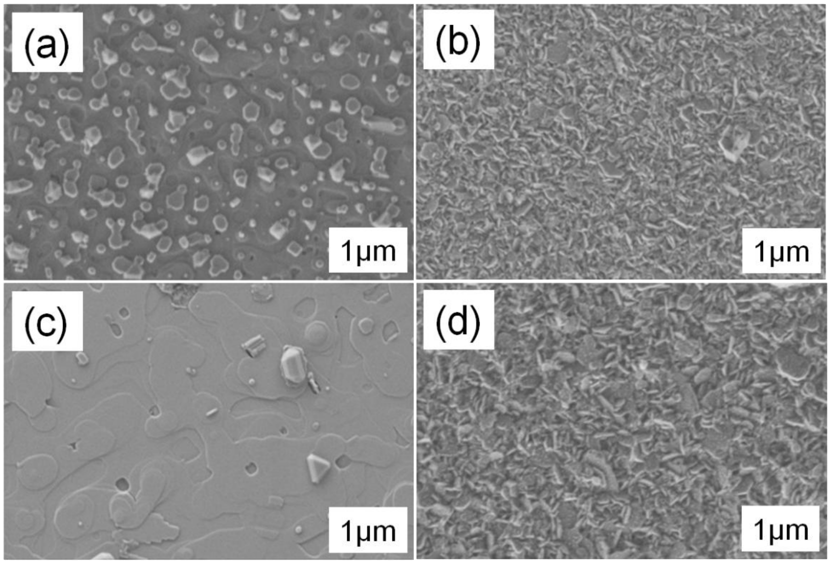

Fig 8.2 *Surface morphology of (a) pure YBCO film, (b) $BaZrO_3$-doped YBCO film, (c) Ag-doped YBCO film, (d) and Ag-$BaZrO_3$-doped YBCO film sintered at 790 ℃ for 1h.*

A similar phenomenon was reflected from the surface morphology of the films, as shown in **Fig 8.4**. Smoother and better interconnected surfaces were seen on the pure YBCO films with increasing annealing temperature, whereas both the $BaZrO_3$-doped thin films showed porous polycrystalline structures without a conspicuous temperature dependence, implying the lack of a liquid phase during the YBCO formation. XRD measured on the $BaZrO_3$ thin films annealed at different temperatures also confirmed our hypothesis. As shown in **Fig 8.5**, the intensity of the $BaZrO_3$ (200) peak increased from 600℃ up to 750℃, which coincides with the YBCO formation, and suggesting a conflict between the formation of $BaZrO_3$and YBCO.

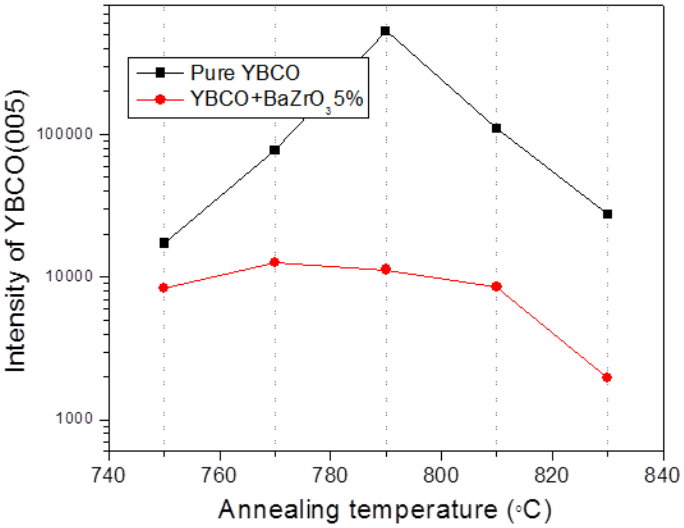

Fig 8.3 *Annealing temperature dependence of YBCO (005) peaks' intensities of pure YBCO and YBCO-*$BaZrO_3$*5% films.*

In contrast, the Ag-doped film shows an exceptionally high intensity of the YBCO (00*l*) peaks, indicating an enhancement of the crystallization of the grains along the c-axis. Also as shown in **Fig 8.2(a) and (c)**, compared to the pure YBCO thin film, a more uniform and dense melting-texture can be seen on the surface of the Ag-doped YBCO film. This phenomenon coincides with the results from investigations on YBCO/Ag pellets produced through a solid reaction, during which the silver additive dramatically decreased the peritectic point of YBCO and consequently promoted the formation of a partial melting phase [16]. The importance of partial melting of YBCO in FF-MOD reaction process has been demonstrated by P. Y Chu et.al [19], as it can greatly eliminate porosity and leads to a favored rearrangement of the already nucleated YBCO grains. The reaction is shown in equation (C), is which was promoted by silver doping.

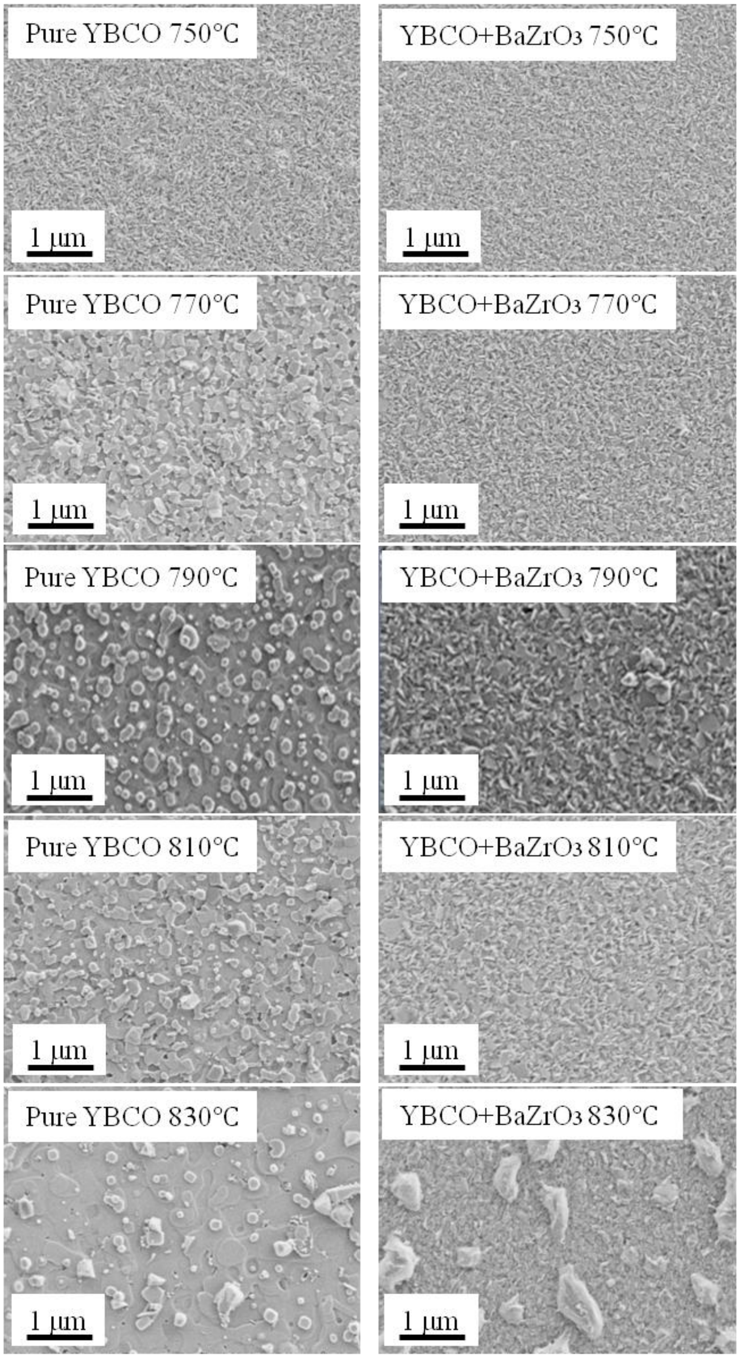

Fig 8.4 *Annealing temperature dependence of surface morphology of pure YBCO and YBCO-* $BaZrO_3$*5% films.*

$$BaCO_3 + CuO \rightarrow L1 \qquad (A)$$

$$Y_2O_3 + L1 \rightarrow YBa_2Cu_3O_{7-x} \qquad (B)$$

$$CuO + YBa_2Cu_3O_{6+x} \rightarrow Y_2BaCuO_5 + CuO + L2 \qquad (C)$$

Though considerable improvement of the microstructure has been seen on the Ag-doped YBCO film, the positive effect of silver doping was found be totally overwhelmed by the negative influence of $BaZrO_3$ in the $BaZrO_3$/Ag hybrid doped YBCO film, the microstructure of which is quite similar to that of the $BaZrO_3$-doped YBCO film, as shown in both the XRD pattern and SEM image (**Fig 8.2(d)**). This means that the reaction responsible for YBCO melting has been interfered by the presence of carbonate contaminate and the barium-rich Ba_2ZrO_4 phase. Therefore, the impact of Ag-doping was cancelled.

AC susceptibility was measured to characterize the superconducting behavior of the film samples. The real component of the AC susceptibility of all samples between 35K and 105K are shown in **Fig 8.3**. The pure YBCO and the Ag-doped YBCO films display sharp superconducting transitions, which start from 91K, with a temperature width of 1K. In contrast, the $BaZrO_3$-doped and $BaZrO_3$/Ag-doped YBCO films show broad transitions, with $\Delta T_c \geq 30K$, indicating a deteriorated microstructure induced by $BaZrO_3$-doping.

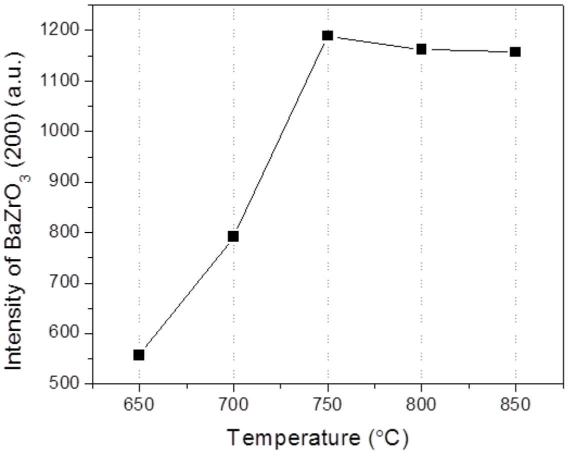

Fig 8.5 *Annealing temperature dependence of intensity of* $BaZrO_3$ *(200) of* $BaZrO_3$ *films.*

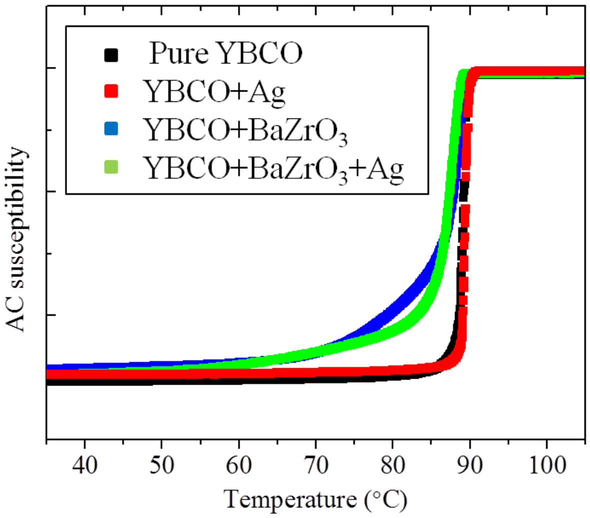

Fig 8.6 *Dependence of AC susceptibility on temperature for the pure YBCO film, Ag-doped YBCO film, BaZrO*$_3$*-doped YBCO film, and Ag-BaZrO*$_3$*-doped YBCO film sintered at 790 ℃ for 1h.*

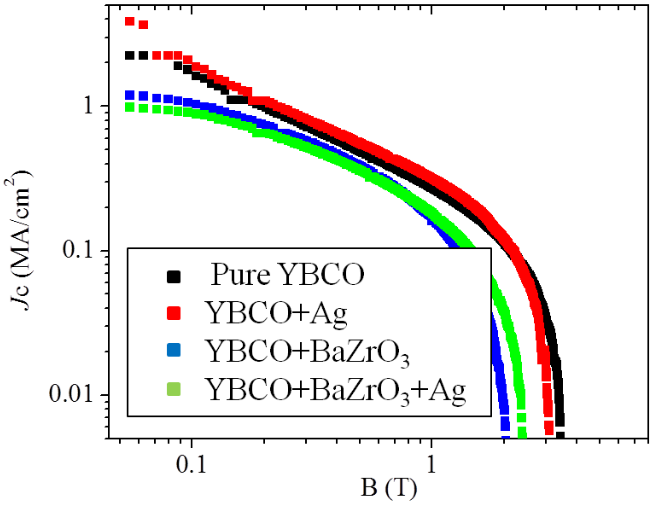

Fig 8.7 *Critical current density versus magnetic field applied parallel to the c-axis at 77K for a pure YBCO film, a Ag-doped YBCO film, a BaZrO*$_3$*-doped YBCO film, and a Ag-BaZrO*$_3$*-doped YBCO film sintered at 790 ℃ for 1h.*

The effect of an applied magnetic field on J_c values at 77K for the pure YBCO film and the doped YBCO films is depicted in **Fig 8.4**. In self-field, the J_c value of the pure YBCO film was 2.1MA/cm^2, in comparison a high J_c value of 3.87MA/cm^2 was recorded on the Ag-doped YBCO film, confirming a significant enhancement of J_c by Ag-doping. This can be due to two reasons. One is the enhanced crystallization as mentioned above, as increased grain size can lead to a decreased number of grain boundaries, while another possible reason originates from the reduced intergrain resistance as the silver segregation at grain boundaries and in pores may change the conducting behavior from SIS (superconductor-insulator-superconductor) into SNS (superconductor-nomal conductor-superconductor) [20]. However, the J_c value was found not be improved by Ag-doping in high field, as the J_c value of the Ag-doped film dropped even faster compared to that of the pure YBCO film when the applied field was higher than 2T. In contrast, the $BaZrO_3$-doped and the $BaZrO_3$/Ag-doped YBCO films showed deteriorated performance both in self-field and high applied field. The J_c value of both samples reached 1MA/cm^2, however, it sharply decreased when the field higher than 1T.

8.4 Conclusion

$BaZrO_3$ and Ag were introduced in an attempt to improve the J_c performance of YBCO thin films prepared through FF-MOD method. Probably due to the formation of $BaCO_3$ contaminant or Ba-rich phases, the crystallization of YBCO was severely hindered and consequently the J_c value of the films both in self-fields and high fields was deteriorated. Ag-doping appeares to be a promising route to improve the J_c value of YBCO films in FF-MOD methods, as it dramatically facilitates the partial melting of YBCO, which can improve the crystallization of the film. As a result, the J_c of the Ag-doped YBCO film reached at 3.87MA/cm^2 at 77K in self-field. By using the same FF-MOD method, the effect of $BaZrO_3$/Ag hybrid doping in YBCO films was investigated. However, the positive influence of Ag-doping was totally cancelled by that of $BaZrO_3$.

Reference

[1] M. Kakihana, *Journal of Sol-Gel Science and Technology*, **6** (1996) 7-55.

[2] K. Zalamova, A. Pomar, A. Palau, T. Puig, X. Obradors, *Superconductor Science and Technology*, **23** (2010) 014012.

[3] P. C. McIntyre, M.J. Cima, J.A. Smith, R.B. Hallock, M.P. Siegal, and J.M. Phillips, *Journal of Applied Physics*, **71** (1992) 1868-1877.

[4] J. A. Smith, M. J. Cima, and N. Sonnenberg, *IEEE Transactions on Applied Superconductivity*, **9** (1999) 1531-1534.

[5] B. A. Glowacki, M. Mosiadz, *Journal of Sol-Gel Science and Technology,* **51** (2009) 335-347.

[6] Y. L. Xu, A. Goyal, J. Lian, N. A. Rutter, D. L. Shi, S. Sathyamurthy, M. Paranthaman, L. Wang, P. M. Martin, D. M. Kroeger, *Journal of America Ceramics Society*. **87** (2004) 1669-1676.

[7] G. Risse, B. Schlobach, W. HaÈ ûler, D. Stephan, T. Fahr, K. Fischer, *Journal of the European Ceramic Society*. **19** (1999) 125-130.

[8] A. J. Bubendorfer, T. Kemmitt, L. J. Campbell, N. J. Long, *IEEE TRANSACTIONS ON APPLIED SUPERCONDUCTIVITY*. **13** (2003) 2739-2742.

[9] L. Lei, G. Y. Zhao, J. J. Zhao, H. Xu, *IEEE TRANSACTIONS ON APPLIED SUPERCONDUCTIVITY*. **20** (2010) 2286-2293.

[10] P. Vermeir, J. Feys, J. Schaubroeck, K. Verbeken, M. Backer, *Materials Chemistry and Physics*, **133** (2012) 998-1002.

[11] S. R. Foltyn, L. Civale, J. L. Macmanus-Driscoll, Q. X. Jia, B. Maiorov, H. Wang, M. Maley, *Nature Materials*, **6** (2007) 631-642.

[12] K. Matsumoto, P. Mele, *Superconductor Science and Technology*, **23** (2010) 014001.

[13] I. Birlik, M. Erbe, T. Freudenberg, E. Celik, L. Schultz, B. Holzapfel, *Journal of Physics: Conference Series*, **234** (2010) 012004.

[14] D. Kumar, M. Sharon, R. Pinto, P. R. Apte, S. P. Pai, *Applied Physics Letters*. **62** (1993) 3522-3524.

[15] P. Selvam, E. W. Seibt, D. Kumar, R. Pinto, P. R. Apte, *Applied Physics Letters*. **71** (1997) 137-139.

[16] L. C. Pathak, S. K. Mishra, S. Srikanth, *Journal of Materials Research*, **17** (2002) 895-900.

[17] E. M. Gyorgy, R. B. van Dover, K. A. Jackson, *Applied Physics Letters*, **55** (1989) 283-285.

[18] M. Veith, S. Mathur, N. Lecerf, V. Huch, T. Decker, *Journal of Sol-Gel Science and Technology*, **15** (2000) 145-158.

[19] P.-Y. Chu, R. Buchanan, *Journal of Materials Research*, **8** (1993) 2134-2142.

[20] T. S. Orlova, B. I. Smirnov, J. Y. Laval and Yu. P. Stepanov, *Superconducting Science and Technology*, **12** (1999) 356-359.

Chapter 9

Summary

First of all, a preliminary review and subsequent trials of the existing CSD routes were performed with the aim of obtaining a systematic evaluation of them before carrying out particular research on a certain CSD route. Different from the previous classification of the CSD routes which depends on the diverse types of organic agents that are present in the precursor solution, within this thesis the main CSD routes were classified into four categories depending on the barium products (BaF_2, $Ba(OH)_2$, $BaNO_3$, and $BaCO_3$) present after the decomposition of the organic precursors. This is motivated by the significant role that the barium intermediate phases play during the formation of the YBCO superconducting phase. The trails on the barium hydroxide and the barium nitrate processes showed dramatic facilitation of YBCO formation at low temperatures, which was due to the low melting points of $Ba(OH)_2$ and $BaNO_3$. However, the heterogeneous YBCO nucleation along both the c-axis and the a-axis at low temperatures was not beneficial to the epitaxial growth of YBCO thin films. Moreover, the low metal concentration of the precursor solution and the decomposition of YBCO induced by the water partial pressure also reduced the applicability of the barium nitrate and the barium hydroxide processes, respectively. Depending on the balanced properties compared to the other processes, the barium carbonate processes appear to be the most promising non-fluorine CSD routes for producing high-quality YBCO superconducting films.

Secondly, a non-fluorine aqueous sol-gel technique was used to produce YBCO superconducting thin films. Efforts were made in the aim of improving the aqueous-based DEA-chelating process for fabricating high-quality YBCO superconducting thin films. Acetic acid was added in order to modify the complexation process taking place between the metal cations and the organic chelating agents. The electrical resistance and the pH value were used as indicators of the quality of the precursors. When pH=6.5, the precursor solution had the lowest resistance, implying a good ionization of the starting metal elements. By using the optimal precursor, the film was found to have very small size particles after pyrolysis. In consequence, the annealed YBCO films are characterized by a sharp superconducting transition, and their J_c (77k) reaches 0.25MA/cm^2. Considering the low J_c value obtained on the DEA-derived film, the influence of DEA and TEA added as chelating agents was investigated. Though yielding a higher mass loss during the decomposition process, the TEA was demonstrated to be beneficial to the microstructure and superconducting performance of the thin films. As a result, the J_c of the YBCO films produced from TEA chelated precursor reached 1.7MA/cm^2 at 77K, a value approaching that of TFA-MOD derived films.

We have also developed a fluorine-free MOD method using acrylic acid as the solvent for the synthesis of GdBCO superconducting thin films. Commonly used propionic acid was also used so as to make a comparison to acrylic acid. Acrylic acid was found to be polymerized during drying and resulted in a high-thermal-stability of the precursor solution. Due to the elevated decomposition temperature of the organic compounds in the acrylic acid based precursor, the formation of intermediate phases such as CuO was delayed and therefore the grain growth and phase segregation were suppressed. The superior quality of pyrolyzed films induced by the use of polymerizable acrylic acid is reflected in the J_c of the GdBCO films, which achieved 1.2MA/cm^2.

Silver-doping was then applied to enhance the J_c values of YBCO films derived from a non-fluorine CSD process. By reacting with propionic acid and ammonia, $AgNO_3$ was initially mixed with YBCO carboxylate precursors dissolved in methanol. High-temperature in-situ XRD measurements of the YBCO-Ag powders revealed that silver addition lowers the incongruent melting temperature of YBCO, which results in a smooth surface morphology of the YBCO films at a temperature as low as 760℃. Grain growth and intergranular conductivity were also found to be improved by silver doping. After annealing under optimized conditions, a high J_c of 4.6MA/cm^2 was obtained in a YBCO-Ag thin film with 10 wt% Ag. Based on the positive effect of Ag-doping on YBCO grain growth and the interconnection at the YBCO grain boundaries, the effect of $BaZrO_3$/Ag hybrid-dopping on the YBCO films were investigated. However, $BaZrO_3$

was found severely deteriorated the microstructure and performance of YBCO, and the microstructure and performance of $BaZrO_3$/Ag hybrid-doped YBCO film also showed that the positive impact of Ag-doping was totally overwhelmed by that of $BaZrO_3$.

Publications

1 **X. Tang**, J-C. Grivel, A Novel SAFF-MOD Technique to Produce High-*J*c YBCO Superconducting Films, *European Patent*, 2013.

2 **X. Tang**, D. He, Y. Zhao, J.-C. Grivel, Characterization of Microstructure and Performance of $YBa_2Cu_3O_{7–x}$ Films Synthesized Through Sol–Gel Aqueous Precursors with DEA/TEA Addition, *Journal of Superconductivity and Novel Magnetism*, 26 (2013) 1883–1886.

3 **X. Tang**, Y. Zhao, W. Wu, N. H. Andersen and J-C Grivel, High-*J*c $YBa_2Cu_3O_{7-x}$-Ag superconducting thin films synthesized through a fluorine-free MOD method, *Status suspended due to the confidentiality of the patent.*

4 **X. Tang**, Y. Zhao, J-C. Grivel, Influence of initial pH on the microstructure of $YBa_2Cu_3O_{7-x}$ superconducting thin films derived from DEA-aqueous sol-gel method, In press *Ceramics International*.

5 **X. Tang**, D. He, Y. Zhao, J-C. Grivel, Manufacture of $GdBa_2Cu_3O_{7-x}$ superconducting thin films using high thermal stability precursors playing the role of intermediate phase grain-growth inhibitors, Submitted to *IEEE TRANSACTIONS ON APPLIED SUPERCONDUCTIVITY.*

6 **X. Tang**, M. S. Bock, Y. Zhao, J.-C. Claude, Effect of $BaZrO_3$/Ag hybrid doping to the microstructure and performance of fluorine-free MOD method derived $YBa_2Cu_3O_{7-x}$ superconducting thin films, *Status suspended due to the confidentiality of the patent*.

7 Y. Zhao, K. Konstantopoulou, A. C. Wulff, **X. Tang**, H. Tian, H. L. Suo, J. Y. Pastor, and J.-C. Grivel, Development of One Meter Long Double-Sided CeO_2 Buffered Ni-5at.%W Templates by Reel-to-Reel Chemical Solution Deposition Route, *IEEE TRANSACTIONS ON APPLIED SUPERCONDUCTIVITY*, 23 (2013).

8 W. Wu, F. Feng, K. Shi, W. Zhai, T. M. Qu, R. X. Huang, **X. Tang**, X. H. Wang, Q. Y. Hu, J-C. Grivel and Z. H. Han, A rapid process of $YBa_2Cu_3O_{7-\delta}$ thin film fabrication

using trifluoroacetate metal–organic deposition with polyethylene glycol additive, *Superconductor Science and Technology*, 26 (2013) 055013.

9 J-C. Grivel, A. Alexiou, K. Rubešová, **X. Tang**, N. H. Andersen, M. von Zimmermann and A. Watenphul, Preparation and characterization of $Mg_{1-x}B_2$ bulk samples and Cu/Nb sheathed wires with low grade amorphous boron powder, Accepted by *Journal of Superconductivity and Novel Magnetism*.

10 **X. Tang**, H. L. Suo, Rapid synthesis of YBCO thick superconducting films by low fluorine TFA-MOD method, *Journal of Inorganic Materials*, 25 (2010) 971-974.